Institutt for fysikk og teknologi

High p_T Physics in Heavy Ion Collisions at $\sqrt{s_{NN}} = 200$ GeV

by

Zhongbao Yin

July 2004

Universitetet i Bergen

Bergen, Norway

Institutt for fysikk og teknologi

High p_T Physics in Heavy Ion Collisions at $\sqrt{s_{NN}} = 200$ GeV

by

Zhongbao Yin

a thesis submitted to Institutt for fysikk og teknologi,
Universitetet i Bergen,
in partial fulfilment of the requirements for
the degree of Doctor Scientiarum

July 2004
Universitetet i Bergen
Bergen, Norway

Preface

Quantum Chromodynamics (QCD), the underlying theory of the strong interaction, predicts a new state of matter called Quark-Gluon Plasma (QGP) where quarks and gluons are freed from confinement. Ultra-relativistic heavy ion collisions at collider energies provide a unique opportunity to explore the properties of such a highly excited dense nuclear matter. A variety of hard probes, e.g. high transverse momentum (p_T) partons which are produced in the early phase of the collisions, are expected to provide a possibility for a detailed quantitative study of the transient partonic matter.

This work concerns the intermediate (high) p_T particle production in ultra-relativistic heavy ion collisions at collider energies. At collider energies the hard pQCD rate of rare high p_T parton scattering becomes sufficiently large that jets can be used to probe the dense strongly interacting partonic medium formed in ultra-relativistic heavy ion collisions. For example, due to induced gluon radiation, hard partons will suffer large energy loss when they travel through the hot medium, resulting in a suppression of high p_T hadron yields. In this thesis, the related high p_T physics will be reviewed in Chapter 2 following an introduction to relativistic heavy ion collisions in Chapter 1. BRAHMS, one of the four experiments at the Relativistic Heavy Ion Collider (RHIC) at Brookhaven National Laboratory (BNL), can measure and identify charged hadrons over a broad range of rapidity and transverse momentum. After a description of the BRAHMS experimental setup and data analysis techniques in Chapter 3, the high p_T spectra of charged pions and (anti-)protons will be presented in Chapter 4 at both mid-rapidity and forward rapidity ($\eta = 2.2$), where they can be well identified up to $p_T = 3$ GeV/c with reasonable statistics. Compared to high p_T yields in $p + p$ and $d + Au$ collisions at the same energy ($\sqrt{s_{NN}} =$ 200 GeV), the nuclear medium effects on the high p_T particle production in heavy ion collisions are studied and compared to other experiments and model calculations. Finally, an outlook on high p_T physics at ALICE/PHOS is given in Chapter 5 and conclusions are summarized in Chapter 6.

Acknowledgments

First I would like to express my sincerest gratitude to my advisor, Prof. Dieter Röhrich. Since the beginning of my study in Bergen four years ago, Prof. Röhrich has always been patient and providing crucial and invaluable advices. His easy-going personality has made it enjoyable to work in his group.

I would like to thank my colleagues and collaborators in the ALICE/PHOS project. I am deeply indebted to Prof. Bernhard Skaali, the project leader of the Norwegian ALICE group, for his advice and kind help when I was working on the data acquisition system for the PHOS beam test. I am particularly grateful to Dr. Mikhail Ippolitov and Alexei Kuryaki for the time working together on the monitoring program for the DAQ system and for valuable contributions on off-line data analysis. Many thanks also to Dr. C. Soos for his guidance when writing a driver for RCU card. My thanks especially go to Dr. Anders Vestbø. It was Anders who picked me up at the airport the first day when I arrived in Bergen and helped me in all kinds of issues. Many thanks to you indeed.

I would also like to thank my colleagues and collaborators in BRAHMS. Sincerely thanks go to the scientists in the high energy heavy ion group at the Niels Bohr Institute, Denmark. I am particularly grateful to Dr. Ian Bearden, Dr. Claus Ekman Jørgensen, Dr. Peter Christensen and Dr. Djamel Ouerdane for their kind help and fruitful discussions during my stays in Copenhagen. I would like to thank Dr. Flemming Videbæk, the spokesman of the BRAHMS Collaboration, for his valuable advices and his efforts to make BRAHMS produce nice results. I am grateful to Prof. Stephen J. Sanders for his kind help to improve my presentations and language skills. A special thank goes to Dr. Jens Ivar Jørdre, my office mate with whom I shared the sweet and sour of being a Dr. Scient. student working on BRAHMS data, for always being ready to help to debug programs and also for fruitful discussions both on physics and cultures.

I would like to express my sincere thanks to Prof. Laszlo P. Csernai, Prof. Gerald Eigen, Prof. Per Osland, Prof. Johan Stadsnes and Prof. Jan S. Vaagen for their enlightening lectures. I am indebted to Prof. Xu Cai and Prof. D. C. Zhou, at the Institute of Particle Physics, Hua-Zhong Normal University, for their constant support and kind consideration in all phases of my studies in both China and Norway.

I am sincerely grateful to my wife and best friend Fang Liu and also my whole family for understanding and continuous support.

Last but not least, I would like to acknowledge the financial support by the Norwegian government and their efforts to help developing countries.

Contents

List of Figures

List of Tables

Chapter 1

Introduction to Relativistic Heavy Ion Collisions

Quantum Chromodynamics (QCD), the fundamental theory of the strong interaction, predicts a new state of matter called the Quark-Gluon Plasma (QGP). To search for and characterize such a new form of matter under extreme conditions of high energy densities and high temperatures is the main objective of relativistic heavy ion physics. In this chapter we introduce some concepts relevant to the study of relativistic heavy ion collisions.

1.1 The Strong Interaction and QCD

The universe appears to be governed by four kinds of forces: the strong force, the electromagnetic force, the weak force and the gravitational force. Strong interactions bind nucleons in nuclei which, being then dressed with electrons and bound into molecules by the much weaker electromagnetic force, give rise to the variety of the physical world.

The underlying theory of strong interactions is QCD, in which the fundamental degrees of freedom are quarks and gluons. Quarks are characterized by the flavor quantum number. Up to the present time, there are six different flavors: u (up), d (down), s (strange), c (charm), b (bottom) and t (top). In addition to fractional electric charges of $+\frac{2}{3}e$ or $-\frac{1}{3}e$, quarks carry a charge called color. Quarks can exist in three different color states: red, green and blue. Correspondingly, they can be represented by a field with three components,

$$\psi(x) = \begin{pmatrix} \psi^r(x) \\ \psi^g(x) \\ \psi^b(x) \end{pmatrix}. \tag{1.1}$$

The strong interaction between quarks is mediated by gluons that themselves carry color charge. Because of color, the strong force transmitted by gluons differs significantly from the electromagnetic force transmitted by photons. For example, gluons can couple directly to other gluons whereas photons cannot couple directly to photons. The most striking consequence is color confinement, i.e. neither quarks nor gluons can appear in isolation but only exist within color-neutral composite hadrons.

1.1.1 The QCD Lagrangian

Strong interaction is described by a local non-Abelian gauge theory of quarks and gluons in which SU(3) is the gauge group and gluons are the gauge bosons. The QCD Lagrangian is given by

$$\mathcal{L}_{QCD} = \bar{\psi}_j (i\gamma^\mu D^\mu - m_j)\psi_j - \frac{1}{4} F^a_{\mu\nu} F^{\mu\nu}_a, \tag{1.2}$$

where m_j and ψ_j are the mass and field of the quark of j-th flavor, and the covariant derivative D^μ and the gluon field tensor $F^{\mu\nu}_a$ are

$$D^\mu = \partial^\mu + igT_a G^\mu_a, \tag{1.3}$$

$$F^{\mu\nu}_a = \partial^\mu G^\nu_a - \partial^\nu G^\mu_a - g f_{abc} G^\mu_b G^\nu_c. \tag{1.4}$$

The QCD Lagrangian $\mathcal{L}$ displayed here is, in principle, a complete description of the strong interaction. But, in practice, it leads to equations that are notoriously difficult to solve. Here G^μ_a is the gluon field, with space-time indices μ and ν and color indices a, b and c. The numerical coefficients f and T_a guarantee SU(3) color symmetry. Aside from the quark masses, the coupling constant g is the only free parameter of the theory.

1.1.2 The Running Coupling Constant

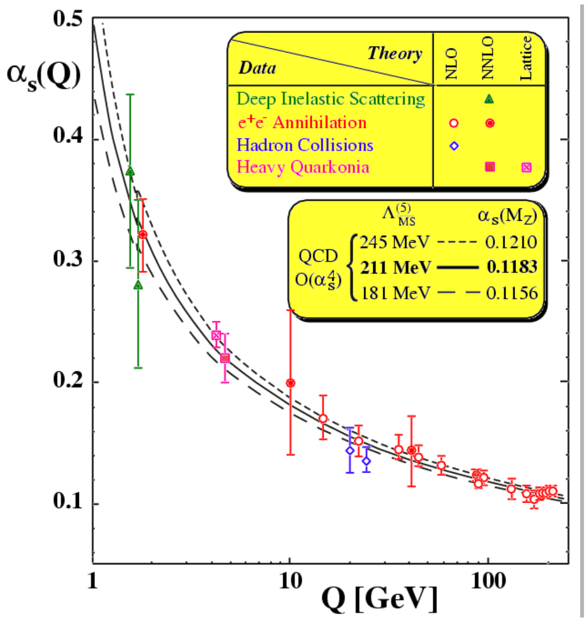

Figure 1.1: *The strong coupling constant α_s as a function of the momentum transfer Q. The figure is taken from [1].*

The running coupling constant for the strong interaction is predicted by QCD to be

$$\alpha_s(Q^2) = \frac{\alpha_0}{1 + \frac{11n_c - 2n_f}{12\pi\alpha_0}\ln(Q^2/\mu^2)} \tag{1.5}$$

where Q is the four-momentum transfer involved in the interaction process, α_0 the coupling constant for the momentum transfer scale of μ, n_c the number of color charges and n_f is the number of flavors. Thus, provided the number of quark flavors is less than 16, it follows that α_s decreases with increasing energy and momentum transfer (see Figure 1.1). When the distance scale of the interaction is small, as for example when one probes the high momentum component of the distribution of quarks, the coupling constant is small. Therefore, quarks move almost freely inside hadrons. This is the case of *asymptotic freedom*, which can be treated by perturbative theory. On the other hand, when the distance scale is large, as for example in the study of the structure of the ground state of a hadron, then the interaction strength is large. This results in the *confinement* of quarks and a non-perturbative treatment is needed.

1.1.3 Deconfinement and QGP

Asymptotic freedom implies that QCD physics gets simpler at very high temperatures. At sufficiently high temperatures and densities, QCD predicts an entirely new form of matter called quark gluon plasma (QGP). In such a plasma, quarks and gluons are no longer confined in hadrons, but behave like free single particles. In contrast to normal matter these single particles are not colorless.

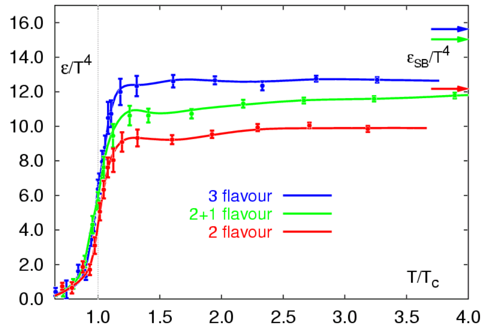

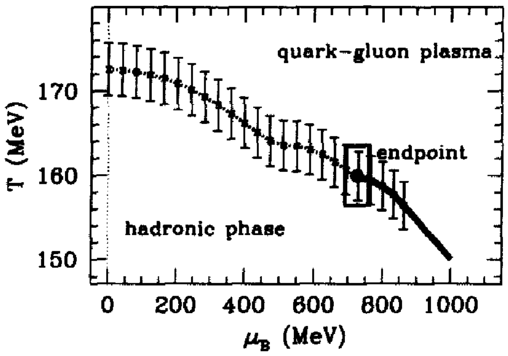

Figure 1.2: *Left: Evolution of the energy density with temperature predicted by Lattice QCD at zero baryochemical potential [2]. For all calculations, the sharp energy increase around the critical temperature T_c indicates a phase transition to QGP. Right: Phase diagram obtained by LQCD at finite baryochemical potential μ_B [3]. Dotted line at small μ_B shows the crossover, solid line at larger μ_B the first order transition. The box gives the uncertainties of the end point.*

Theoretically, the phase transition from hadronic matter to a possible QGP has been studied in lattice QCD (LQCD) calculations. As shown in the left panel of Figure 1.2, LQCD calculation at zero baryochemical potential (μ_B) predicts that at a critical temperature T_c of $\sim$ 170 MeV [2], corresponding to an energy density of $\epsilon_c \sim 1$ GeV/fm^3, nuclear matter undergoes a phase transition to a deconfined state of quarks and gluons. In addition, chiral symmetry is approximately restored and quark masses are reduced from their large effective values in hadronic matter to their small bare ones. The right panel of Figure 1.2 shows the first lattice result for QCD phase diagram at finite baryon-chemical potential. Solid line indicates a first order transition at large μ_B and dotted line shows a rapid crossover transition at smaller μ_B. It is commonly believed that a QGP was realized right after the big bang, the believed origin of our present universe. Today quark matter is expected to exist, due to high particle densities, in neutron stars. It is expected that, by means of high energy heavy ion collisions, a sufficiently large particle density and high temperature can be established to form a QGP. Figure 1.3 summarizes the present understanding about the phase diagram of hadronic matter. The chemical freeze-out temperature and the baryon chemical potential for each data point are calculated from measured particle multiplicity ratios using a statistical model [4, 5, 6].

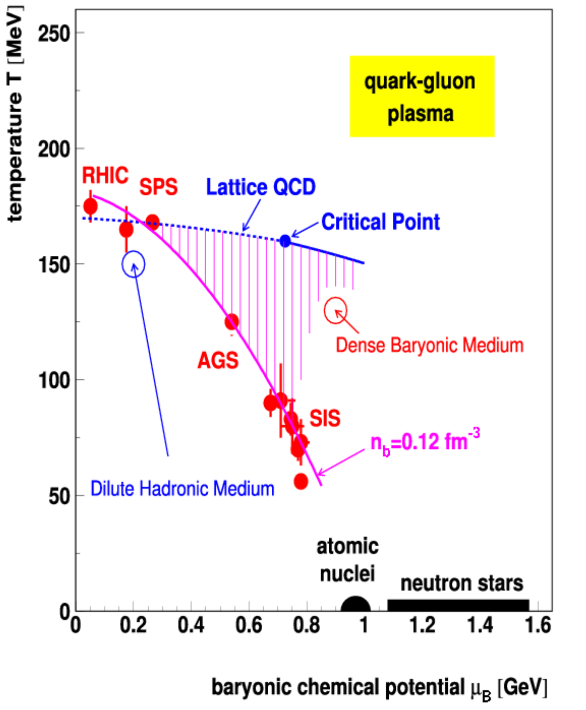

Figure 1.3: *The phase diagram summarizing the present understanding of hadronic matter and the hadron gas - QGP phase transition.*

1.2 Relativistic Heavy Ion Collisions

One of the major goals of high energy nuclear physics is to explore the phase diagram of strongly interacting matter, to study the QCD phase transition and the properties of the QGP. However, the system created in heavy ion collisions undergoes a fast dynamic evolution from the extreme initial conditions to the dilute final state. It is a theoretical challenge to understand such a fast evolving system and to characterize the QGP state. In this section, the dynamics of a heavy ion collision according to the Bjorken picture will be described after a short discussion about collision geometry. And then several different probes suggested as signatures of QGP will be briefly reviewed in section 1.2.3.

1.2.1 Collision Geometry of Heavy Ion Collisions

Regarding collision geometry of relativistic nucleus-nucleus collisions, there are several general concepts worthwhile to mention.

Nuclear density profile

A nucleus A is an object composed of A nucleons. The nucleon distribution inside the nucleus can be described by the Woods-Saxon density profile:

$$\rho(r) = \frac{\rho_0}{1 + \exp(\frac{r-r_0}{a})}. \tag{1.6}$$

For the case of Au, the parameters are $r_0 = 6.38$ fm, $\rho_0 = 0.169$ fm^{-3} and $a = 0.535$ fm from $e + A$ scattering [7]. With these parameters the integral $\int_0^\infty \rho(r) 4\pi r^2 dr$ yields approximately 197, the total number of nucleons in a Au nucleus.

Participants and spectators

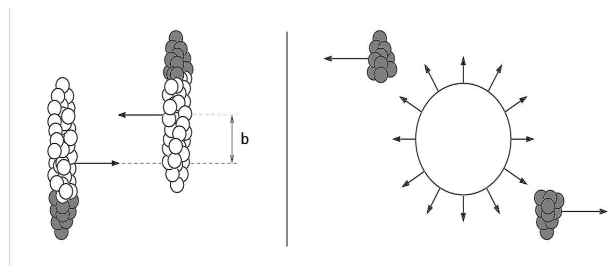

Figure 1.4: *Schematic view of a relativistic heavy-ion collision: before (left) and after (right) the collision.*

Figure 1.4 shows schematically a geometrical picture of a relativistic symmetric nucleus-nucleus ($A + A$) collision. The nuclei are Lorentz contracted in their direction of motion. The transverse distance between the center of the two colliding nuclei is called the *impact parameter* b. For a given impact parameter, only the nucleons in the overlap region of the nuclei participate in the collision. These nucleons (denoted as open circles in the left figure) are usually called *participants*, the rest that do not participate in the collision are called *spectators*. For a head on collision, $b = 0$ and the number of participants N_{part} will just be $2A$ in the hard sphere limit for an $A + A$ collision.

Due to the large size of a nucleus, multiple nucleon-nucleon collisions occur, where a nucleon in one nucleus may collide with many nucleons in the other nucleus, and in the process deposit a large amount of energy. The total number of elementary nucleon-nucleon collisions involved in a nucleus-nucleus collision is called *the number of binary collisions* N_{coll}. Both N_{part} and N_{coll} can be estimated by the Glauber model [8].

Centrality

With heavy ions a collision can be very different if the ions collide head on or only graze each other. It is commonly assumed that the more central the collision is, the more violent it is and the more outgoing particles it produces. On average, decreasing the impact parameter leads to more nucleons participating in the interaction and more produced particles. Thus the most central collision corresponds to the smallest b, the highest N_{part}, the highest N_{coll} and the highest multiplicity (see e.g. Figure 1.5). Since the geometrical probability to have a collision of impact parameter $b \pm db$ increases proportionally with $2\pi b$, theoretically one can characterize the degree of centrality C by

$$C = \frac{\int_0^{b_c} 2\pi b db}{\sigma_{inel}}, \tag{1.7}$$

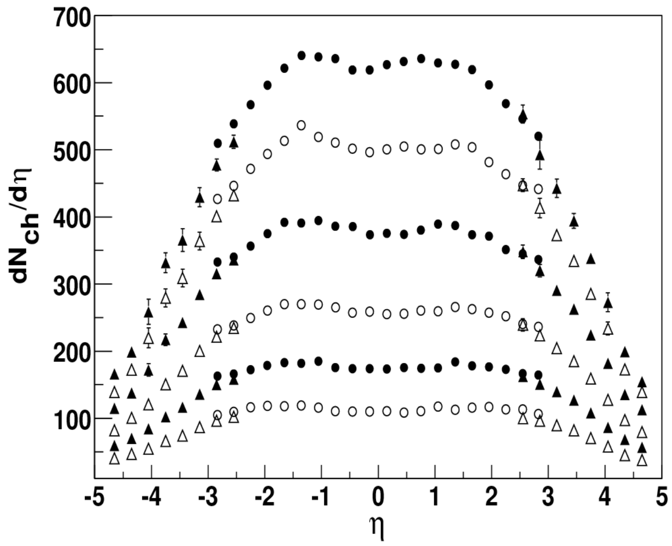

Figure 1.5: *Distribution of charged particle pseudo-rapidity density $dN_{ch}/d\eta$ in Au+Au collisions at $\sqrt{s_{NN}} = 200$ GeV measured by BRAHMS [9] for centrality range of, top to bottom, 0-5%, 5-10%, 20-30%, 30-40%.*

where σ_{inel} is the total inelastic cross section of a nucleus-nucleus collision, and b_c the impact parameter cut-off. Thus C is the probability that a collision occurs at $b < b_c$. Since the impact parameter is not directly measurable, experimentally one usually uses observables like the number of produced charged particles (charged-particle multiplicity) and/or the number of participants[1] to classify centralities. For 0-5% central Au+Au collisions, N_{part} and N_{coll} are estimated to be 357 ± 8 and 1000 ± 125, respectively [9].

[1]The number of spectators ($N_{part} = N - N_{spec}$) can be measured by Zero Degree Calorimeters.

1.2.2 Dynamics of Ultra-relativistic Heavy Ion Collisions

For ultra-relativistic heavy-ion collisions, there are two extreme scenarios with essentially different physics: stopping which assumes that baryons stemming from the projectile and the target are fully or partly stopped by each other, forming a fairly baryon rich matter in the middle of the reaction zone; and transparency which assumes that initial target and projectile baryons cannot be slowed down completely in the collision and the participants keep most of their initial momenta after the collision and leave a highly excited zone between the nuclei giving rise to a net-baryon poor fireball. Based on observations from high energy $p + p$ collisions, it is expected that the higher the collision energy the higher degree of transparency. Figure 1.6 shows the net-proton rapidity density measured at AGS [10, 11, 12], SPS [13] and RHIC [14]. The net-protons at mid-rapidity decrease as the colliding energy increases. A net-proton poor region at mid-rapidity is realized at RHIC energy.

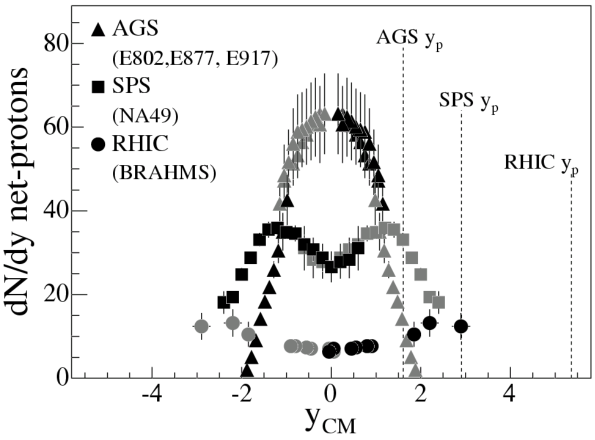

Figure 1.6: *The net-proton rapidity distribution at AGS [10, 11, 12], SPS [13] and RHIC [14].*

The evolution of the medium created in ultra-relativistic heavy ion collisions is usually described by the Bjorken picture [15], in which nuclear transparency is assumed. Figure 1.7 shows the Bjorken space-time scenario for a relativistic heavy ion collision.

Pre-equilibrium Parton-parton scattering happens. This stage features the creation of high transverse momentum (p_T) jets, $c\bar{c}$ pairs or other products of high momentum transfer processes on parton level. In addition, large cross-section soft nucleon-nucleon scatterings between the two highly Lorentz contracted nuclei help re-distribute a large fraction of the incoming kinetic energy into partonic degrees of freedom. If the energy density is well above the critical energy density ϵ_c, partons are expected in a deconfined phase but may not initially be in equilibrium. The hard processes with small cross-section are usually used as experimental probes for the hot and dense medium created in the collision.

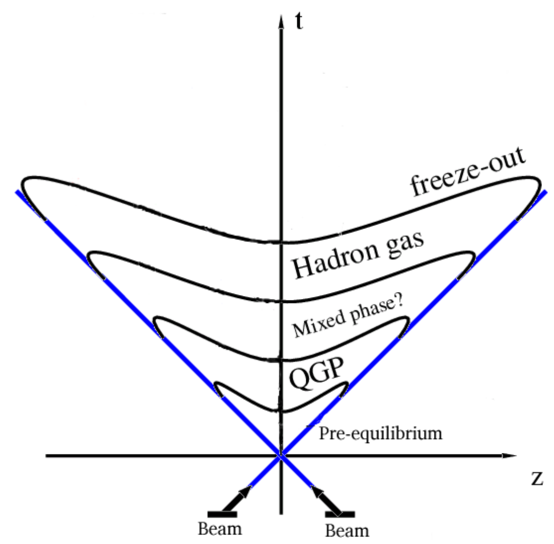

Figure 1.7: *The space-time evolution of a relativistic heavy ion collision in the Bjorken picture.*

Chemical and thermal equilibrium Subsequent multiple partonic scatterings bring the matter to local equilibrium at the proper time τ_0 and QGP is formed. The plasma then evolves according to hydrodynamics, with the possible formation of a mixed phase of QGP and hadron gas. Collective flow is expected to develop at this stage.

Hadronization and freeze-out As the plasma expands, its temperature drops. When the critical temperature T_c is reached a phase transition from QGP to hadron gas takes place. As the system cools down further so that there is not enough energy in each collision to change the different species' populations or ratios, *chemical freeze-out* of the final state particles is then reached. Eventually, when the system becomes diluted enough such that the interactions cease and the momenta of particles do not change further (*kinetic freeze-out*), hadrons stream out of the collision region.

In order to understand the collision dynamics and study the properties of QGP and the phase transition, experimentally one can only start from the measurement of final state particles. Indirect information must be inferred from the hadrons, leptons and photons produced from the collision. Hadrons are copiously produced, but interact strongly with each other well after the transition from QGP to hadrons. This tends to obscure the information they carry about the system prior to the phase transition, but they can provide information on the freeze out conditions. On the other hand, leptons and photons, which are produced at all stages of the collision and interact weakly with the rest of the system, can better reflect the properties of the system at the time they were produced. But also because they interact weakly, directly produced leptons and photons are rare in comparison to hadrons, and the information they carry can be obscured by the large background which comes from the decay of hadrons. However, many measurements have been proposed to probe of the high energy density medium created in ultra-relativistic heavy ion collisions.

1.2.3 Searching for Signatures of QGP

In general, to search for signatures of QGP one looks for differences in single-particle spectra or multi-particle correlations between collisions in which a QGP was formed and collisions in which no QGP was formed. Evaluating whether a transition occurred requires an accurate hadronic scenario as a basis for a comparison. This basis is usually established by using elementary nucleon-nucleon collisions, varying the centrality of heavy ion collisions or colliding lighter nuclei. Recent reviews of the different possible QGP signatures can be found for example in [16]. In this section we will briefly review some of the potential experimental signals that have been proposed to probe the system created in relativistic heavy ion collisions.

"Anomalous" J/ψ suppression

J/ψ is a small and tightly bound state of charm and anti-charm quarks ($c\bar{c}$). It has a radius of about 0.2 fm, much smaller than the normal hadronic scale $\Lambda_{QCD}^{-1} \simeq 1$ fm; its binding energy is with 0.6 GeV much larger than $\Lambda_{QCD} \simeq 0.2$ GeV. It therefore requires hard gluons to resolve and dissociate a J/ψ. Lattice calculation predicts that the heavy quark-quark potential $V_{q\bar{q}}$ decreases with increasing temperature as shown in Figure 1.8. At $T > T_c$, the potential is negligible, this means that the color charge gets screened and the bound state of quarks gets dissolved. So the suppression of J/ψ yields would indicate the color deconfinement or QGP formation.

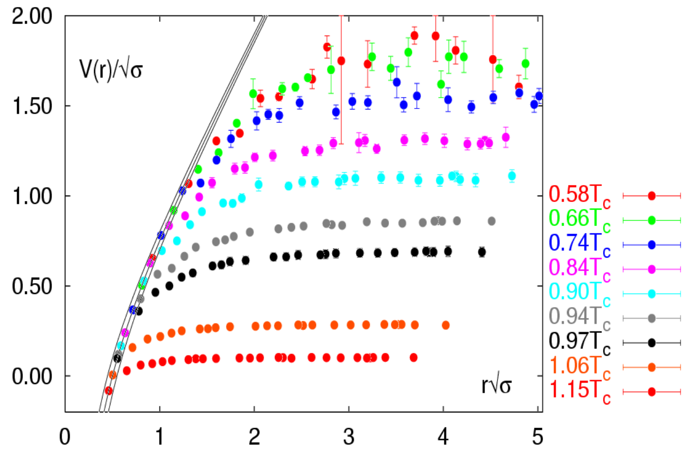

Figure 1.8: *The heavy quark effective potential at different temperatures, taken from [2]. The linear rise of the potential is weakened as one approaches the critical temperature. The solid curves show the Cornell potential $V(r) = -\alpha/r + \sigma r$ with $\alpha = 0.25 \pm 0.05$, where σ is the string tension.*

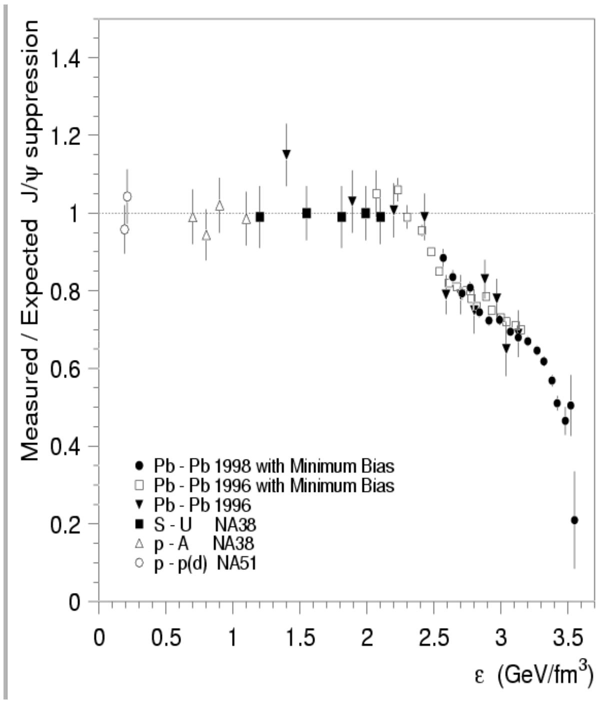

Figure 1.9: *Measured J/ψ production yields normalized to the expected yields assuming that the only source of suppression is the ordinary nuclear absorption. The figure is taken from [17].*

"Anomalous" J/ψ suppression has been reported by the NA50 collaboration for central Pb + Pb collisions at SPS [17]. Figure 1.9 shows the yields of J/ψ normalized to the expected yields assuming that the nuclear absorption is the only source of suppression. The suppression observed above the energy density $\epsilon \sim 2.3$ GeV/fm is consistent with the formation of a QGP albeit a few of non-QGP models cannot be ruled out.

In-medium hadron modification

The dileptons produced by hadron decay constitute an ideal tool to probe the medium created in relativistic heavy ion collisions, providing the hadrons actually decay inside the medium. The ρ meson, with a life-time of about 1 fm, appears to be the best candidate. Chiral symmetry restoration is expected to change the properties of hadrons as the temperature of the medium approaches the restoration point [18, 19, 20].

As shown in Figure 1.10, the dilepton mass spectrum in the region below the ρ was indeed found to differ considerably from that expected from the known hadronic sources [21], which do describe the measured distribution in p+A collisions. Thus this indicates that the in-medium resonance modification effect appears to set in in nucleus-nucleus collisions. This 'low mass dilepton enhancement' is also observed in S+U and Pb+Pb collisions, and for the latter at a beam energy of 40 GeV as well as of 160 GeV.

If at the onset of chiral symmetry restoration, the mass of ρ decrease sufficiently, then the observed effect can be accounted for [22]. But alternative scenarios have also provided

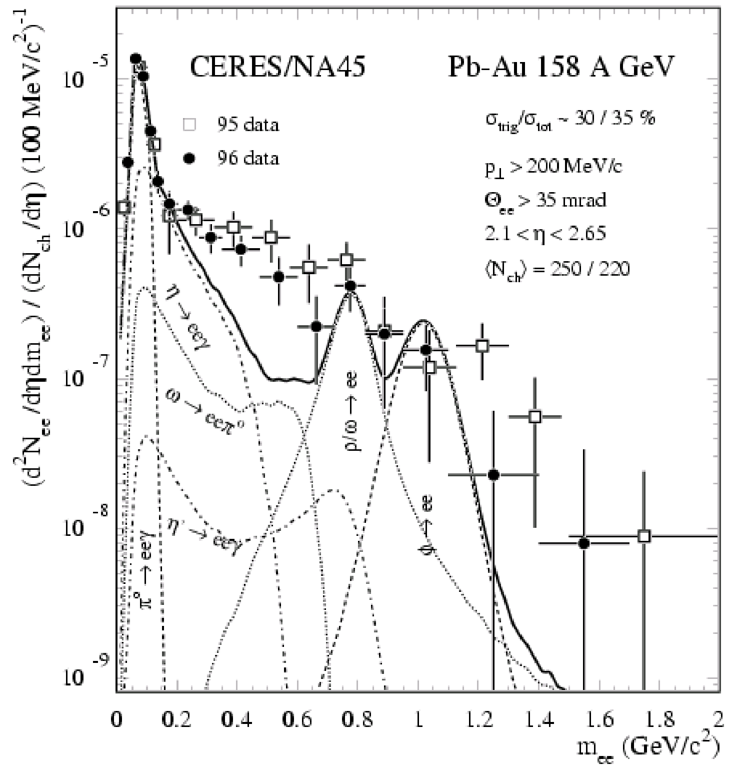

Figure 1.10: *The dilepton spectrum in Pb+Au collisions at $\sqrt{s_{NN}} = 17$ GeV, compared to the expected yields from known hadronic source [21].*

explanations. A much broader ρ, with the applicable kinematic constraints, also produces the low-mass enhancement [23].

Strangeness enhancement

Enhancement of strangeness is a frequently discussed signature of the QGP. In hadronic reactions, the production of particles containing strange quarks is normally suppressed due to the high mass of the s-quark ($m_s \simeq 170$ MeV/c^2) compared to u and d quark masses. In the presence of QGP, the gluon density is high and the chiral symmetry might be (partly) restored [28, 29] at high temperature, which results in an enhancement of the $s\bar{s}$ pair production compared to a confined medium. In particular, a chemically equilibrated deconfined state with an unusually high abundance of strange quarks favors the formation of multi-strange hadrons [30]. A large enhancement of multi-strange antibaryons has therefore been proposed as characteristic and nearly background-free signature of QGP.

Figure 1.11 shows the ratio between measured yields of (multi-)strange baryons from p+Pb, Pb+Pb and p+Be collisions at $\sqrt{s_{NN}} = 17.3$ GeV as a function of the number of participants [31]. While the ratio is consistent with unity for p+Pb yields, a clear enhancement is seen in Pb+Pb, directly related to the strangeness content on the baryon species.

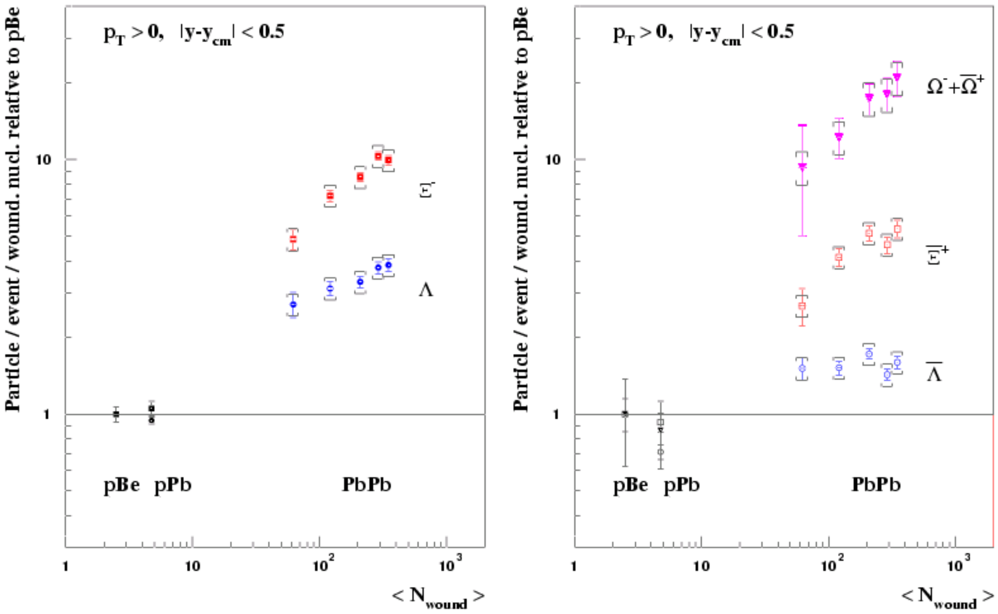

Figure 1.11: *Multi-strange baryon enhancement relative to pA collisions. The figure is taken from [31].*

Anisotropic flow

Anisotropic flow, an anisotropy of the particle azimuthal distribution in momentum space with respect to the reaction plane[2], is thought to be sensitive to the degree of thermalization achieved in the system. The spatial anisotropy of the source is largest immediately after the collision occurs. As the system evolves, the spatial anisotropy is converted by multiple interactions into a momentum-space anisotropy. The rapid expansion of the hot system destroys the original anisotropy and quenches the build-up of the momentum anisotropy. For this reason, it is believed that the final azimuthal momentum-space anisotropy is primarily built up in the initial moment of the system's evolution and thus sensitive to the early stage of the collision [24].

Figure 1.12 shows the *elliptic flow*[3] measured by STAR [25] and PHENIX [26] for π, K, p and Λ in Au+Au collisions at $\sqrt{s_{NN}} = 200$ GeV. It is impressive that the observed large elliptical flow and its hadron mass dependence agree very well with the hydro-

[2]The reaction plane is defined by the beam axis and the impact parameter $\vec{b}$.

[3]The azimuthal anisotropy of the transverse momentum distribution for a particle can be studied by expanding the azimuthal component of the particle's momentum distribution in a Fourier series,

$$\frac{dN}{d\phi} = \frac{1}{2\pi}\left[1 + 2\sum_n v_n \cos(n[\phi - \phi_0])\right]. \tag{1.8}$$

The harmonic coefficients, v_n, are anisotropy parameters and ϕ the azimuthal angle for the particle, and ϕ_0 is the azimuthal angle of the reaction plane. The first harmonic coefficient, v_1, describes *directed flow*, and the second coefficient, v_2, corresponds to *elliptic flow*. The *radial flow* component, "1", is conventionally identified from the mass dependence of the invariant m_T spectra of hadrons.

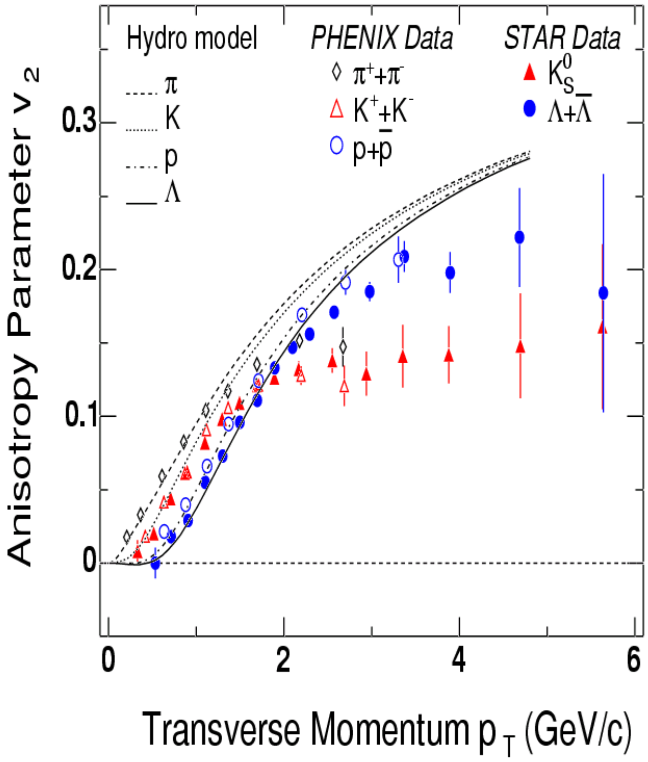

Figure 1.12: *Elliptic flow measured by STAR [25] and PHENIX [26] for* π, K, p *and* Λ *together with the hydro-dynamic model predictions [27].*

dynamical model predictions [27] at least up to about $p_T \sim 1$ GeV/c, indicating that a high degree of local thermalization is reached at early times followed by a collective hydro-dynamic expansion.

Jet quenching

The hot and dense QCD matter can be probed by its effect on a fast propagating parton, which is produced at the very beginning of the collision. If such a parton traverses a deconfined medium, it finds much harder gluons to interact with than it would in a confined medium, where the gluons are constrained by the hadronic parton distribution. As a result, jets (hard partons) will suffer a much greater energy loss per unit length in a QGP than in hadronic matter [32, 33]. This effect is called *jet quenching* and has several consequences. Of more direct relevance to particle spectra, a comparison of the transverse momentum spectrum of hadrons to appropriately scaled distributions from $p + p(\bar{p})$ and p(d)+Au collisions should show a suppression at high p_T. Furthermore, high p_T hadron correlations should show a suppression of back-to-back di-jets. More detailed discussion will follow in section 2.7.

Direct photons and dileptons

Photons and dileptons emitted during the entire evolution of the collision subsequently undergo no (strong) interactions with the medium and hence can reflect its state at the time they were produced.

1. Hard (prompt) photons and Drell-Yan dileptons, which are produced by the early hard parton-parton interactions, can provide information about the initial (pre-equilibrium) stage such as the effective initial state parton distributions. In particular, they will show any nuclear modifications (shadowing, anti-shadowing, coherence effects) of these distributions. They also indicate the initial state energy loss and initial state k_T broadening suffered by partons in normal nuclear matter. Since they do not undergo any final state strong interactions, they therefore provide a reference for studying the nuclear medium effects on e.g. jets (see γ-tagged jet section as an example).

2. Thermal photons and dileptons, which are emitted by the medium through parton or hadron interactions during its entire evolution, can serve as a thermometer for the successive stages, from QGP to final hadronic freeze-out. The functional form of thermal spectra,
$$\frac{dN}{dk_\gamma} \sim \exp(-k_\gamma/T) \tag{1.9}$$
for photon momentum k_γ, or the corresponding distributions in the dilepton mass $M_{l^+l^-}$, indicate the temperature T of the medium at the time they were emitted. Although the functional form for thermal production is the same for radiation from hadronic matter and from a QGP, the observed rates and temperatures are expected to differ in the two cases. However, also because these signals would be emitted during the entire thermal evolution, it is not straight-forward to separate different phases of origin.

3. Photons and dileptons from the decay of hadrons, which are produced at any point of the hadronic stage from the QGP-hadron transition to freeze-out, can provide information about the dense interacting hadronic matter (as ρ mesons discussed earlier) or about hadro-synthesis at the end of the strong interaction era.

1.3 Facilities: RHIC and LHC

Relativistic heavy ion collisions offer a unique tool to produce, in the laboratory, the primordial matter of the universe essentially consisting of a plasma of deconfined quarks and gluons. During the past decades, a great experimental effort has been devoted to search for such a state of matter in fixed target experiments at the Alternating Gradient Synchrotron (AGS) at the Brookhaven National Laboratory (BNL) with $\sqrt{s_{NN}} \simeq 5$ GeV and the Super Proton Synchrotron (SPS) at CERN with $\sqrt{s_{NN}} \simeq 17$ GeV. It is believed that the deconfinement boundary is established by the SPS/AGS program, but the QGP has yet to be observed unambiguously. This bodes well for studies using ultra-relativistic heavy ions at significantly higher energies at the Relativistic Heavy Ion Collider (RHIC) at BNL and at the Large Hadron Collider (LHC) at CERN. In this section a short description will be given for these two colliders.

1.3.1 RHIC

A schematic view of RHIC accelerator is shown in Figure 1.13. The AGS accelerator complex (Tandem, Booster and AGS) is used as a pre-accelerator before the beams are transferred into the RHIC rings where the beams are accelerated to their final energies. The maximum RHIC design energy $\sqrt{s_{NN}}$ is 200 GeV, about ten times higher than the top SPS energy.

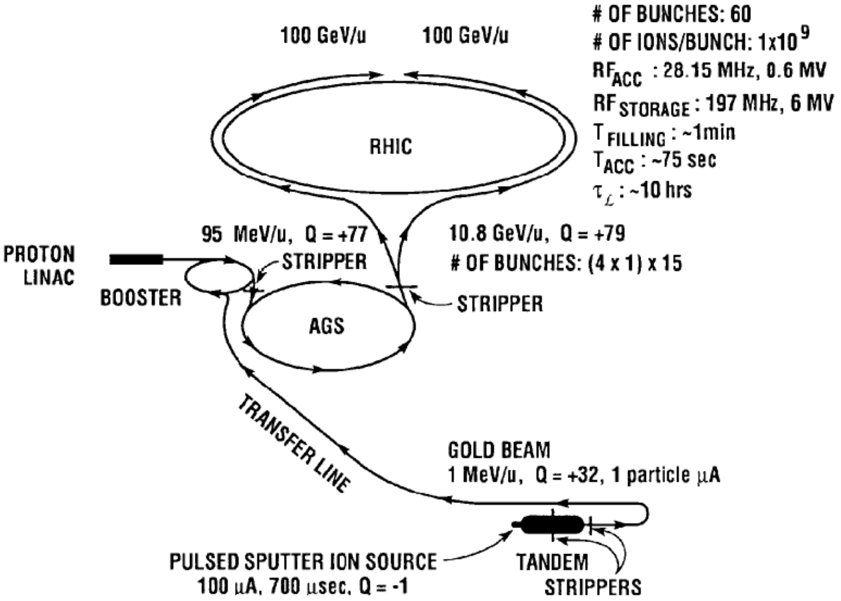

Figure 1.13: *Schematic view of the RHIC accelerator complex.*

There are six experimental halls where the beams can intersect, of which four have been instrumented. There are two large collider detectors, STAR and PHENIX. The STAR experiment concentrates on measurements of hadron production over a large solid angle in order to study global observables on an event-by-event basis. The PHENIX experiment focuses on measurements of lepton and photon production and has the capability of measuring hadrons in a limited range of pseudo-rapidity. There are two smaller experiments, PHOBOS and BRAHMS. The physical goals of the PHOBOS experiment are to measure single particle spectra and correlations between particles with low transverse momentum with a very large pseudo-rapidity coverage. The physical goal of the BRAHMS (BRoad RAnge Hadron Magnetic Spectrometers) experiment is to achieve a basic understanding of the relativistic collision at RHIC through a systematic study of charged particle production over a broad range of rapidity and transverse momentum. The physics results presented in chapter 4 are obtained with data collected by the BRAHMS experiment.

1.3.2 LHC

The Large Hadron Collider (LHC) at CERN is a particle accelerator which will probe deeper into matter than ever before. It will collide beams of protons at an energy of 14 TeV and of lead nuclei at a center-of-mass energy of 1150 TeV (5.5 ATeV). The first collisions are expected in 2007. Five experiments will study what happens when the LHC's beams collide. The CMS experiment [34] and the ATLAS experiment [35] will have the search for the Higgs boson and determination of its mass as a main purpose for their activity. The LHCb experiment [36] will be dedicated to investigating CP violation and the TOTEM experiment [37] to the measurement of total cross section, elastic scattering and diffractive processes. The ALICE (A Large Ion Collider Experiment) [38] is optimized for the study of heavy-ion collisions at $\sqrt{s_{NN}} \sim 5.5$ TeV. The prime aim of the experiment is to study in detail the behavior of matter at high densities and temperatures, in view of probing deconfinement and chiral symmetry restoration. The ALICE experiment and the spectrometer for photon detection will be described in more detail in chapter 5.

Chapter 2

High p_T Physics in Relativistic Heavy Ion Collisions

At collider energies similar to RHIC, the importance of hard or semi-hard parton scattering is clearly seen in high energy $p + p(\bar{p})$ collisions [39, 40]. They are also expected to be important in heavy-ion collisions at RHIC energies. These hard scatterings happen on a very short time scale and their production rates are calculable in perturbative QCD (pQCD). If a dense partonic matter is formed in the initial stage of a heavy-ion collision with a large volume and long life time, the high p_T partons produced will interact strongly with the matter and thus suffer large energy loss due to e.g. induced gluon radiation, resulting in a depletion of high p_T hadron yields. In this chapter, theoretical approaches to high p_T hadron production will be briefly reviewed and possible high p_T observables in relativistic heavy-ion collisions will be discussed.

2.1 The Parton Model and Structure Functions

In deep inelastic electron-proton scattering $ep \to eX$, the exchange of an energetic virtual photon (γ^*) or Z^0 with large transverse momentum squared Q^2 disintegrates the proton into hadrons. The boson interacts with a parton[1] inside the proton. As the energy and momentum transfer is large, the time scale of the hard scattering process is very short compared to that of inter-parton interactions, hence the other partons in the proton can be regarded as spectators in the scattering process. After the collision both the proton remnant and the struck quark hadronize into 'jets'.

Figure 2.1 illustrates the parton model description of the deep inelastic electron-proton collision. The quantities k and k' are the four-momenta of the incoming and outgoing electrons, p is the four-momentum of a proton with mass M, W is the mass of the recoiling system X, $q = k - k'$ is the four-momentum transfer, and the *Bjorken scaling variable* x is defined as

$$x = \frac{Q^2}{2M\nu}, \tag{2.1}$$

where $\nu = q \cdot p/M$ is the electron's energy loss in the proton rest frame. In the parton model, x is the fraction of the proton's momentum carried by the struck quark.

[1] In the context of QCD partons are associated with (anti-)quarks and gluons.

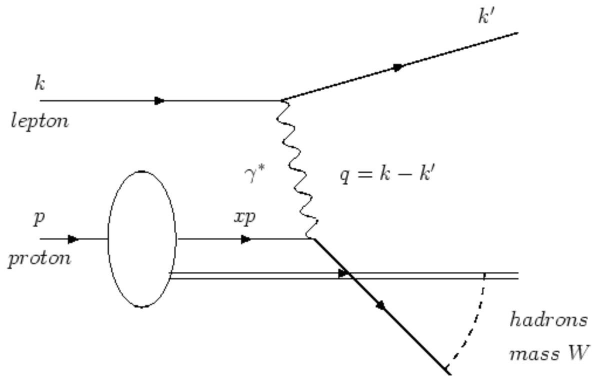

Figure 2.1: *A schematic view of the parton model description of deep in-elastic electron proton scattering.*

Assuming that in the limit of large ν and Q^2, the proton can be decomposed into free moving partons and the interaction of the electron with the proton can be viewed as the incoherent sum of its interaction with the point-like individual partons, then one can write down the general form of the differential cross section for unpolarized inclusive electron-nucleon scattering,

$$\frac{d^2\sigma}{dE'd\Omega} = \frac{4\alpha^2 E'^2}{Q^4}\left[W_2(\nu,Q^2)\cos^2(\theta/2) + 2W_1(\nu,Q^2)\sin^2(\theta/2)\right], \tag{2.2}$$

where θ is the scattering angle and E' the energy of outgoing electron. W_1 and W_2 are structure functions of the proton to represent the incalculable part of the hadronic vertex. Comparing it to the cross section of elastic scattering from a stationary, point-like, spin-$\frac{1}{2}$ object,

$$\frac{d^2\sigma}{dE'd\Omega} = \frac{4\alpha^2 E'^2}{Q^4}\left[\cos^2(\theta/2) + \frac{Q^2}{2M^2}\sin^2(\theta/2)\right]\delta(\nu - \frac{Q^2}{2M}), \tag{2.3}$$

one can extract the structure functions of the proton as

$$W_1(\nu,Q^2) = \frac{Q^2}{4M^2}\delta(\nu - \frac{Q^2}{2M}), \tag{2.4}$$

$$W_2(\nu,Q^2) = \delta(\nu - \frac{Q^2}{2M}). \tag{2.5}$$

Re-arranging the arguments of the δ function, the two dimensional structure function W_1 and W_2 can be replaced by two dimensionless structure functions:

$$F_1(x) = MW_1(\nu,Q^2), \tag{2.6}$$

$$F_2(x) = \nu W_2(\nu,Q^2). \tag{2.7}$$

One can find that in the parton model

$$F_2(x) = 2xF_1(x) = \sum_q e_q^2 x f_q(x). \tag{2.8}$$

The function $f_q(x)$ is known as the *parton distribution function* (PDF), where $q = u, \bar{u}, d, \bar{d}$ etc. The quantity $f_q(x)dx$ is the number of quarks (or anti-quarks) of a specific flavor that carry a momentum fraction between x and $x + dx$ of the proton's momentum in a frame in which the proton momentum is large. e_q is the electric charge carried by the quark (or anti-quark) in units of e. Thus, the cross section only depends on one variable, x. This property is called the *Bjorken scaling* [41]. In QCD, however, the radiation of hard gluons from the quarks leads to scaling violation which has been observed to a small degree, and the evolution of both the structure function and the parton distribution functions. As Q^2 increases, more and more gluons are radiated, which in turn split into $q\bar{q}$ pairs. This process leads both to the softening of the initial quark momentum distributions and to the growth of the gluon density and the $q\bar{q}$ sea as x decreases.

The parton distribution functions can be determined from deep inelastic lepton-nucleon scattering and related hard scattering processes initiated by nucleons. Figure 2.2 shows the unpolarized distribution functions multiplied by x using the MRST2001 parameterization [42] at scale $\mu^2 = 10$ GeV^2. Besides MRST parameterization, the popularly used parameterizations for PDFs are CTEQ [43] and GRSV [44].

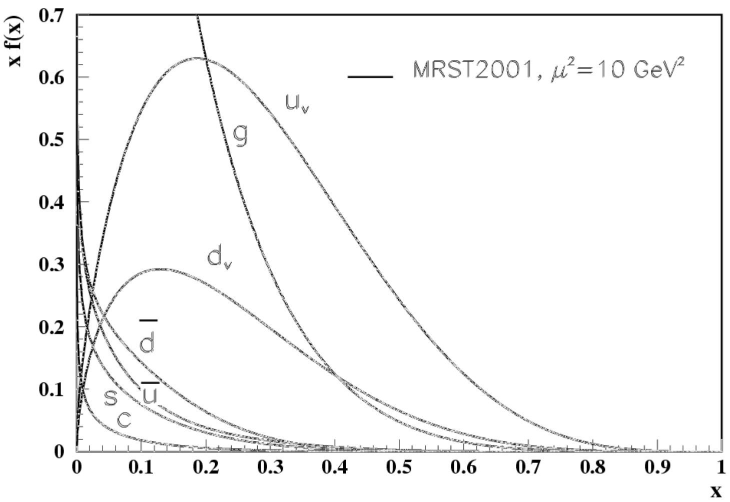

Figure 2.2: *The unpolarized parton distributions $f(x)$ (where $f = u, d, \bar{u}, \bar{d}, s, c, g$) multiplied by x using the MRST2001 parameterization [42] at a scale $\mu^2 = 10$ GeV^2.*

2.2 Fragmentation Functions

Fragmentation functions are dimensionless functions that describe the final-state single-particle energy distributions in hard scattering processes. The total e^+e^- fragmentation function for hadrons of type h in annihilation at $\sqrt{s}$, via an intermediate vector boson (γ or Z^0), is defined as

$$F^h(x_p, s) = \frac{1}{\sigma_{\text{tot}}} \frac{d\sigma}{dx_p}(e^+e^- \to hX), \tag{2.9}$$

where $x_p = 2p_h/\sqrt{s}$ and p_h is the momentum carried by the hadron. In terms of contributions from the different parton types $i = u, \bar{u}, d, \bar{d}, ..., g$,

$$F^h(x_p, s) = \sum_i \int_{x_p}^1 \frac{dz}{z} C_i(s, z, \alpha_s) D_{h/i}(x_p/z, s), \tag{2.10}$$

where $D_{h/i}$ are the *parton fragmentation functions* (PFF) and C_i the coefficient functions which are generally factorization-scheme dependent.

Parton fragmentation functions represent the probability for a parton to fragment into a particular hadron carrying a certain fraction of the parton's energy. Fragmentation functions incorporate the long distance, non-perturbative physics of the hadronization process in which the observed hadrons are formed from the final state partons of the hard scattering process and, like structure functions, cannot be calculated in pQCD, but can be evolved from a starting distribution at a defined energy scale by e.g. the DGLAP equation [45]. Fragmentation functions can be extracted from the measurements of e^+e^- fragmentation into identified particles. The most popularly used parameterizations for fragmentation functions are KKP [46], BKK [47], Kretzer [48] and BFGW [49] parameterizations.

If the fragmentation functions are combined with the cross sections for the inclusive production of each parton type in the given physical process, predictions can be made for the scaled momentum, x_p, spectra of final state hadrons.

2.3 High p_T Particle Production in $N + N$ Collisions

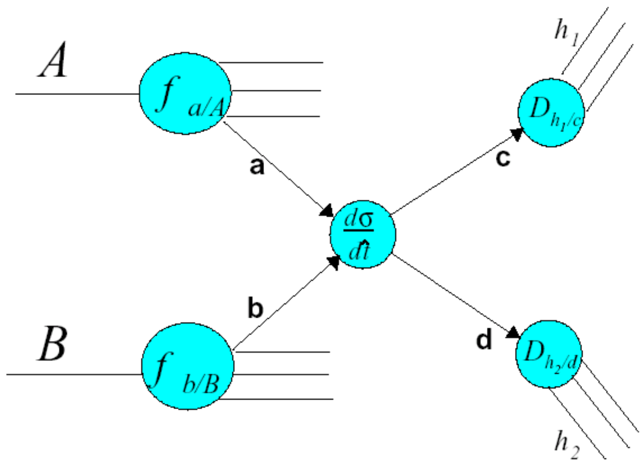

Figure 2.3: *Schematic representation of factorization theorem for a $N + N$ collision.*

In nucleon-nucleon collisions, the standard pQCD calculations of hard scattering processes rely on so called factorization theorems [50], which provide a way to separate long distance non-perturbative effects from short distance perturbative effects. Hard scattering is then described by the lowest order sub-processes which, for high p_T particles, correspond to a convolution of two-body scattering. This is shown schematically in Figure 2.3.

The corresponding expression for the inclusive differential cross section for $N+N \to h+X$ is given by

$$E_h \frac{d\sigma_h^{NN}}{dp^3} = K \sum_{abcd} \int dx_a dx_b d^2k_a d^2k_b g_N(k_a) g_N(k_b) f_{a/N}(x_a, Q_a^2) f_{b/N}(x_b, Q_b^2) \times \frac{d\sigma}{d\hat{t}}(ab \to cd) \frac{D_{h/c}(z_c, Q_c^2)}{\pi z_c}, \tag{2.11}$$

where x_a and x_b are the initial momentum fractions carried by the interacting partons a and b, $z_c = p_h/p_c$ is the momentum fraction carried by the final observable hadron, $f_{\alpha/N}(x_\alpha, Q_\alpha^2)$ is the parton distribution function of the parton of flavor α in a nucleon, and $D_{h/c}(z_c, Q_c^2)$ is the fragmentation function for the parton of flavor c into h. Here, k_a and k_b denote the intrinsic transverse momenta k_T of the colliding nucleons. The initial k_T distribution is usually assumed to be a Gaussian form

$$g_N(k_T) = \frac{e^{-k_T^2/\langle k_T^2 \rangle}}{\pi \langle k_T^2 \rangle}, \tag{2.12}$$

where the width $\langle k_T^2 \rangle$ is related to initial state radiation. The differential cross section of hard parton-parton scattering process, $\frac{d\sigma}{d\hat{t}}(ab \to cd)$, can be calculated by pQCD at leading order (LO) or the next-to-leading order (NLO) of α_s. The phenomenological K factor is introduced to mimic higher order corrections.

It turns out that the pQCD calculations are rather successful in describing high p_T particle production in high energy $N+N$ collisions [51, 52, 53]. As an example, Figure 2.4 shows the invariant differential cross section for π^0 in $p+p$ collisions at $\sqrt{s} = 200$ GeV measured by the PHENIX collaboration at RHIC [40], together with results from NLO pQCD calculations. The pQCD calculations are consistent with the data down to $p_T \sim 2$ GeV/c, indicating that the high p_T particle production in $p+p$ collisions is dominated by the fragmentation of hard-scattered partons.

2.4 Nuclear Effects on High p_T Hadron Production

Since the discovery of so called *EMC effect* by the European Muon Collaboration (EMC) at CERN in 1982 that the structure function F_2 per nucleon in iron differs significantly from that of free nucleon [54], nuclear effects on structure functions have been extensively studied both experimentally and theoretically [55]. It was such a discovery that opened a door for a systematic study of QCD dynamics in a nuclear environment, which has lead to many new QCD phenomena, e.g. shadowing, gluon saturation and Color Glass Condensate (CGC).

In this section, four nuclear effects in nuclear collisions will be discussed. The Cronin effect, nuclear shadowing and gluon saturation effect are considered as initial state effects, while jet quenching is considered to be a final state effect, which happens after the hard parton-parton scattering in a relativistic heavy-ion collision.

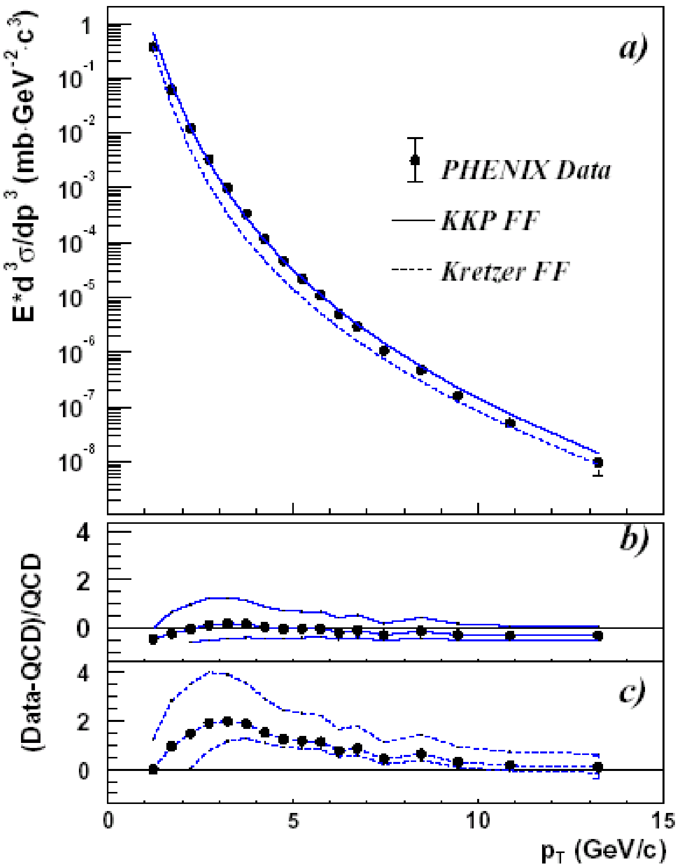

Figure 2.4: *a) The invariant π^0 spectra measured by the PHENIX experiment in $p+p$ collisions at $\sqrt{s} = 200$ GeV, together with the results from NLO pQCD calculations using KKP and Kretzer fragmentation functions. b,c) The relative difference between the data and pQCD predictions using KKP (b) and Kretzer (c) fragmentation functions with scales of $p_T/2$ (lower curve), p_T and $2p_T$ (upper curve). The figure is taken from [40].*

2.4.1 The Cronin Effect

In the mid 70s it was discovered by Cronin *et al.* [57] that high p_T particle production in $p+A$ collisions is enhanced beyond simple binary collision scaling. This enhancement is commonly referred to as the *Cronin effect*.

Due to the finite thickness of heavy nuclei, a parton may suffer multiple soft scatterings while traveling though the nuclear matter before the final hard parton-parton scattering occurs. The initial partons in general have small transverse momenta but large longitudinal momenta. The soft scatterings increase the transverse momenta of the partons and effectively broaden the k_T of the beam partons (i.e. k_T *broadening*). This k_T broadening leads to a smearing of the p_T spectra. Since the particle production cross section falls steeply toward high p_T, this smearing effect results in an enhancement of particle production at moderate p_T range ($\sim 1.5-4$ GeV/c) compared to $N+N$ collisions.

Traditionally the Cronin effect has been parameterized as

$$E\frac{d^3\sigma^{pA}}{dp^3} = E\frac{d^3\sigma^{pp}}{dp^3}A^{\alpha(p_T)}. \tag{2.13}$$

An $\alpha(p_T) > 1$ indicates an enhancement. Figure 2.5 shows $\alpha(p_T)$ measured by different fixed target experiments [58, 59, 60, 61]. There is a clear enhancement of hadron yields at $p_T > 2$ GeV/c. The Cronin effect has also been observed at $\sqrt{s_{NN}} \simeq 17$ GeV in Pb+Pb and Pb+Au collisions at SPS [13, 62].

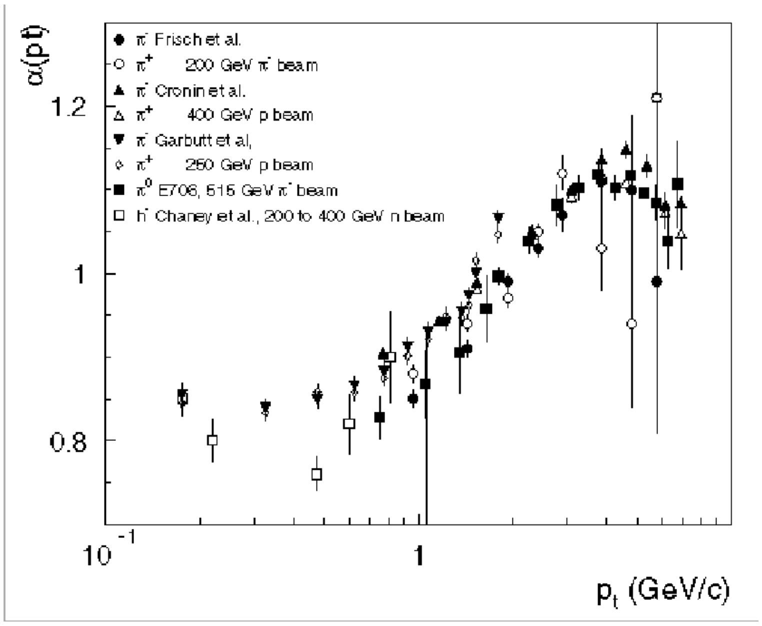

Figure 2.5: *The Cronin exponent $\alpha(p_T)$ as a function of p_T measured by different experiments. The figure is taken from [63].*

2.4.2 Nuclear Shadowing and Gluon Saturation

When the incoming nuclei are large, the composite nucleon wave functions can interact coherently among each other. A parton associated with a particular nucleon can effectively 'leak' into a neighbor and fuse with a parton of that nucleon. The physical consequences are dramatic when the Bjorken scaling variable x is either large or small as shown in Figure 2.6. If a quark receives a 'kick' from a gluon and its momentum was already large, the quark that a virtual photon scattered with may then have a value of x greater than 1. Thus the nuclear structure function extends beyond $x = 1$ and the ratio $F_2^A(x)/F_2^N(x)$ will rise as x approaches 1. On the other hand, two gluons fuse together to form a single gluon which results in reducing the effective gluon density and a sharp decrease of the gluon distribution in the nucleus at small x. This is called *gluon shadowing*. As shown in Figure 2.2, the parton density as $x \to 0$ is dominated, as Q^2 increases, by the gluon

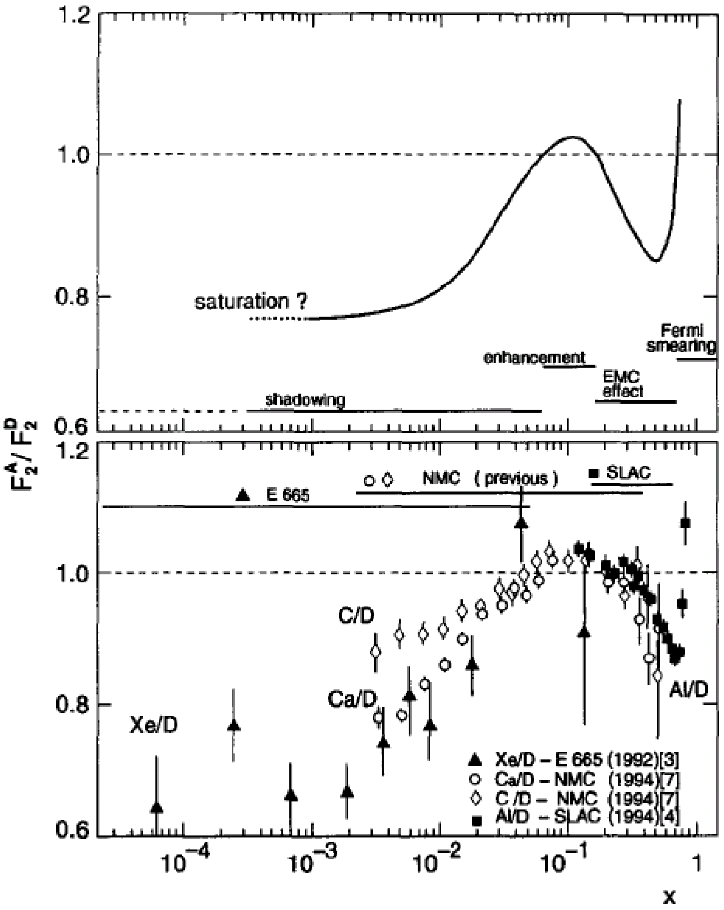

Figure 2.6: *A phenomenological curve (top) and some high precision data sets (bottom) on nuclear effects on structure function F_2. The figure is taken from [56].*

density. Gluon shadowing becomes translated, therefore, into shadowing of the structure function at low x [64].

Nuclear shadowing effects increase for small x and large nuclei. QCD analysis suggests that, at certain small x, the gluon density saturates as a result of non-linear corrections to the QCD evolution equation [64]. Due to soft gluon bremsstrahlung of hard valence partons, the total parton density increases rapidly with decreasing x. However, parton recombination, $gg \to g$, is expected to be significant when the two-parton density in the nucleus becomes very large. Consider a nucleus of radius R_A moving with high momentum: if each nucleon has a momentum p, then the nucleus has a longitudinal size $\sim 2R_A(M/p)$, where M is the nucleon mass. Gluons with a given x will have a longitudinal size of $\sim 1/(xp)$, so when $x < 1/(2MR_A)$ these gluons are forced to overlap with each other. At the same time these gluons are being probed by a photon with $q^2 = -Q^2$ and so they have a transverse size $\sim 1/Q$. As Q^2 increases the gluon density at very small x increases very rapidly and when it becomes much greater than $Q^2R_A^2$ then the calculation of the gluon density based on DGLAP evolution becomes unreliable. Mueller and Qiu [64] showed that the DGLAP evolution equations themselves are modified by the recombination of partons which results in gluon saturation at certain small x.

This parton saturation phenomenon is expected to introduce a characteristic momentum scale, the "*saturation scale*" Q_s, to determine the critical values of the momentum transfer at which the parton system becomes dense and gluon saturation sets in. The saturation scale is proportional to the gluon density and grows rapidly with $1/x$ and the number of nucleons A as

$$Q_s(x, A) \sim A^{1/3}/x^{\lambda}, \tag{2.14}$$

where $\lambda \approx 0.2$-0.3 is obtained from fits to HERA data [67]. For Q^2 smaller than or similar to Q_s^2, the non-linear effects are essential, and are expected to "saturate" the growth of the gluon distribution at a value $\mathcal{O}(1/\alpha_s)$ [66], a typical value of condensates, leading to the expectation that saturated gluons form a new form of matter called the *Color Glass Condensate* [68].

Parton shadowing and gluon saturation (or CGC) are of interest in high energy nucleus-nucleus collisions because they could influence significantly the initial conditions in reactions with a high gluon density. In order to take into account the effect of gluon shadowing on high p_T particle production, a well-known parameterization of the modification of the parton distribution is made [65] based on global fits to the most recent collection of data available and some modeling for the nuclear modification of the gluon distribution.

2.4.3 Parton Energy Loss

At the center-of-mass energy reached at RHIC, the hard scattering rate becomes quite large. Due to the large Q^2, the hard-scattered partons are created in the early stage of the collision and are expected to probe the hot, dense and strongly interacting medium created subsequently. When an energetic parton propagates through the nuclear medium, it is expected to suffer both elastic energy loss from simple scatterings and radiation energy loss due to induced gluon bremsstrahlung from multiple scattering before it hadronizes [71, 72].

The energy loss caused by elastic scattering of the propagating quark or gluon off the partons in the dense QGP has been shown [73] to be

$$-\frac{dE}{dx} \simeq \alpha_s^2 \sqrt{\epsilon}, \tag{2.15}$$

where ϵ is the energy density of the QGP. The energy loss turns out to be less than the string tension of $\mathcal{O}(1\ \mathrm{GeV/fm})$, which measures the slowing down of a high-momentum quark in cold nuclear matter [74].

However, as in quantum electrodynamics (QED), bremsstrahlung is another important source of energy loss [33]. Due to multiple inelastic scatterings and induced gluon radiation, high momentum jets and leading large p_T hadrons become depleted, quenched [71]. It has been shown [72] further that a genuine non-Abelian effect, namely, gluon rescattering is responsible for the dominant energy loss: after the gluon is radiated off the energetic parton it suffers multiple scatterings in the medium. The medium-induced energy loss suffered by an energetic parton with energy E is shown, based on asymptotic techniques (or the BDMPS approach) [72, 76] to be

$$-\frac{dE}{dx} \simeq \frac{\alpha_s}{\pi} N_c \frac{\mu^2}{\lambda} L \tag{2.16}$$

for the size of the medium $L < L_{cr} \equiv \sqrt{\lambda E/\mu^2}$ and N_c colors, where μ is a scale to characterize the medium, $\lambda = 1/(\rho\sigma)$ is the parton mean free path in the medium of density ρ with partonic cross section σ. Integrating over x leads to the total energy loss growing as L^2. While for $L > L_{cr}$, the energy loss per unit length

$$-\frac{dE}{dx} \simeq \frac{\alpha_s}{\pi} N_c \sqrt{\frac{\mu^2}{\lambda} E}, \tag{2.17}$$

which is not dependent on the size of the meduim but proportional to $\sqrt{E}$. This is similar to the QED-coherent Landau-Pomeranchuk-Migdal (LPM) suppression [75].

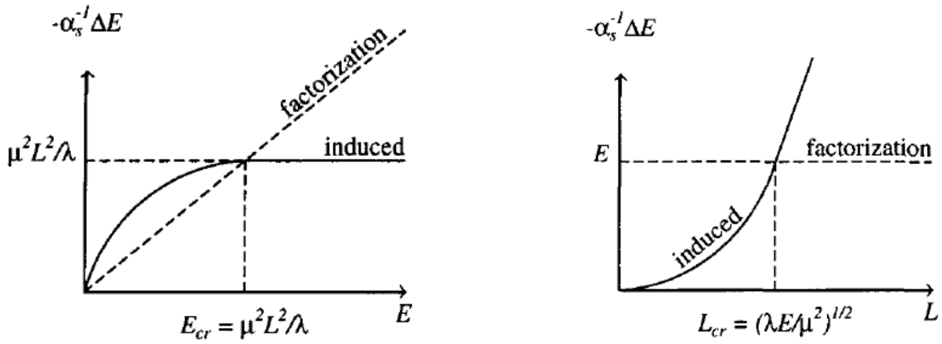

Figure 2.7: *Total induced energy loss from the BDMPS approach as a function of the parton energy E (left, with L fixed) and of the medium size L (right, with E fixed), respectively.*

Figure 2.7 shows schematically the E and L dependence of total induced energy loss ΔE with fixed L and E, respectively. Because λ depends on the density ρ of the medium, which in turn can be translated into energy density ϵ as $\rho(T) \sim T^3 \sim \epsilon^{3/4}$ for QGP with temperature T, a "smooth" increase of the total energy loss with increasing ϵ has been shown [76].

In practice, different parameterizations on parton energy loss have been derived by using different approaches to give predictions on high p_T particle production [77, 78, 79]. In the thin plasma opacity expansion framework (or the GLV approach) where the quark gluon plasma is modeled by N well-separated color-screened Yukawa potentials, Gyulassy, Levai and Vitev derived the total radiative energy loss given by [77]

$$\Delta E = \frac{C_R \alpha_s}{N(E)} \frac{L^2 \mu^2}{\lambda_g} \log \frac{E}{\mu}, \tag{2.18}$$

where C_R is a color factor and λ_g the radiated gluon mean free path.

In [78], the parton energy loss is calculated via a detailed balance approach in which both stimulated gluon emission and thermal absorption are taken into account. The effective parton energy loss is parameterized as

$$\Delta E \propto \frac{(E/\mu - 1.6)^{1.2}}{7.5 + E/\mu}. \tag{2.19}$$

The detailed balance between emission and absorption on the one hand reduces the effective parton energy loss and on the other hand increases the energy dependence.

Jeon, Jalilian-Marian and Sarcevic have investigated parton energy loss per scattering for three different cases [79]: (1) constant parton energy loss per parton scattering, $\delta E_n = const$, (2) LPM energy-dependent energy loss, $\delta E_n \sim \sqrt{E_n}$ and (3) Bethe-Heiter energy-dependent energy loss, $\delta E_n = \kappa E_n$. E_n is the energy of the parton at the n-th scattering and δE_n the energy loss in that scattering. They found that with $\kappa = 0.06$, Bethe-Heiter energy-dependent energy loss can reproduce the observed suppression of neutral pion production in Au+Au collisions at RHIC measured by the PHENIX experiment.

2.5 A pQCD-based Approach to High p_T Hadron Production

In this section we focus on hard processes in nuclear collisions and demonstrate how the various nuclear effects are treated in the pQCD inspired parton model.

2.5.1 $p + A$ Collisions

In $p + A$ collisions, the Cronin effect is attributed to the initial state multiple parton scattering, leading to k_T broadening, $\langle \Delta k_T^2 \rangle_A$. Therefore, after going through the target nucleon the initial parton k_T distribution inside a projectile nucleon becomes

$$g_A(k_T) = \frac{e^{-k_T^2/\langle k_T^2 \rangle_A}}{\pi \langle k_T^2 \rangle_A}, \tag{2.20}$$

with a broadened width

$$\langle k_T^2 \rangle_A = \langle k_T^2 \rangle + \langle \Delta k_T^2 \rangle_A. \tag{2.21}$$

The invariant inclusive hadron distribution in $p + A$ collisions can thus be given by

$$\begin{aligned} E_h \frac{d\sigma_h^{pA}}{dp^3} &= K T_A(b) \sum_{abcd} \int dx_a dx_b d^2k_a d^2k_b g_A(k_a) g_p(k_b) \\ &\times f_{a/A}(x_a, Q_a^2) f_{b/p}(x_b, Q_b^2) \\ &\times \frac{d\sigma}{d\hat{t}}(ab \to cd) \frac{D_{h/c}(z_c, Q_c^2)}{\pi z_c}. \end{aligned} \tag{2.22}$$

Here, $T_A(b)$ is the nuclear overlap integral at impact parameter b, and $T_A(b) = N_{coll}/\sigma_{inel}$, σ_{inel} is the inelastic nucleon-nucleon cross section and N_{coll} the number of binary collisions. g_A takes into account the k_T broadening, and $D_{h/c}$ is the fragmentation function. $f_{a/A}$ is the parton distribution function of parton a inside the nucleus A, which can be derived from the parton distribution functions of partons in proton $f_{a/p}$ and neutron $f_{a/n}$:

$$f_{a/A}(x_a, Q_a^2) = S_A(x_a, Q_a^2)\left[\frac{Z}{A}f_{a/p}(x_a, Q_a^2) + (1 - \frac{Z}{A})f_{a/n}(x_a, Q_a^2))\right], \tag{2.23}$$

where $S_A(x_a, Q_a^2)$ accounts for the nuclear effects due to parton shadowing and anti-shadowing effects, which can be extracted from deep inelastic lepton-nucleus scattering experimental data. Here Z and A are the number of protons and the atomic number of the nucleus, respectively.

The formula 2.22 should be applicable to $d + A$ collisions except replacing the $f_{a/p}$ by the $f_{a/d}$ and taking into account the possible nuclear shadowing effects on the parton distributions in the deuteron as well.

2.5.2 $A + B$ Collisions

In relativistic heavy ion collisions, the effect of final state parton energy loss can be studied and modeled directly by medium-modified fragmentation functions. Energy loss of the parton prior to hadronization changes the kinematic variables of the effective fragmentation function as

$$D_{h/p}^{\mathrm{medium}}(z, Q^2) = \int_0^1 d\epsilon P(\epsilon)\frac{1}{1-\epsilon}D_{h/p}(\frac{z}{1-\epsilon}, Q^2), \tag{2.24}$$

where $P(\epsilon)$ denotes the probability that a fraction ϵ of the initial energy of the hard parton is lost due to gluon radiation and multiple scattering, and $D_{h/p}$ is the parton fragmentation function in vacuum.

Thus, the invariant hadron spectrum in nucleus-nucleus collisions can be given by

$$\begin{aligned} E_h\frac{d\sigma_h^{AB}}{dp^3} &= KT_{AB}(\vec{b})\sum_{abcd}\int dx_a dx_b d^2k_a d^2k_b g_A(k_a)g_B(k_b) \\ &\times f_{a/A}(x_a, Q_a^2)f_{b/B}(x_b, Q_b^2)\frac{d\sigma}{d\hat{t}}(ab \to cd) \\ &\times \int_0^1 d\epsilon P(\epsilon)\frac{1}{1-\epsilon}\frac{D_{h/c}(z_c/(1-\epsilon), Q_c^2)}{\pi z_c}. \end{aligned} \tag{2.25}$$

Here, $D_{h/c}$ is the fragmentation function in vacuum and $T_{AB}(\vec{b})$ the nuclear overlap integral, which is a calculation of the overlap of the density profiles of two specific nuclei at a given impact parameter $\vec{b}$:

$$T_{AB}(\vec{b}) = \int d^2s dz_1 dz_2 \rho_A(\vec{s}, z_1)\rho_B(\vec{s} - \vec{b}, z_2), \tag{2.26}$$

where the z direction is the beam direction. For a given impact parameter, one calculates the product of the densities of each nucleus at a given point $\vec{s}$ and then integrates over all space.

2.6 Other High p_T Hadron Production Mechanisms

In the pQCD approach described above, it is assumed that hadrons are created by the fragmentation of energetic partons, which in turn can be calculated by pQCD. Nuclear effects are taken into account by modifying the effective nuclear structure functions and fragmentation functions. The parton fragmentation functions have been used even at low p_T in string models where the particle production in hadronic collisions is treated as the fragmentation of di-quarks. However, there has been a long-standing debate on whether particle production in the fragmentation region can better be described by fragmentation [80, 81] or recombination [82]. As an alternative or complementary to fragmentation picture, this section describes the parton recombination picture as a particle production mechanism followed by gluonic baryon junction [83] as a mechanism to enhance the baryon production rate.

2.6.1 Parton Recombination

In the parton recombination picture, those large p_T hard partons created in hard scatterings will lose momenta and virtuality through gluon radiation until a large body of quarks and anti-quarks are assembled for recombination. In the parton recombination language, the inclusive distribution of the meson M can be written as [84]

$$E\frac{d^3N_M}{dp^3} = \int \frac{d^3p_1}{E_1}\frac{d^3p_2}{E_2}\mathcal{F}(\vec{p_1},\vec{p_2})\mathcal{R}_M(\vec{p_1},\vec{p_2},\vec{p}), \tag{2.27}$$

where $\mathcal{F}(\vec{p_1},\vec{p_2})$ is the probability of having a quark with 4-momentum p_1^μ and an anti-quark with p_2^μ just before hadronization. $\mathcal{R}_M(\vec{p_1},\vec{p_2},\vec{p})$ is the probability of producing a meson at p^μ given a quark q at p_1^μ and an anti-quark $\bar{q}$ at p_2^μ. In addition, one needs only consider the partons in the same transverse plane that contains $\vec{p}$, and thus assumes

$$y_1 = y_2 = y, \tag{2.28}$$
$$\phi_1 = \phi_2 = \phi, \tag{2.29}$$

where y_1, y_2 and y are rapidities, and ϕ_1, ϕ_2 and ϕ azimuthal angles for the q, $\bar{q}$ and meson, respectively.

Since many quarks and anti-quarks are produced in a heavy-ion collision, it is reasonable to assume that the quark distribution is independent of the anti-quark distribution so that one can factorize $\mathcal{F}(\vec{p_1},\vec{p_2})$ as

$$\mathcal{F}(\vec{p_1},\vec{p_2}) = \mathcal{F}_q(\vec{p_1})\mathcal{F}_{\bar{q}}(\vec{p_2}), \tag{2.30}$$

where the functions $\mathcal{F}_q(\vec{p_1})$ and $\mathcal{F}_{\bar{q}}(\vec{p_2})$ are, respectively, distribution functions of quarks and anti-quarks in the phase space.

All together, the inclusive distribution of meson can be determined if $\mathcal{R}_M(\vec{p_1},\vec{p_2},\vec{p})$ and the parton distributions before recombination are deduced. Since the recombination of q and $\bar{q}$ into a meson is the time reversed process of displaying the meson structure, it is expected that $\mathcal{R}_M(\vec{p_1},\vec{p_2},\vec{p})$ depends on the meson structure. During hadronization the initiating q and $\bar{q}$ dress themselves and become the valence quarks of the produced hadron without significant change in their momenta. However, for the sake of simplicity, a uniform distribution is usually taken [84, 85].

Regarding the parton distributions there are different parameterizations [84, 85] (or models) used to give predictions on high p_T hadron yields. Since it is expected that, at RHIC energies, hard processes between initial nucleons lead to the production of mini-jet partons with large transverse momentum, an improved pQCD calculation [86] was used to obtain the transverse momentum distribution of those mini-jet partons in reference [85]. For partons in the dense matter (or QGP), a uniform rapidity distribution is assumed in the range $-0.5 < y < 0.5$ and an exponential form is taken for their p_T distribution. To take into account collective flow effect, the light quark and anti-quark transverse momentum distributions are given by

$$\frac{dN_{q,\bar{q}}}{d\mathbf{r_T}^2 d\mathbf{p_T}^2} = \frac{g_{q,\bar{q}}\tau m_T}{(2\pi)^3} \exp(-\frac{\gamma_T(m_T - \mathbf{p_T}\cdot\mathbf{v_T}) \mp \mu_b}{T}), \tag{2.31}$$

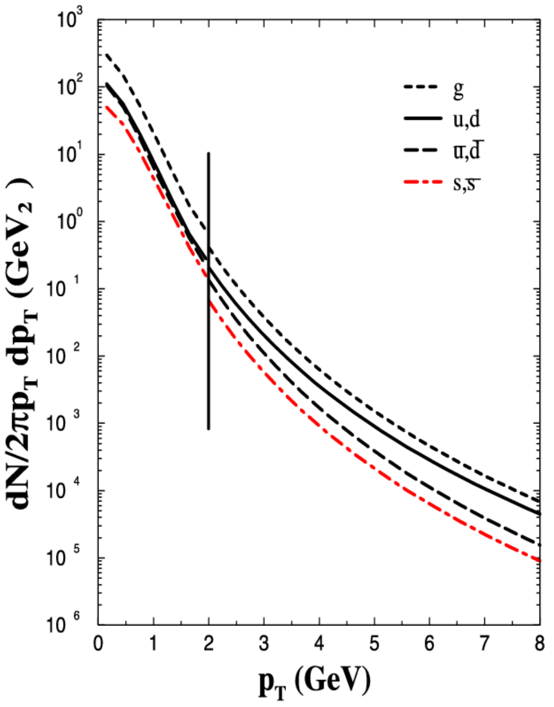

Figure 2.8: *Transverse momentum distributions of partons at hadronization in Au+Au collisions at $\sqrt{s_{NN}}$ = 200 GeV for gluons (short-dashed), u, d (solid), $\bar{u}, \bar{d}$ (dashed) as well as s and $\bar{s}$ (dash-dotted curve) quarks. Mini-jet partons have transverse momenta greater than 2 GeV, while partons from the QGP have transverse momenta below 2 GeV. The figure is taken from [85].*

where $g_q = g_{\bar{q}} = 6$ are spin-color degeneracies of light quarks and anti-quarks, and the minus and plus signs are for quarks and anti-quarks, respectively. $\mathbf{v_T} = \beta_0(\mathbf{r_T}/R_T)$ is a flow velocity, which depends on the transverse radial position $\mathbf{r_T}$ of the parton. Here, R_T

is the transverse size of the QGP at hadronization, and β_0 is the collective flow velocity of the QGP. T is the phase transition temperature, μ_b the quark baryon chemical potential, τ the proper time of the QGP at hadronization, and $\gamma_T = 1/\sqrt{1-v_T^2}$ takes into account the transverse flow effect. Figure 2.8, taken from [85], shows the transverse momentum distributions of partons at hadronization in Au+Au collisions at $\sqrt{s_{NN}} = 200$ GeV with appropriate parameters.

It is straight-forward to generalize the results for mesons to formation of baryons and anti-baryons from the parton distributions and the baryon recombination function of three quarks, as

$$E\frac{d^3N_B}{dp^3} = \int \frac{d^3p_1}{E_1}\frac{d^3p_2}{E_2}\frac{d^3p_3}{E_3}\mathcal{F}(\vec{p_1}, \vec{p_2}, \vec{p_3})\mathcal{R}_B(\vec{p_1}, \vec{p_2}, \vec{p_3}, \vec{p}), \tag{2.32}$$

with colinear conditions and momentum conservation

$$y_1 = y_2 = y_3 = y, \tag{2.33}$$

$$\phi_1 = \phi_2 = \phi_3 = \phi, \tag{2.34}$$

and

$$\vec{p_1}_T + \vec{p_2}_T + \vec{p_3}_T = \vec{p}_T. \tag{2.35}$$

Based on these formula, in principle, one should be able to calculate invariant transverse momentum spectra for various hadron species by integrating over rapidity y and azimuthal angle ϕ. It has already been shown that the parton recombination mechanism can account for the qualitative difference between the observed elliptic flows of mesons and baryons [87] and explain the observed enhancement of intermediate transverse momentum protons and anti-protons at RHIC.

2.6.2 Baryon Junction

An attractive dynamical model that was proposed to explain copious baryon and anti-baryon production at mid-rapidity is based on the existence of topological gluon configurations: baryon junctions [83, 90, 91, 92]. Gluonic baryon junctions predict long-range baryon number transport in rapidity as well as hyperon enhancement and considerable p_T enhancement relative to conventional diquark-quark string fragmentation. Figure 2.9 depicts baryon production via fragmentation of a diquark-quark string configuration (top) and of a baryon junction (bottom), respectively. In the baryon junction model, the excited baryon is described as a 'Y'-shaped string configuration. When the string undergoes fragmentation via $q\bar{q}$ production, the resulting baryon is composed of sea quarks and the valence quarks are contained in three (leading) mesons. In this mechanism the baryon then emerges with a smaller fraction of the energy available so the amount of stopping is larger. The p_T of the baryon is obtained by adding the p_T of the three sea quarks. This leads to a considerable enhancement in the baryon's transverse momentum, with the $\langle p_T^2 \rangle$ of the junction baryon increasing by a factor of three relative to that obtained from diquark-quark string configuration.

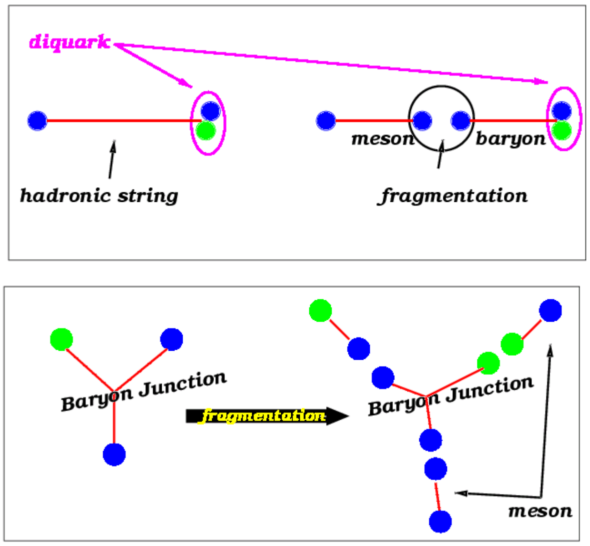

Figure 2.9: *Diagrams depicting baryon production via diquark-quark string fragmentation (top) and baryon junction mechanism (bottom).*

2.7 High p_T Observables

Even though it is impossible to observe hard scattered partons directly, they can be used as a probe for the dense medium created in relativistic heavy-ion collisions. Experimentally, one can rely on hadrons from parton fragmentation that carry the reminiscent information about the original parton. The fragments of a high energy parton usually have a small angular spread and focus around the 'leading particle' which carries a large fraction of the energy of the original hard parton. In a high energy elementary reaction, where the particle multiplicity is low, jets can be directly identified by applying an energy cut on a cluster of particles that falls within a small cone. However, in relativistic heavy-ion collisions, it is difficult to identify them in such a way due to large particle multiplicities and multi-jet production. Thus indirect methods have to be applied in order to characterize jet and extract information on nuclear medium effects on high p_T production. For example, the characteristics of hard scattered partons are rather well understood in $p+p(\bar{p})$ and $e^+ + e^-$ collisions, thus can be used as a calibrated probe for heavy-ion collisions. Furthermore, the knowledge gained from $e+p$, $e+A$ and $p+A$ collisions about the nuclear shadowing and k_T broadening can help us to disentangle various nuclear effects on high p_T particle production in relativistic heavy-ion collisions. In this section, we will discuss several proposed high p_T observables in relativistic heavy-ion collisions.

2.7.1 High p_T Hadron Suppression

When an energetic parton traverses the hot dense medium created in a relativistic heavy-ion collision, it suffers large energy loss due to gluon radiation and multiple scattering. This energy loss is expected to modify the effective parton fragmentation function which should be reflected in the p_T spectra of hadrons, e.g. a suppression of high p_T hadron yields.

Nuclear modification factor

To quantify the nuclear medium effect on the measured hadron yield in high energy nucleus-nucleus collisions, one compares it to the expectation from $N + N$ collisions, which are appropriately scaled to the large systems. As hard scatterings have a very small cross section and are expected to be incoherent, it is common to introduce the nuclear modification factor:

$$R_{AB} = \frac{d^2N^{AB}/dp_T d\eta}{(\langle N_{coll}\rangle/\sigma_{inel}^{NN})d^2\sigma^{NN}/dp_T d\eta}, \tag{2.36}$$

where $\langle N_{coll}\rangle$ is the average number of binary nucleon-nucleon collisions in the $A + B$ collisions, and σ_{inel}^{NN} is the total inelastic cross section of the $N + N$ collision. In absence of any nuclear modifications to the hard scattering, the ratio R_{AB} will be unity; thus any departure from unity indicates nuclear medium effects, and a value smaller than 1 at high p_T region indicates a suppression of high p_T yield.

2.7.2 High p_T Particle Composition

Particle abundances and ratios between them can be used to extract the chemical freeze-out condition of the fireball created in a heavy-ion collision, while particle composition at high p_T can shed light on the hadronization mechanism. For example, due to their different color representation, hard gluons are expected to lose approximately a factor of two more energy than hard quarks. Depending on the relative contribution of gluon fragmentation, this modifies the ratio of hadronic species. The ratio of anti-proton to proton $\bar{p}/p$ is expected to decrease with increasing p_T in central heavy-ion collisions if the fragmentation of the energetic partons is the dominant hadronization mechanism. Any differing from the expectation of pQCD would suggest that there are other mechanisms which contribute to high p_T particle production. Therefore studying the flavor dependence of high p_T yields is expected to be an important step in understanding high p_T particle production and transport, system evolution, and the interplay between soft and hard processes.

2.7.3 High p_T Particle Azimuthal Correlation

Hard partons fragment into jets of hadrons around the direction of parton propagation. Due to the large multiplicities and multi-jet production in central heavy-ion collisions at high energy, it is difficult to reconstruct a full jet. However, it is possible to identify jets on a statistical basis, for example, utilizing two-hadron azimuthal correlations at large transverse momentum. Since the jet fragments are focused in a small cone, they are highly correlated in angular space. Experimentally, one can trigger on a single (leading) particle with large transverse momentum (e.g. $p_T^{\rm trig} > 3$ GeV/c) and then build correlations with other particles from the same event with transverse momentum 2 GeV/$c < p_T < p_T^{\rm trig}$. Due to energy loss, energy imbalance of di-jet is expected in central heavy-ion collisions at collider energies. In the most extreme case this leads to the disappearance of one of the two jets which has a much longer in-medium path-length. As shown in Figure 2.10, data from STAR [88] show the complete disappearance of back-to-back correlated high p_T particles in the range $p_T \sim$ 2-6 GeV/c in central Au+Au collisions at $\sqrt{s} = 200$ GeV, but both the jet ($\Delta\phi = 0$) and the back-jet ($\Delta\phi = \pi$) are observed in peripheral collisions. At LHC, such studies can be extended to much higher p_T, and it is expected that the backward correlated high p_T remnant will re-appear again.

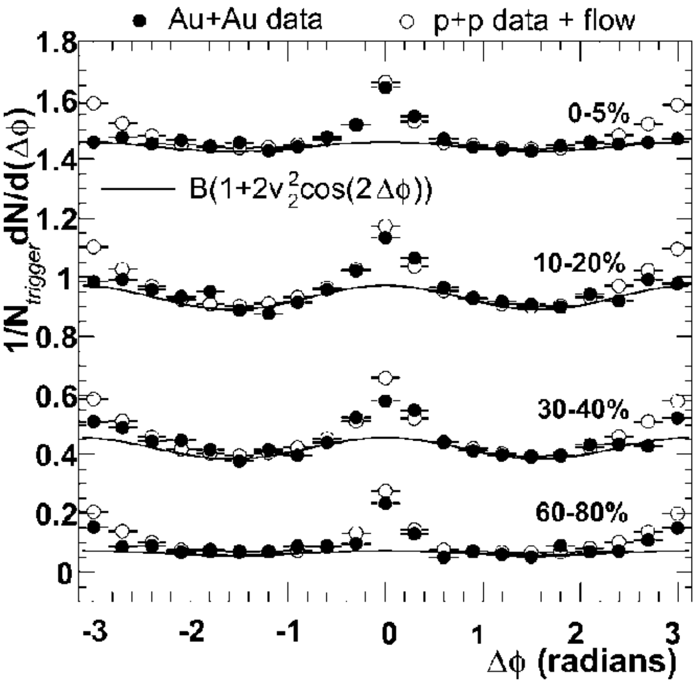

Figure 2.10: *Azimuthal correlations of high p_T particles ($0 < |\Delta\eta| < 1.4$, $4 < p_T^{trig} <$ 6 GeV/c) for Au+Au collisions (fill circles) compared to a prediction based on the $p+p$ data (open circles), with a correction for elliptic flow present in Au+Au collisions. The curves represent the contribution from elliptic flow for each centrality. The figure is taken from [88].*

2.7.4 γ-tagged Jet

The lowest order sub-processes for direct photon production are

$$q\bar{q} \rightarrow \gamma g \tag{2.37}$$

$$gq(\bar{q}) \quad \rightarrow \quad \gamma q(\bar{q}). \tag{2.38}$$

At high p_T the signature of such an event would be a hadron jet balancing an electromagnetic shower. The transverse energy of the jet is roughly the same as that of the direct photon but in the opposite transverse direction. Experimentally, one thus can benefit from this property to extract information on the energy loss of a fast parton in a hot dense medium created in relativistic heavy-ion collisions. It was proposed that one can study the modification of the jet fragmentation function by measuring the particle p_T distribution in the opposite transverse direction of a tagged direct photon [89]. In such $\gamma +$jet events, the background due to particles from the rest of the system was estimated to be well below the p_T spectrum from jet fragmentation at moderate large p_T. Therefore, one can extract the fragmentation function from the experimental data, and by comparing the extracted jet fragmentation function in $A + A$ to that in $p + p$ collisions, one can then measure the modification of the fragmentation function and determine the parton energy loss. Since the energy loss per unit path-length, dE/dx, is related to the parton density of the medium that the parton is traveling through, one can therefore estimate the parton density of the produced dense matter by measuring the energy loss of a fast parton in high energy heavy-ion collisions.

Chapter 3

The BRAHMS Experiment and Data Analysis

The data presented in this thesis were collected by the BRAHMS experiment during 2001 and 2003. The BRAHMS experimental setup and data analysis procedure will be presented in this chapter.

3.1 The BRAHMS experiment

BRAHMS consists of two magnetic spectrometers and a set of global detectors. The global detectors are devoted to measuring global properties of a collision such as the collision interaction point (IP, or the primary vertex), reaction centrality and charged-particle multiplicity, etc. The two magnetic spectrometers, the Mid-Rapidity Spectrometer (MRS) and the Forward Spectrometer (FS), are dedicated to tracking charged particles, and determining their momenta and masses. The overall layout of the experiment is shown in Figure 3.1 and the detector system has been described in detail in [93]. In this section we will focus on detectors which are relevant to this work.

The MRS

The MRS is composed of two time projection chambers (TPCs) for tracking of charged particles, a dipole magnet D5 for momentum determination, and a time-of-flight detector (TOF) for particle identification. In the middle of the 2003 run, another time-of-flight wall (TFW2) and a Čerenkov detector C4 were installed to extend the PID capabilities, however for the data presented in this thesis they are not used.

The MRS can rotate from 30° to 90° with respect to the beam line and thus covers the mid-rapidity regions. In addition, the MRS platform bearing the two TPCs (usually called as TPM1 and TPM2) and D5 can be moved backward to decrease the spectrometer acceptance. For the data presented in this thesis the MRS was positioned at 90° corresponding to rapidity 0.

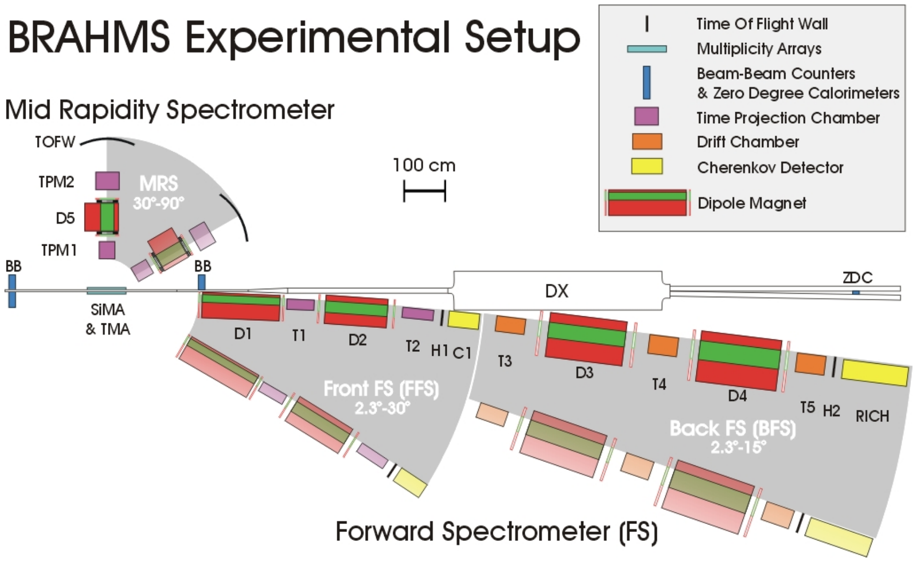

Figure 3.1: *Schematic picture of the BRAHMS detector system.*

The FS

The FS is composed of two independent parts, the Front-Forward and Back-Forward Spectrometers (FFS and BFS). The FFS can rotate in a range of $2.3° \leq \theta \leq 30°$ whereas the BFS can only be rotated in a range of $2.3° \leq \theta \leq 15°$. For the data presented in this thesis, both FFS and BFS were positioned at 12° corresponding to pseudo-rapidity $\eta \sim 2.2$, where PID is achievable to relatively high p_T with reasonable statistics.

In FFS a dipole magnet D1 is used to sweep away low momentum particles (typically below 1 GeV/c) and bend particles into the aperture of the subsequent detector. The rest of the FFS composition is identical to the MRS: two TPCs (T1 and T2) at the front and back of a dipole magnet D2, completed by a hodoscope H1 for PID and a Čerenkov threshold counter C1 which is located behind H1 to extend PID capabilities. The BFS is designed to identify very high momentum particles. To achieve this goal, the BFS is composed of three drift chambers (DCs), two dipole magnets, one hodoscope H2 and a ring imaging Čerenkov detector (RICH) at the far end.

3.1.1 Global Detectors

The global detectors include a multiplicity array, a set of Beam-Beam Counters (BBCs) and a set of Zero Degree Calorimeters (ZDCs). In d+Au and p+p 2003 runs, in addition, a set of inelasticity counters (INEL) were used to develop a minimum-bias trigger and to provide vertex position information.

Multiplicity array

The multiplicity array (MA), which is composed of an inner barrel of Si strip detectors and an outer barrel of plastic scintillator "tile" detectors, measures the energy loss of charged particles passing through the array to establish overall charged particle multiplicities and further to determine the collision centrality. The relationship between the measured multiplicities and the reaction centrality can be deduced based on model calculations and simulations of the array response as detailed in [94].

Beam-beam counters

The BBCs are deployed to characterize collisions from a global perspective, to provide the zero level trigger, the start time for the TOF measurements, and to determine the primary collision vertex position to an accuracy of approximately 1 cm. In addition, the BBCs offer a measurement of the charged particle multiplicity at large pseudo-rapidity, outside of the acceptance of the multiplicity array.

The BBCs consist of two (left and right) arrays of fast Čerenkov radiators (tubes) coupled to photo–multiplier tubes (PMTs). They are positioned at 2.19 m on each side of the nominal IP and cover a pseudo-rapidity of $2.2 < |\eta| < 4.6$. Each array is composed of two types of tubes: small tubes for a finely segmented detection and larger sized tubes which detect on average more particles at a time than small tubes. Half of the right array is missing in order to let particles fly toward the FS. When charged particles hit the BBC radiators, they emit Čerenkov photons if their velocity $v > c/n$, where the refractive index of the radiators $n \approx 1.5$. The assumption that the particles travel with the speed of light c toward both arrays allows the flight times to be converted into a distance from which the time of the collision $T0$ and the IP can be determined by

$$D = c(t_{\text{left}} + t_{\text{right}} - 2T0)/2, \tag{3.1}$$

$$z = c(t_{\text{left}} - t_{\text{right}})/2 = c((t_{\text{left}} - T0) - (t_{\text{right}} - T0))/2 \tag{3.2}$$

where the right-hand expressions can be constructed from the TDC results after transit time correction. D is the distance between left and right array and z the displacement of the primary collision vertex from the nominal IP along the beam axis. There are three methods for estimating the IP and T0 by using: (1) only large tubes, (2) only small tubes and (3) the fastest tubes. The best IP determination is obtained by using small tubes with resolution of the IP position $\sigma_{IP} = 0.7$ cm and of the T0 $\sigma_{T0} = 65$ ps, whereas the resolutions are slightly poorer for the method by using only large tubes. The method by using the signals from the fastest tubes on either side is much more prone to background and the event is therefore ignored if the IP is determined by such a method in the Au+Au data analysis. The algorithm of vertex and start-time determination by using BBCs is described in detail in [95].

Zero degree calorimeters

The ZDCs, which are common to all RHIC experiments, are designed to measure the luminosity of the colliding beams. This capability allows the beam operators to tune the machine and provides a means to compare results between different experiments. The two ZDCs are lead–tungsten calorimeters positioned at 18 m on each side of the nominal IP, behind the focusing DX magnets so that charged particles emitted from the reaction along z are bent away by the DXs and only charge neutral particles, mainly spectator neutrons, can reach the ZDCs. The ZDCs provide both energy and time signals. The time difference between the two ZDCs can be used to measure the position of the primary interaction vertex with a resolution of $\sigma_{IP} = 2.8$ cm. By requiring that it coincides with the IP determined by BBCs, events where the IP positions are inconsistent, supposedly because of background signals, can be identified and rejected. The energy signal can be used to deduce the impact parameter of the event because the neutron multiplicity is correlated with the event geometry. In the BRAHMS experiment, the coincidence of both ZDCs serves as minimum bias trigger in Au+Au collisions.

Inelasticity counters

Three pairs of INEL Counters were used to establish a minimum bias trigger for d+Au and p+p collisions in 2003 runs by detecting charged particles in the pseudo-rapidity range of $3.2 < |\eta| < 5.3$. The INEL counter consists of a plastic scintillator ring that is segmented into four pieces and arranged around the beam pipe. The counters corresponding to the innermost utilized pair are located on either side of the nominal IP at ± 155 cm. The other four counters are paired at ± 416 cm and ± 660 cm. Using the relative time-of-flight of particles hitting the left and right arrays in coincidence it is possible to determine the interaction vertex with a resolution of ~ 5 cm. The INEL trigger is estimated to select $91 \pm 3\%$ of the d+Au inelastic cross section and $71 \pm 5\%$ of the total inelastic p+p cross section according to GEANT simulations.

Event trigger

The BRAHMS trigger system, or simply trigger, determines whether an event should be recorded by the Data Acquisition (DAQ) system. For the Au+Au 2001 run, the implemented trigger logic is only based on inputs from the global detectors, due to the relatively low event rate. Table 3.1 summarizes the event trigger conditions applied during the data taking in 2001.

Trigger Id	Condition
1	BBC coincidence $N_L > 2$ AND $N_R > 2$
2	BBC coincidence $N_L > 1$ AND $N_R > 1$
3	Multiplicity trigger (TMA energy threshold)
4	ZDC coincidence and energy threshold
5	Vertex trigger (ZDC) $\rightarrow |z_{IP}| < 25$ cm
6	Trigger 3 AND Trigger 5
7	Pulser trigger for pedestal runs
8	1 Hz synchronization trigger

Table 3.1: *Trigger conditions used during Au+Au 2001 data taking. N_L and N_R are the numbers of tubes with hits in the left and right array of the BBCs, respectively.*

Due to the low number of tracks per p+p and d+Au collisions, it is essential to deploy spectrometer triggers to effectively select events with tracks in the spectrometers. In addition to INEL counters used to develop a minimum bias trigger for d+Au and p+p collisions, two start trigger and timing counters have been added to the detector system.

One is a 3 slat counter (TD1) in front of D1, the other called TMrsT0 is a 4 slat counter just across the front of TPM1. Signals from these counters combined with signals from hodoscopes form highly efficient spectrometer triggers. Table 3.2 summarizes the event trigger conditions applied during the data taking in d+Au and p+p 2003 runs.

Trigger Id	Condition
1	BBC coincidence $N_L \geq 1$ AND $N_R \geq 1$
2	BFS (INEL AND TD1 AND H1 AND H2)
3	MRS (INEL AND TMrsT0 AND TOFW)
4	ZDC (peripheral)
5	INEL (minimum bias trigger)
6	FFS (INEL AND TD1 AND H1)
7	Pulser trigger for pedestal runs
8	1 Hz synchronization trigger

Table 3.2: *Trigger conditions used during d+Au and p+p 2003 data taking. N_L and N_R are the numbers of tubes with hits in the left and right array of the BBCs, respectively.*

A recorded event is thus characterized by a trigger word with 16 bits. The lower 8 bits (0-7 bit) are set to 1 or 0 depending on whether the trigger condition is fulfilled, while the higher 8 bits are set to 1 only when the scale-down factor is met for the corresponding trigger. For example, if trigger 5 events are scaled down by factor of 2000, then every 2000 times the trigger 5 condition is fulfilled bit 12 will be set to 1 and the event will be recorded by the DAQ system.

3.1.2 Tracking Detectors

Several TPCs and Drift Chambers (DCs) are dedicated to tracking, i.e. to the reconstruction of the trajectory of charged particles through the spectrometer. Firstly tracking is done in all tracking chambers and local tracks are found. By matching the local tracks across a dipole magnet using simple geometrical constraints, a global track is identified as a collection of matched local tracks between different tracking chambers. From the bending angles in each magnet the momentum of the particle can be determined.

Time projection chambers

There are four TPCs: two in the MRS and the other two in the FFS. TPCs are designed to provide a three-dimensional measurement of charged particle trajectories with high position resolution. When a charged particle passes through the TPC, it will lose energy by ionizing the gas and create electrons along its trajectory. Electrons created by ionization then drift toward the top due to a homogeneous electrical field inside the TPC active volume. At the very top the electrons are quickly accelerated toward an anode wire at +1200 V to create an avalanche. The anode wires collect these electrons and the ion cloud induces a signal on the readout pad-row. When the drift velocity v_{drift} of the electrons is constant, the drift time is proportional to the drift distance. The mapping of row, pad and time leads to three-dimensional space points. Figure 3.2 shows schematically the principles of a TPC. The main characteristics of the four BRAHMS TPCs are given in Table 3.3. Detailed description of the TPCs can be found in [93].

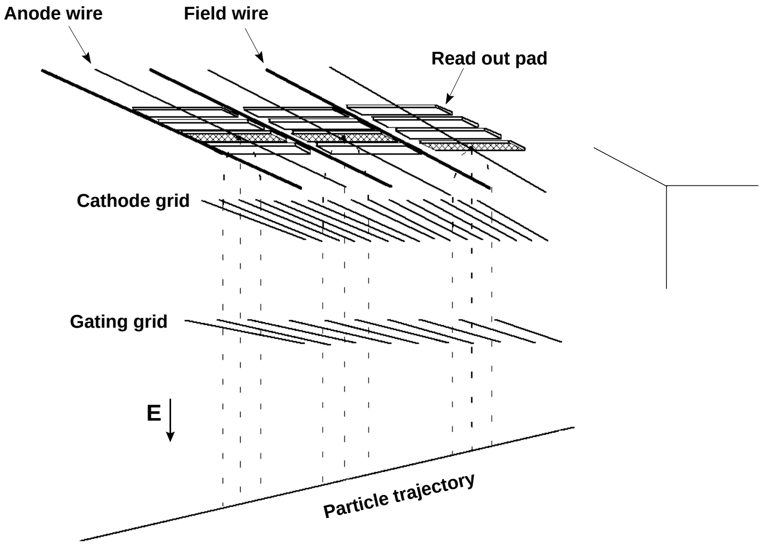

Figure 3.2: Schematic picture of the TPC readout plane and electron drift lines.

Name	Length (cm)	Width (cm)	Height (cm)	Gas mixture	N_{row}	N_{pads}/row	$\langle v_{drift} \rangle$ (cm/μs)	$\langle \sigma_x \rangle$ (mm)	$\langle \sigma_y \rangle$ (mm)
T1	56.0	33.6	19.8	Ar–CO_2	10 (14)	96	1.8	0.38	0.40
T2	75.5	39.6	19.8	Ar–CO_2	8 (14)	112	1.8	0.37	0.41
TPM1	36.6	38.4	20.0	Ar–CO_2	12 (12)	96	1.7	0.31	0.43
TPM2	50.0	67.7	19.8	Ar–CO_2	10 (20)	144	1.6	0.39	0.49

Table 3.3: *Main characteristics of the four BRAHMS TPCs. N_{row} the number of instrumented (total) pad rows, N_{pad}/row the number of pads per row, $\langle v_{drift} \rangle$ is the measured average electron drift velocity along the drift lines (y direction) and the $\langle \sigma \rangle$s are the one-particle resolutions averaged over rows. The gas mixture is in the proportion of 90:10.*

Drift chambers

Three drift chambers (T3, T4 and T5) have been employed in the BFS of BRAHMS. Each of them is composed of three modules with 8-10 detection planes, which consist of planes of anode/cathode wires and field wires. The wire directions are x, y, u and v, where x is in the horizontal direction and y in the vertical direction, while u and v are $+$ and $-18°$ relative to the y-direction. Each x- and y-plane is followed by another plane with the same wire orientation, but shifted by a quarter cell width to remove right-left ambiguities.

When a charged particle traverses the detector it ionizes the gas and the liberated electrons drift to the anode wire along the electrical field line induced by the field and cathode wires. Near the anode wire an avalanche of electron-ion pairs will take place and a signal will be induced in the anode wire. When the drift time in the DC is known the position of the track in the direction perpendicular to the wires can be determined with a position resolution $\sigma \simeq 100\ \mu$m. By combining track position in different plane a local track can be reconstructed. More details on the DC design and performance can be found in [96].

Local tracking

The BRAHMS tracking chambers measure pieces of charged particle trajectories that consist of sets of points called track hits. The local tracking is by definition the construction of these points and the subsequent linear fit leading to straight track segments in the chamber. The TPC local tracking has been described in great detail in [14] and the DC tracking has been explained in [96].

Track matching and momentum determination

After local tracking in the TPCs and DCs, the straight line local tracks, found in the tracking detectors, are matched in the intervening magnet and the particle momentum is determined using an effective edge approximation[1]. When the entrance and exit points of the magnet are known for a pair of tracks, a matching plane is by definition centered at the mid-point between the entrance and exit, perpendicular to the horizontal component of a line connecting the entrance and exit, see Figure 3.3. Each local track is projected to the matching plane, and the vertical position y, the vertical slope[2] α_y and the polar angle θ (in xz plane) of the track with respect to the matching plane are calculated. The tracks are then matched in these three parameters by requiring that the difference of each variable is within a 3σ cut, where the width is found by fitting the difference with a Gaussian. The track matching has been described in more detail in [14, 95].

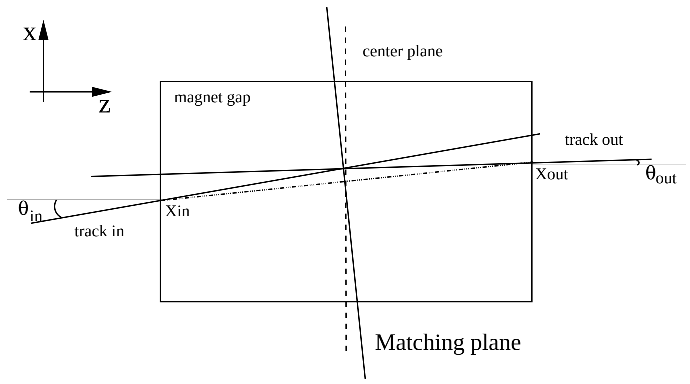

Figure 3.3: *Schematic view of track matching.*

[1]The effective edge approximation assumes that the magnetic field outside the physical gap is the same as inside such that the integral Bdl is the same as the measured.

[2]It is the difference of y positions between intersection point and the entrance (exit) divided by the distance between intersection point and the entrance (exit).

If the local tracks are matched up the momentum can be calculated assuming a unit charge as:

$$p = \frac{B\Delta L}{(\sin\theta_{\text{out}} - \sin\theta_{\text{in}})\sqrt{1-\alpha_y^2}} \tag{3.3}$$

where B and ΔL are the magnitude and the length of the magnetic field in the effective edge approximation, θ_{out} and θ_{in} are defined as in Figure 3.3, and α_y is the averaged vertical slope of the tracks. In the small angle limit,

$$p \approx \frac{B\Delta L}{\Delta\theta}, \tag{3.4}$$

where $\Delta\theta$ is the bending angle. The momentum resolution is then determined by the angle resolution as:

$$\frac{\sigma_p}{p} = \frac{\sigma_{\Delta\theta}}{\Delta\theta} = \sigma_{\Delta\theta}\frac{p}{B\Delta L}, \tag{3.5}$$

and the angle resolution $\sigma_{\Delta\theta}$ can be determined from zero-field runs.

3.1.3 PID detectors

In BRAHMS there are two types of PID detectors, TOF detectors and Čerenkov detectors. By combining the momentum and the corresponding TOF or Čerenkov signal appropriately, one can determine the particle mass based on:

$$p = \frac{m\beta c}{\sqrt{1-\beta^2}}, \tag{3.6}$$

where m is the mass and $\beta = v/c$ the velocity of the particle.

TOF detectors

There are three TOF "walls" in BRAHMS, one in the MRS (TOFW)[3] and two in the FS (H1 and H2). All three are composed of a number of vertical plastic scintillator slats readout by a PMT at each end of each slat. When the path length l of the track is determined and the time-of-flight has been measured, the velocity can be calculated as $\beta = l/ct_{\text{TOF}}$, where t_{TOF} is the time of flight. Once the particle velocity β and momentum p are known, the mass squared m^2 can be calculated (in $c = \hbar = 1$) as:

$$m^2 = p^2(\frac{1}{\beta^2} - 1). \tag{3.7}$$

So, in order to extract a meaningful PID from the TOF information, it is essential to determine the path length and as well as the start time.

[3]The second time-of-flight wall (TFW2) has been installed during d+Au and p+p 2003 runs, but it is not used in the present analysis.

Čerenkov detectors

In the FS, two Čerenkov detectors are used to extend the PID capability to higher momentum. When a charged particle traverses a medium of index of refraction $n > 1$ it emits light if its velocity v exceeds the speed of light in the medium. The light emission angle $\theta_{\rm ch}$ is

$$\cos\theta_{\rm ch} = \frac{1}{\beta n} \leq 1. \tag{3.8}$$

Thus, charged particles emit Čerenkov light above well defined momentum thresholds,

$$p_{\rm th} = \frac{m}{\sqrt{n^2 - 1}}, \tag{3.9}$$

which depends on the particle mass m and the refractive index. The higher the particle mass, the higher the momentum threshold; the larger the index of refraction, the lower the momentum threshold. The number of Čerenkov radiated photons when a charged particle crosses a radiation path L depends on its charge Z as

$$N_\gamma \propto Z^2 L(1 - \frac{1}{\beta^2 n^2}). \tag{3.10}$$

In the FFS a threshold Čerenkov counter C1, which is located behind H1, can be used to discriminate pions from kaons and protons due to the relatively low pion momentum threshold (~ 3.1 GeV/c) and high kaon threshold (~ 9 GeV/c). The Ring Imaging Čerenkov (RICH), which is situated at the far end of the FS in a low multiplicity environment of one or two tracks per event, can extend the PID capability to very high momenta. In the RICH the light emitted by charged particles is focused by a spherical mirror at the back of the detector as a ring onto a finely segmented image plane oriented at twice the mirror's focal angle and located at a distance equal to the focal length (see Figure 3.4). The radius r of the ring is related to the emission angle as

$$r = L\tan\theta_{\rm ch}, \tag{3.11}$$

where L is the focal length of the spherical mirror. Together with Eq. 3.8 a relation between the ring radius, the momentum p, the refractive index n and the mass m is given as

$$\begin{aligned} r &= L\sqrt{n^2\beta^2 - 1} \\ &= L\sqrt{\frac{n^2 p^2}{p^2 + m^2} - 1}. \end{aligned} \tag{3.12}$$

Above the momentum threshold a charged particle with smaller mass will give a bigger ring with a certain momentum as shown in Figure 3.5.

The RICH detector can identify pions with momenta starting at ~ 2.4 GeV/c. The ring radii of pions and kaons can be well distinguished up to 18 GeV/c. And protons can be identified from 9 GeV/c up to 30 GeV/c.

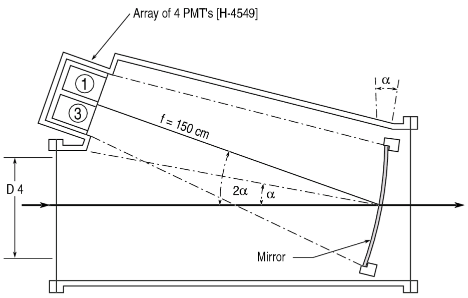

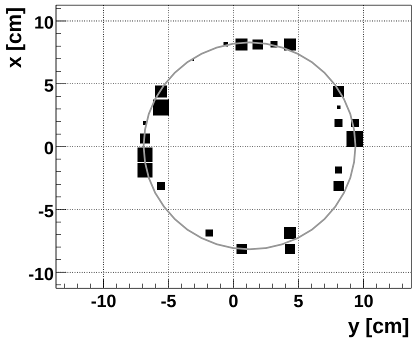

Figure 3.4: *Left: Schematic side view of RICH. Right: A reconstructed ring in the RICH detector.*

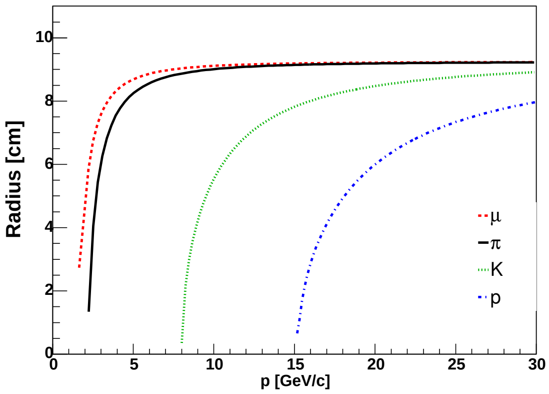

Figure 3.5: *Ring radius versus particle momentum with* $n = 1.00190$ *for different particle types calculated by using formula 3.12.*

3.2 Data Analysis

Data presented here were collected during 2001 for Au+Au collisions and 2003 for d+Au and p+p collisions at $\sqrt{s_{NN}} = 200$ GeV. This section describes the procedure from data selection to the deduction of the high p_T spectra at mid-rapidity ($\eta = 0$) and forward rapidity ($\eta = 2.2$) for charged pions and (anti-)protons.

3.2.1 Data Selection

Event selection and centrality

Trigger 5 and trigger 6 events as defined in Table 3.1 are selected for Au+Au collisions. Trigger 5, which selects events in a vertex range of -25 cm to 25 cm from the nominate IP, is based on a narrow time difference between left and right beam-beam counters corresponding to the ~ 0-60% central events. Trigger 6 is based on trigger 5 and an energy threshold in the tile multiplicity array corresponding to the ~ 20% most central events. The centrality distribution[4] of such events is shown in Figure 3.6. The distribution of trigger 6 events is rather flat from 0-20%, thus the data analyses for 0-10% and 10-20% centralities are based on trigger 6 events, while for centralities of 20-40% and 40-60% trigger 5 events are selected. The corresponding values of $\langle N_{coll}\rangle$ and $\langle N_{part}\rangle$ are listed in Table 3.4 for the four different centrality classes based on HIJING model calculations.

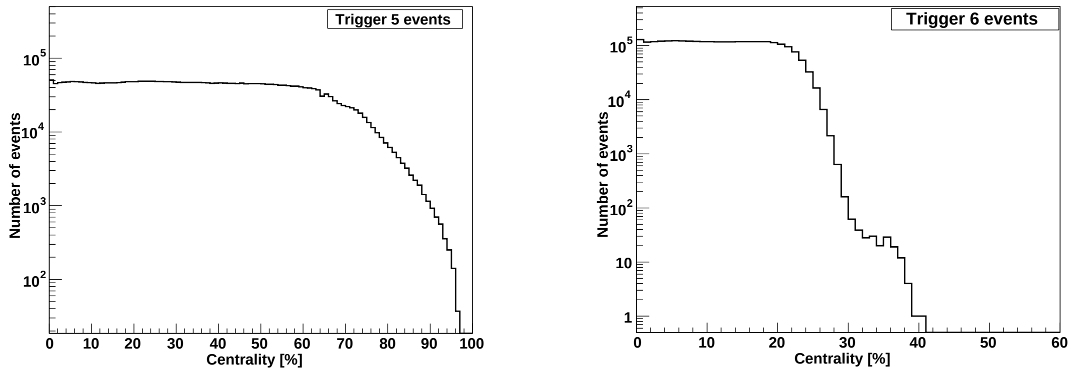

Figure 3.6: *Centrality distribution of trigger 5 (left) and 6 (right) events for Au+Au collisions at* $\sqrt{s_{NN}} = 200$ *GeV.*

Centrality	$\langle N_{coll}\rangle$	$\langle N_{part}\rangle$
0-10%	897±117	332±10
10-20%	552±100	239±10
20-40%	259±51	141±9
40-60%	78±26	59±8

Table 3.4: *Centrality classes and the corresponding values of* $\langle N_{coll}\rangle$ *and* $\langle N_{part}\rangle$ *for Au+Au collisions at* $\sqrt{s_{NN}} = 200$ *GeV.*

Because of the trigger efficiency limits and vertex dependence of the geometrical acceptance of the spectrometers, a cut on the location of the collision vertex has to be applied. Only events within the range of $|z_{\rm vtx}| < 20$ (15) cm are selected for the FS (MRS) analysis. As shown in Figure 3.7, the vertex positions determined by the ZDCs and BBCs are strongly correlated, events are rejected if the vertex $z_{\rm ZDC}$ is not consistent with $z_{\rm BB}$. A 3σ cut on the differences $(z_{\rm BB} - z_{\rm ZDC})$ is applied for each run based on a Gaussian fit around the mean difference between the vertex z positions determined by BBCs and ZDCs.

For d+Au and p+p collisions, trigger 2, trigger 3 and trigger 5 events as defined in Table 3.2 are selected for the present analysis. Trigger 2 and 3 are spectrometer

[4]Centrality is determined from the charged-particle multiplicity obtained from MA and the determination procedures are detailed in [94]

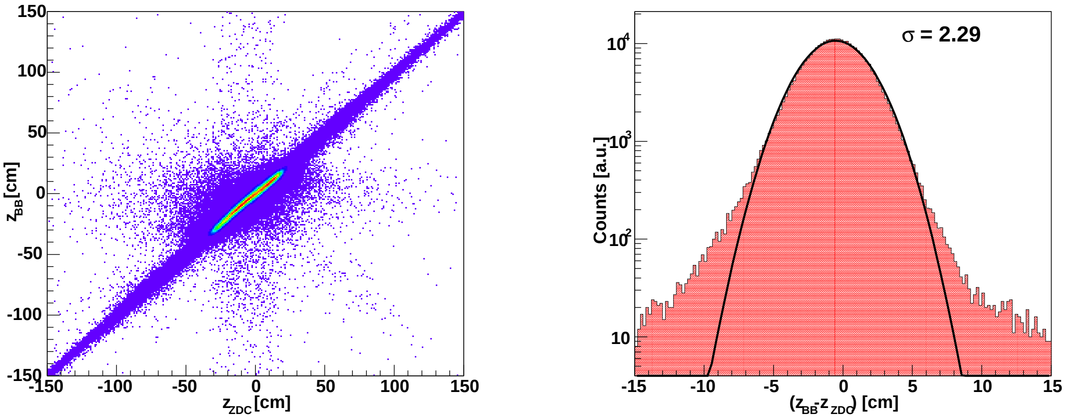

Figure 3.7: *Correlation between vertex measurements by BBCs and ZDCs.*

triggers triggering respectively on FS and MRS tracks, while trigger 5 is a minimum-bias trigger based on signals from INEL counters. Figure 3.8 shows the centrality distribution of trigger 5 events for d+Au collisions. Table 3.5 lists the centrality classes and their corresponding values of $\langle N_{coll} \rangle$ and $\langle N_{part} \rangle$ for d+Au collisions at $\sqrt{s_{NN}} = 200$ GeV.

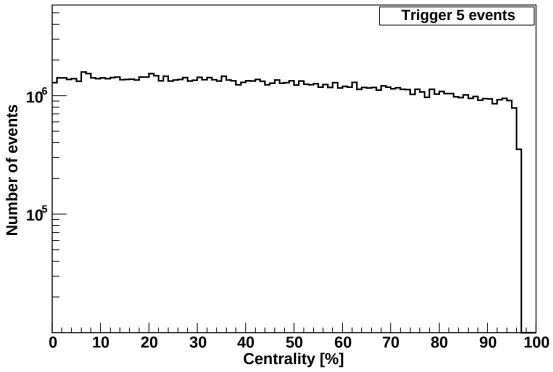

Figure 3.8: *Centrality distribution of trigger 5 events for d+Au collisions at* $\sqrt{s_{NN}} = 200$ *GeV.*

Track selection

In order to remove background or secondary particles, tracks are extrapolated back to the beam pipe line and required to originate within a given distance from the IP determined by BBCs for Au+Au or INEL counters for d+Au and p+p collisions. To determine the cut condition all tracks are projected back to a plane containing the IP. As shown in Figure 3.9, the plane is $x = 0$ for MRS tracks and $z = z_{\text{IP}}$ for FS tracks, where z_{IP} is

Centrality	$\langle N_{coll} \rangle$	$\langle N_{part} \rangle$
0-30%	12.5±1.	13.5±1.1
30-60%	7.1±0.8	8.3±0.9
60-92%	2.1±0.5	2.2±0.6
min. bias	7.2±0.4	8.0±0.5

Table 3.5: *Centrality classes and the corresponding values of $\langle N_{coll} \rangle$ and $\langle N_{part} \rangle$ for d+Au collisions at $\sqrt{s_{NN}} = 200$ GeV.*

vertex position determined by BBCs or INEL counters[5]. The intersection point is used as *track vertex*.

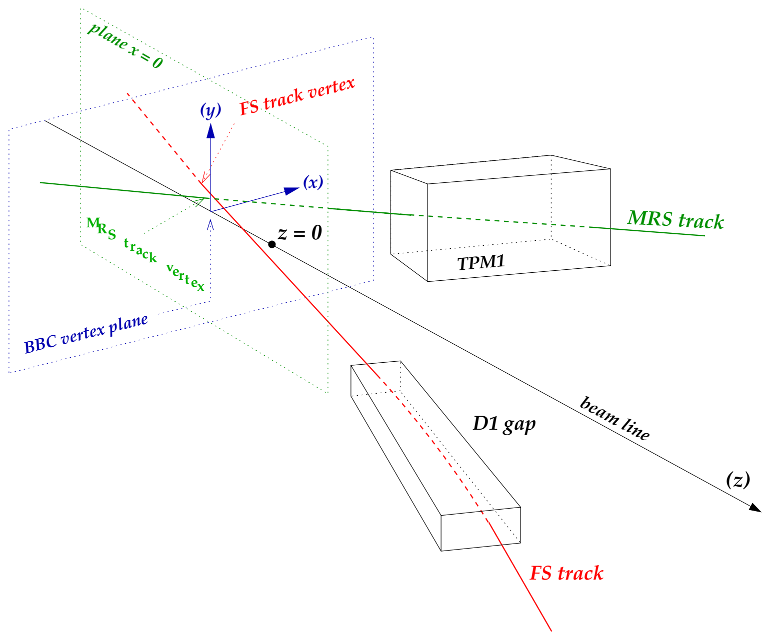

Figure 3.9: *Track projection to primary vertex planes. The intersection point is used as track vertex. The figure is taken from [95].*

For both MRS and FS tracks, the track vertex is compared to the vertex $(0, 0, z_{\rm IP})$ determined by BBCs or INEL counters and the differences in each dimension are fitted with a Gaussian to obtain the means and standard deviations. Finally a 3σ two dimensional elliptical cut[6] is applied on a run-by-run basis in order to minimize the effect of the fluctuations in y. Figure 3.10 illustrates the selection procedure for MRS tracks. It is the same for FS tracks but a cut on x instead of $(z_{\rm trk} - z_{\rm IP})$.

In addition, when the local tracks are matched in a magnet the tracks are required to propagate through the magnet without getting closer than 1 cm to the side of the magnet

[5]The reason to use two different plane is because the resolution along z gets worse as the polar angle of tracks decreases.

[6]That is, for example, $(\frac{x-<x>}{\sigma_x})^2 + (\frac{y-<y>}{\sigma_y})^2 \leq n_\sigma^2$, where n_σ is the number of sigma cut.

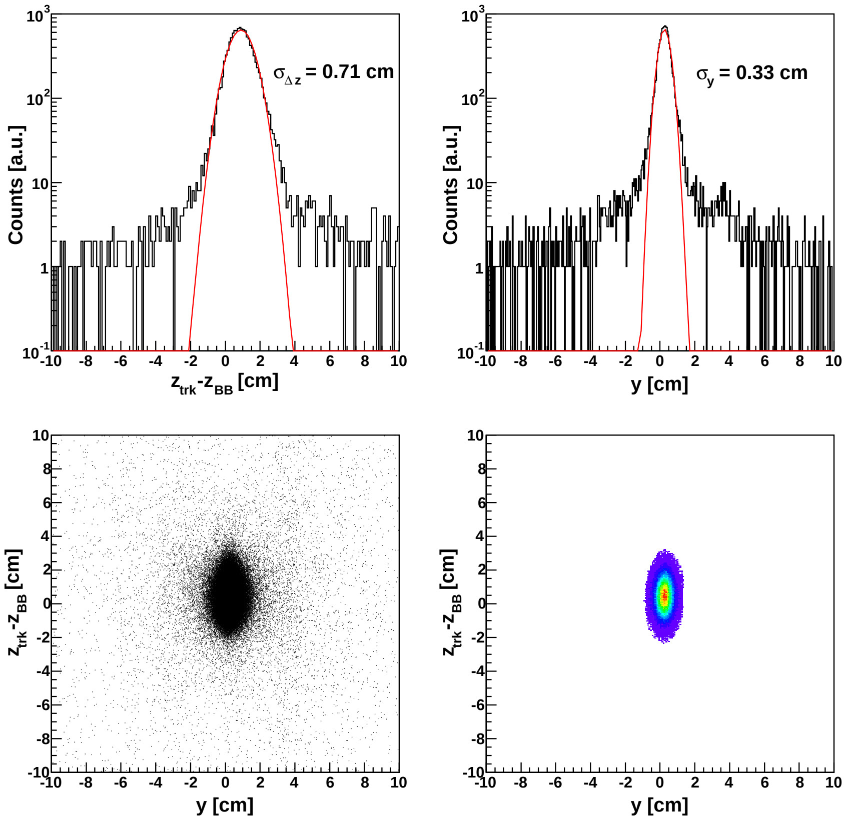

Figure 3.10: *Primary track selection procedure. Top: The differences between track vertex and BB vertex are fitted with a Gaussian. Bottom: The left panel shows the distribution of the difference between track vertex and BB vertex for a setting 90B1000back, where the MRS is positioned at 90 degrees and moved back 50 cm with D5 on B polarity and 1 kGauss magnetic field, in Au+Au collisions. The right panel shows the selected tracks by a 3σ elliptical cut.*

gap. The reason to apply such a magnet fiducial cut is that the confidence in track combination is low due to track direction uncertainties, especially along the y direction because the drift velocity close to the TPC edges is not perfectly uniform [14, 95]. These magnet fiducial cuts have also been taken into account when geometrical acceptance corrections of the spectrometers are calculated.

3.2.2 Particle Identification with TOF Detectors

TOF PID is done by first matching TOF hits to tracks whose momenta are known. Slats intersected by selected tracks are inspected to check if they contain valid TOF hits. Once hits are matched to tracks, the track path lengths[7] can be finally determined and

[7]For Au+Au 2001 run, the track path length is the track trajectory from the collision vertex to the hit position of the TOF wall, while for d+Au and p+p 2003 run, it is the track trajectory from the hit position of the start counter (TD1 or TMrsT0) to the hit position of TOF wall.

hodoscope calibrations can be performed. The TDC calibration leads to the particle time-of-flight. The procedures of the track path length determination, hodoscope calibrations and the time-of-flight determination have been described in detail in [95].

By combining of measurements of the time-of-flight, flight path length and momentum, the charged particle identification is performed by using

$$m^2 = p^2 \left[\left(\frac{t_{\mathrm{TOF}}}{L/c} \right)^2 - 1 \right], \tag{3.13}$$

where p is the momentum, t_{TOF} is the time-of-flight and L is the flight path length. The charged particle identification is then performed using cuts in m^2 and momentum space according to the TOF m^2 resolution.

The TOF m^2 resolution

The PID capability of TOF detectors is strongly dependent on momentum, time and track path length resolutions. In order to qualify the PID resolution, the equation of m^2 as a function of p and β is differentiated with respect to p and β. It then follows from the error propagation that the TOF m^2 resolution σ_{m^2} can be expressed as

$$\left(\frac{\sigma_{m^2}}{m^2} \right)^2 = 4\frac{\sigma_p^2}{p^2} + 4\gamma^4 \frac{\sigma_\beta^2}{\beta^2}, \tag{3.14}$$

where $\gamma = 1/\sqrt{1-\beta^2}$, σ_p and σ_β are the resolution of momentum and β, respectively. The momentum resolution can be parameterized as

$$\frac{\sigma_p^2}{p^2} = p^2\sigma_\alpha^2 + (1 + \frac{m^2}{p^2})\sigma_{\mathrm{ms}}^2, \tag{3.15}$$

where σ_α depends on the angular resolution of tracks and the magnitude of the magnetic field as derived in Eq. 3.5 in the small angular limit. σ_{ms} is a term to take care of the multiple scattering effect. By using $\beta = L/(ct_{\mathrm{TOF}})$, it follows that

$$\frac{\sigma_\beta^2}{\beta^2} = \frac{\sigma_{t_{\mathrm{TOF}}}^2}{t_{\mathrm{TOF}}^2} + \frac{\sigma_L^2}{L^2} \approx \frac{\sigma_{t_{\mathrm{TOF}}}^2}{t_{\mathrm{TOF}}^2}. \tag{3.16}$$

Finally, the m^2 resolution can be expressed as:

$$\sigma_{m^2}^2 = 4 \left[m^4 p^2 \sigma_\alpha^2 + m^4 \left(1 + \frac{m^2}{p^2} \right) \sigma_{\mathrm{ms}}^2 + (m^2 + p^2) p^2 \sigma_t^2 \right], \tag{3.17}$$

where $\sigma_t = c\sigma_{t_{\mathrm{TOF}}}/L$. The m^2 and p are filled in three two-dimensional histograms for intervals of m^2 in $[-0.1, 0.1]$, $[0.15, 0.35]$ and $[0.6, 1.2]$. The m^2 and p distributions for each species are sliced into narrow momentum intervals and fitted with a Gaussian to evaluate the width of m^2. The width σ_{m^2} squared can then be fitted simultaneously for pions, kaons and protons. The parameters of σ_α, σ_{ms} and σ_t are tabulated in Table 3.6 for different MRS settings in Au+Au 2001 runs where the TOFW is used for PID. With

MRS Setting	A350	B350	A700back	B700back	B1000	B1000back
$\sigma_\alpha \times 10^2$ [c/GeV]	3.9	4.0	2.6	2.5	0.87	0.85
$\sigma_{ms} \times 10^2$	2.7	2.4	1.8	2.4	1.4	1.3
$\sigma_t \times 10^3$	6.5	6.2	7.0	6.3	7.0	6.8

Table 3.6: *PID resolution parameters for difference settings where the MRS is at 90 degrees for Au+Au collisions at* $\sqrt{s_{NN}} = 200$ *GeV.*

typical track path length of 435 cm, values for time-of-flight resolution obtained from the fits are 90-110 ps.

In Figure 3.11, a plot of m^2 as calculated from the TOF measurement by the TOFW at 90 degrees versus momentum multiplied by charge is shown together with the applied PID cuts as solid curves. 2σ standard deviation PID cuts in m^2 and momentum space are imposed for each particle species. Protons can be well separated from kaons up to 3.2 GeV/c, while for pions above 2 GeV/c an asymmetric PID cut is applied to reduce the kaon contamination of the pions. As shown in Figure 3.11, the overlap regions which are within the 2σ cuts for both pions and kaons are excluded. The upper cut-off on the pions is $p_T = 3$ GeV/c, where the kaon contamination is estimated to be less than 5%.

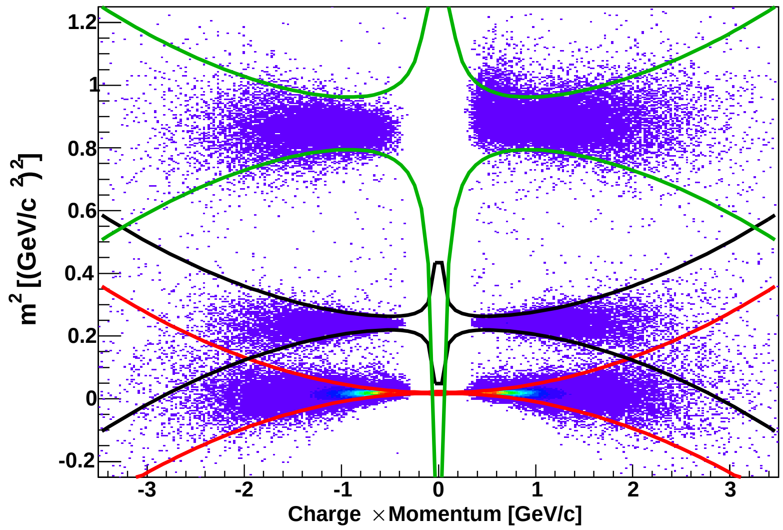

Figure 3.11: m^2 *versus momentum multiplied by charge distribution for the TOFW at 90 degrees in Au+Au collisions at* $\sqrt{s_{NN}} = 200$ *GeV. The curves are the* 2σ *curves used to select pions, kaons and protons.*

In addition, for the MRS lower momentum cut-offs are also applied: 0.4 GeV/c for pions and 0.6 GeV/c for protons and anti-protons. The cut-off value for p and $\bar{p}$ is larger than that for pions due to the large energy loss effect.

For the FS PID in the present Au+Au analysis, only H2 is used for two low magnetic settings, A427 and A843 at 12 degrees. Figure 3.12 illustrates the PID capability of H2 for the data set A427. With 2σ cuts pions and protons are separated from kaons up to 4.2 and 7.1 GeV/c, respectively. Since the momentum threshold is 7.9 GeV/c for kaons to result in a ring in the RICH with gas refractive index of 1.00196, we apply an asymmetric PID cut for proton identification above 7 GeV/c. The overlap regions which are within 2σ cuts for both protons and kaons are excluded. The upper momentum cut-off on the protons is 9 GeV/c where the contamination of protons by kaons is estimated to be less than 6%. In addition, a lower momentum cut-off of 2 GeV/c is also applied for both pion and proton identification due to very low statistics and small geometrical acceptance below the cut-off value.

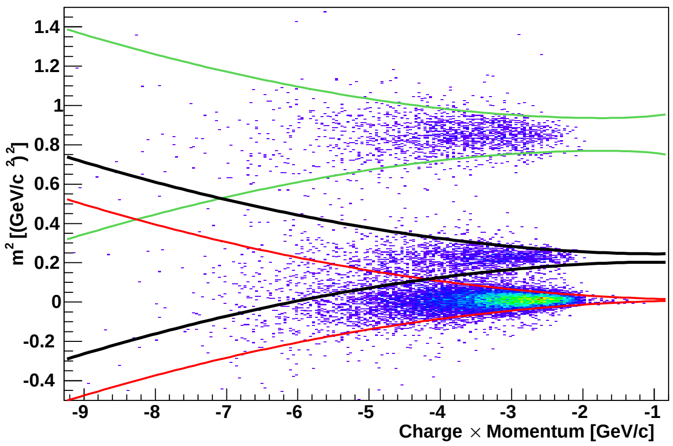

Figure 3.12: m^2 *versus momentum multiplied by charge distribution for H2 at 12 degrees in Au+Au collisions at* $\sqrt{s_{NN}} = 200$ *GeV. The data set is A427.*

By comparing an 1.6σ selection with the 2σ selection it was found that the ratios have little momentum dependence. The ratios for pions and protons were within 2-3% and 2-5% of the 93.3% expected from a Gaussian distribution, respectively. The centrality dependence of the width and the mean position of the m^2 has also been checked for Au+Au collisions. There is no clear difference between central and peripheral collisions.

For d+Au and p+p 2003 runs, the particle flight path length is calculated from the hit position in the spectrometer trigger counter, i.e. TMrsT0 in the MRS or TD1 in the FS, to the hit position in the TOF wall; same for the time-of-flight. Because the timing resolution of the TMrsT0 and TD1 is worse than that of BBCs which are used to determine the start time in Au+Au collisions, the PID capabilities of TOF walls in d+Au and p+p 2003 runs are not as good as those in Au+Au 2001 runs. With the TOFW pions and protons can only be separated from kaons up to 1.6 and 2.6 GeV/c respectively by applying 2σ standard deviation PID cuts. In the present analysis, an asymmetric PID cut is imposed for pion and proton identification above 1.6 and 2.6 GeV/c, respectively. The corresponding upper momentum cut-offs for pions and protons are 2.2 and 3.3 GeV/c. In the FS, in addition to H2, the RICH is used for pion and proton identification.

3.2.3 Particle Identification with the RICH

In the FS, the RICH is used for high momentum charged particle identification by combining the measurement of the ring radius and the momentum.

Index of refraction

Since the momentum threshold for charged particles emitting Čerenkov light and also the radius of the ring depend on the index of refraction of the radiator, it is important to have a well determined and stable refractive index. Unfortunately there was a leakage of gas in the RICH detector which lead to a deviation of the refractive index from the measured value ($n = 1.00203$) when the filling of the radiator was completed.

In order to determine the index of refraction of the radiator during certain runs, pre-identification of pion is done with a guessed index of refraction, e.g. 1.00202 for Au+Au 2001 runs or 1.00170 for d+Au and p+p 2003 runs. By using Eq. 3.12 the index of refraction can be calculated according to

$$n = \frac{\sqrt{(r/L)^2 + 1}}{\beta}, \tag{3.18}$$

where $\beta = p/\sqrt{m^2 + p^2}$. Figure 3.13 shows the refractive index determined in such a way for data set A843 at 12 degrees for Au+Au and p+p collisions at $\sqrt{s_{NN}} = 200$ GeV, respectively. The index of refraction for different data sets is tabulated in Table 3.7. In d+Au collisions, the indices of refraction are 1.00187(1.00186) from run number 8375 to 8389 and 1.00173 from run number 8547 to 8632. The difference is significant for different run periods.

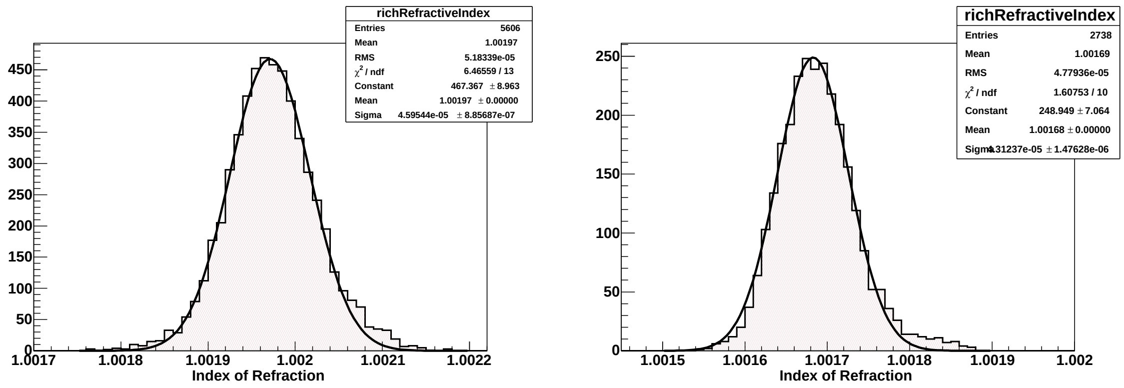

Figure 3.13: *Index of refraction for the RICH radiator calculated from pre-identified pions. Left: data set A843 at 12 degrees in Au+Au collisions at* $\sqrt{s_{NN}} = 200$ *GeV. Right: data set A843 at 12 degrees in p+p collisions at* $\sqrt{s_{NN}} = 200$ *GeV.*

The RICH PID resolution

The RICH PID is performed by using the combination of two measurements, the ring radius from the RICH and the momentum, together with the determined refractive index

FS Setting	A427	A843	A1692	A2268
Au+Au	1.00195	1.00197	1.00192	1.00192
d+Au	-	1.00187/1.00173	1.00186/1.00173	-
p+p	1.00169	1.00168	1.00168	-

Table 3.7: *Index of refraction of the RICH radiator for different settings with FS at 12 degrees in Au+Au, d+Au and p+p collisions. In d+Au collisions, the indices of refraction are 1.00187(1.00186) from run number 8375 to 8389 and 1.00173 from run number 8547 to 8632.*

of the RICH radiator. The square of the mass is calculated according to the following formula,

$$m^2 = p^2 \left[\frac{n^2}{(\frac{r}{L})^2 + 1} - 1 \right], \tag{3.19}$$

where L is the mirror focal length and r is the ring radius. Similar to the TOF PID, the charged particle identification by RICH is performed using a cut in the m^2 and momentum space.

The PID cut is based on a parameterization of the measured m^2 width as a function of momentum,

$$\begin{aligned}\sigma^2_{m^2} \quad = \quad & 4m^4p^2\sigma^2_\alpha + 4m^4\left(1 + \frac{m^2}{p^2}\right)\sigma^2_{\mathrm{ms}} \\ & +4(p^2+m^2)^2\sigma^2_n + \frac{4(p^2+m^2)^3(n^2p^2-p^2-m^2)}{n^4p^4L^2}\sigma^2_r \\ & +\frac{8m^2(p^2+m^2)}{pn}\mathrm{cov(p,n)} \\ & -\frac{8(p^2+m^2)^{5/2}(n^2p^2-p^2-m^2)^{1/2}}{n^3p^2L}\mathrm{cov(r,n)}, \end{aligned} \tag{3.20}$$

where σ_α depends on the track angular resolution and field setting, σ_{ms} takes into account multiple scattering effect, σ_n is the relative uncertainty of the refractive index and σ_r is the radius resolution, $\mathrm{cov(p,n)}$ and $\mathrm{cov(r,n)}$ are the covariances of p and n and of r and n, respectively. These covariant terms rise because the index of refraction is extracted from the same data set, otherwise they should be zero. The RICH PID capability is therefore strongly dependent on the momentum resolution, the uncertainty of the refractive index and the uncertainty of the radius measurements.

In Figure 3.14, a plot of m^2 versus momentum is shown together with applied 3σ standard deviation PID cuts as solid curves. The typical value for σ_r is 0.45 cm, which is consistent with the value estimated in the BRAHMS Conceptual Design Report [97]. By comparing a 2σ cut selection with the 3σ selection, the ratios show no momentum dependence and are within 1-3% of the 95.5% expected from a Gaussian distribution. Also shown in the figure is the threshold curve which is defined by Eq. 3.19 with $r = 0$ and given as

$$m^2 = p^2(n^2 - 1). \tag{3.21}$$

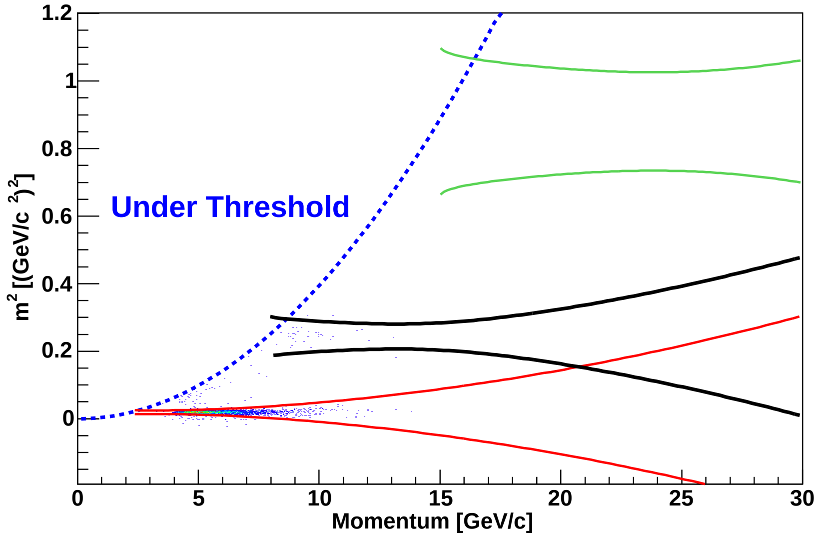

Figure 3.14: *Mass squared versus momentum distribution for data set A843 at 12 degrees in Au+Au collisions at* $\sqrt{s_{NN}}$ = 200 *GeV. The lines indicate the RICH 3σ standard deviation PID cuts, from bottom to top, for pions, kaons and protons.*

In addition protons are also identified indirectly, that is, particles with momenta larger than the kaon momentum threshold and zero ring radii are identified as protons. The lower momentum cut-off for proton identification is 9 GeV/c, which is 1 GeV/c away from the kaon threshold and the inefficiency for pion and kaon identification is expected to be less than 3%. Figure 3.15 shows the ring radius versus momentum distribution measured by the RICH before and after the PID cuts applied.

3.2.4 Corrections

In order to get correct particle spectra, corrections for (1) the geometrical acceptance, (2) in-flight decays for pions and kaons, (3) the effect of multiple scattering, (4) nuclear interactions with materials in the detector (including anti-proton absorption), and (5) detection inefficiency of detectors have to be applied. Most of these corrections are evaluated by using BRAG, a GEANT [98] based Monte Carlo simulation program of the BRAHMS detector. The single charged particle tracks are passed to GEANT and propagated through the detector elements. The output, which contains information on the position and momentum of the particles and their hits in the active detectors, is then digitized[8] and passed through the event reconstruction software which is used for the real data.

[8]Digitization is user-defined information simulating the response of a given detector element.

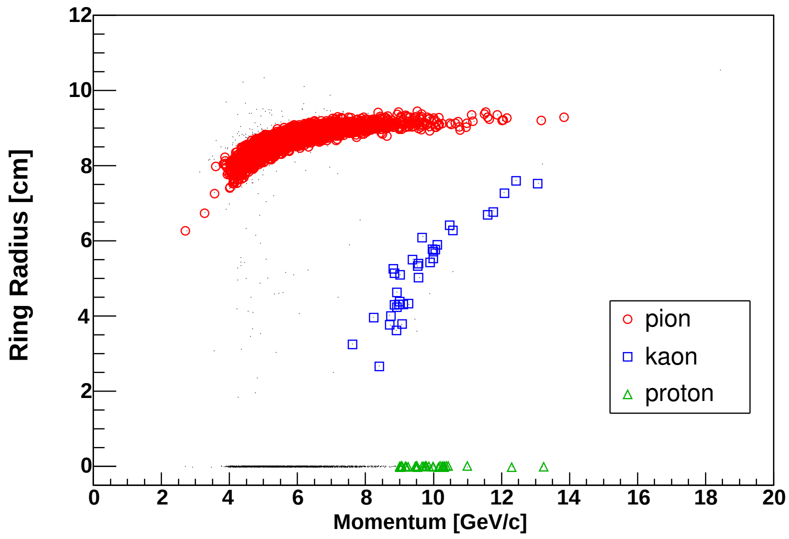

Figure 3.15: *RICH ring radius versus momentum distribution before and after PID cuts applied. The scatter-plot shows all tracks associated with a RICH ring. Fully identified particles are shown in open circle (pion), rectangle (kaon) and triangle (proton), respectively. The data set used is the same as in Figure 3.14.*

Geometrical acceptance

The acceptance is purely geometrical and is calculated by simulation. A flat distribution in momentum p, θ and ϕ, of single particles is generated in a solid angle subtended by the magnetic gap from a certain vertex bin[9]. In the simulation, these particles are propagated through the detectors to see if they can successfully be reconstructed by certain detectors depending on which PID detector is used in the real data analysis. The acceptance is then determined in each (y, p_T) or (η, p_T) bin by dividing the reconstructed output by the generated input as expressed as follows:

$$\epsilon_{\rm acc}(y, p_T) = \frac{\text{Number of reconstructed tracks}}{\text{Number of generated tracks}} \times \frac{\Delta\phi}{2\pi}, \tag{3.22}$$

where y and η denote rapidity and pseudo-rapidity, respectively. The $\Delta\phi/2\pi$ reflects that particles are only generated in an angle interval $\Delta\phi$ which covers completely the vertical aperture of the first magnet in the spectrometer. The resulting correction factors $1/\epsilon_{\rm acc}$ are then applied to the data in each (y, p_T) or (η, p_T) bin and for each individual species[10]. The procedure to generate the acceptance map is well described in [14]. An example of acceptance for π^- and $\bar{p}$ is shown in Figure 3.16 for MRS setting B1000 at 90 degrees and FS settings at 12 degrees. The color contours represent the acceptance magnitudes. In all setting used in present analysis, the relative statistical error introduced by acceptance correction is at most $\sim 4\%$ when the edges of the acceptance excluded.

[9]The vertex ranges are ± 20 cm for FS and ± 15 for MRS and are divided into bins of 5 cm.

[10]In (η, p_T) space acceptances are the same for all species, but in (y, p_T) space they are different because rapidity y depends on mass.

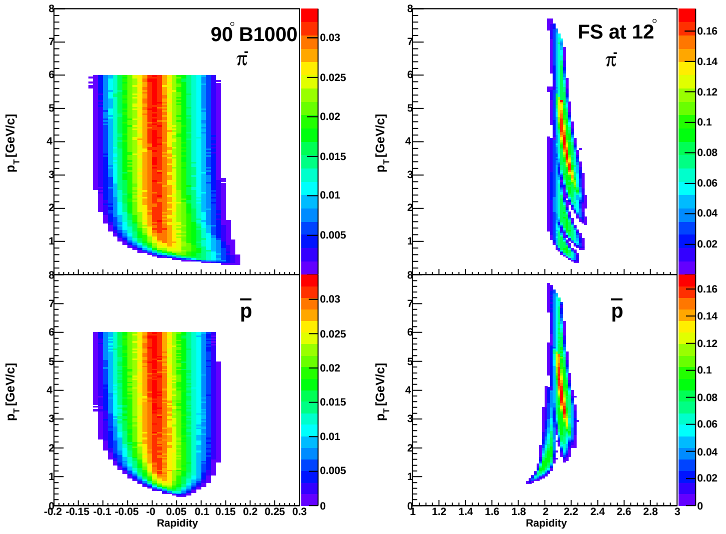

Figure 3.16: *π^- and $\bar{p}$ acceptances in (p_T, y) of the MRS setting 90° B1000 (left) and the FS settings at 12° (right).*

Tracking efficiency

The tracking efficiency of TPCs has been studied by embedding simulated tracks into real events [99]. Alternatively a reference track method [100] has been developed to study the tracking efficiencies of the tracking chambers in the forward spectrometer.

1. Track Embedding. The simulated tracks with well defined momentum and identity are digitized and merged into a real event at the raw data level. The raw data with embedded track are then passed through the same track reconstruction procedure including cluster finder, cluster deconvolution and track finder [14] as for real events. The tracking efficiency $\epsilon_{\rm tr}$ is then determined as a function of the number of hits in the TPCs for the event as

$$\epsilon_{\rm tr} = \frac{\text{Number of reconstructed embedded tracks}}{\text{Number of embedded tracks}}. \tag{3.23}$$

   As shown in Figure 3.17, the efficiency curves turn out to be linear and the efficiency decreases as the number of hits increase. When the corrections are applied in this manner there is no momentum dependence. The momentum dependence was studied in [99] and it turns out that the dependence observed is related to multiple scattering which will be separately corrected for. These efficiency curves are used for different centrality classes since the number of total TPC hits is related to the event centrality.

2. Reference Track Method. In such an approach the efficiency of a given tracking device is studied by comparing the number of matched track segments in the tracking detector under study to the number of reference tracks reconstructed by other

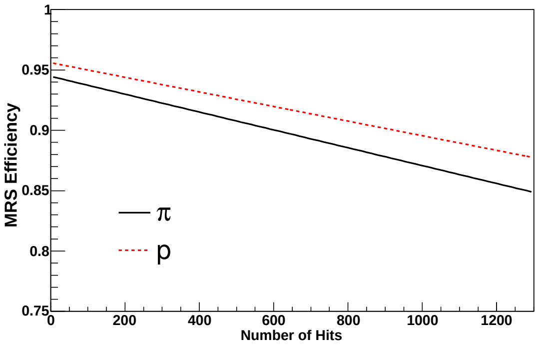

Figure 3.17: *MRS global tracking efficiency estimated by the tracking embedding method for pions and protons as a function of total hits in TPM1 and TPM2. The figure is re-produced from [99].*

tracking detectors except the one under study. The tracking efficiency for the given detector is then defined as

$$\epsilon_{\mathrm{tr}} = \frac{\text{Number of well matched track segments}}{\text{Number of reference tracks}}. \qquad (3.24)$$

The reference track is constructed by matching track segments in x and y the same way as track matching for momentum determination. Once the reference track is made, it is extrapolated to the mid-plane of the tracking detector under study. If the deviation in positions at the mid-plane of the tracking detector and slopes between the extrapolate track and the track segment is within certain matching cuts e.g. 3σ, the track segment is then to be identified as well matched. This procedure has been applied for each data set and studied as a function of centrality for Au+Au collisions and horizontal track position in the mid-plane and slope. To apply the tracking efficiency correction, the dependence on momentum has been studied and no clear momentum dependence is found. Table 3.8 lists the FS tracking efficiencies for different data sets used in the present analysis when FS sits at 12 degrees. For d+Au collisions, within the tracking efficiency uncertainty there is no centrality dependence. By this procedure the particle type dependence has not yet been investigated.

For the present analysis, the track embedding efficiencies are used for MRS data, while the efficiencies obtained from the reference track method are used for FS data.

PID efficiency

For PID detectors corrections for the detection inefficiency and for the PID cuts have to be applied. For the RICH detector we applied 3σ PID cuts which corresponds to 99.7% of the particle yields, while for time-of-flight "walls" 2σ standard PID deviation cuts are applied and above the K/π and p/π separation momenta the cuts are applied asymmetrically.

System	A427	A843	A1692	A2268
0 – 10%	0.614±0.006	0.614±0.010	0.638±0.034	0.755±0.035
10 – 20%	0.653±0.006	0.655±0.011	0.684±0.042	0.784±0.035
20 – 40%	0.698±0.008	0.777±0.011	0.764±0.046	0.824±0.044
40 – 60%	0.673±0.011	0.785±0.015	0.855±0.064	–
d+Au	–	0.803±0.006	0.808±0.027	–
p+p	0.845±0.005	0.818±0.008	0.818±0.015	–

Table 3.8: *FS tracking efficiencies for p+p, d+Au and centrality selected Au+Au collisions with the FS at 12 degrees for setting A427, A843, A1692 and A2268.*

Figure 3.18 shows the inverse PID cut corrections applied to each identified pion by TOFW for MRS setting 90° B1000 in Au+Au collisions.

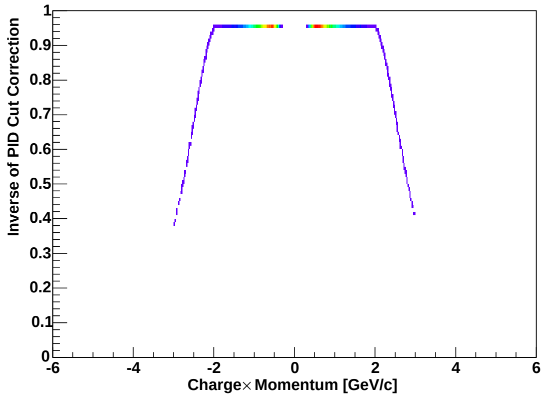

Figure 3.18: *Inverse of PID cut corrections applied to each identified pion by TOFW for MRS setting 90° B1000 in Au+Au collisions.*

The detection efficiency of time-of-flight “walls” has been investigated by dividing the distribution of hits associated to valid tracks by the distribution of the number of times valid tracks intersect the slats by extrapolation. The slats in the TOFW show a constant efficiency of $\sim 93 \pm 2\%$ when bad slats are excluded, and H2 achieves a constant efficiency of $\sim 98 \pm 1\%$ [14, 95]. In addition to the slat efficiency there is also a correction for hits that are ignored because multiple tracks are pointing to the same slat. This effect depends on the track density and was found negligible for the TOFW and H2 [14].

The RICH detection efficiency has been studied via simulation by using BRAG. The simulated charged pion tracks (with only energy loss switched on) are passed to BRAG. Digitized simulation data are merged with raw background events and then passed through the event reconstruction and particle identification procedure. In this simulation the response of the RICH detector is tuned to match the real data. The refractive index of the RICH radiator and the PID cuts used are the same as for real data. Figure 3.19 shows the RICH PID efficiency for setting 12° A427. Above 3 GeV/c, the RICH PID efficiency is $\sim 97\%$. Also shown in the figure is the RICH detection efficiency estimated by using identified pions, which is limited to the momentum range common to H2. Since pions might decay after H2, such a procedure underestimates the RICH detection efficiency but provides a lower limit. In [14], the RICH inefficiency has been studied by using H2 to study the difference $1/\beta - 1/\beta_{\mathrm{proton}}$, where $1/\beta$ is measured by H2 and $1/\beta_{\mathrm{proton}}$ is the theoretical value for proton with a certain momentum. It is found that the RICH inefficiency is $\sim 3\%$ for all settings which is consistent with the PID efficiency estimated by simulation.

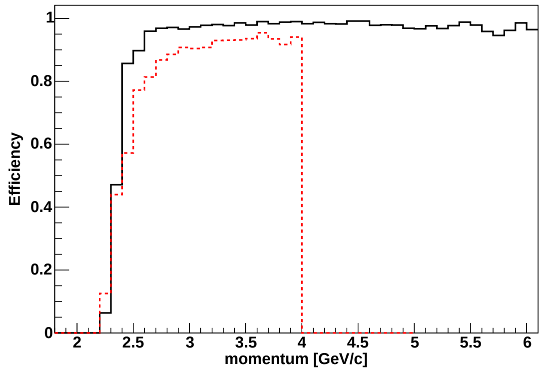

Figure 3.19: *RICH detection efficiency estimated by simulation (black solid line) and by using pions identified in H2 (red dashed line).*

Since the RICH detection efficiency solely depends on β it is assumed in this analysis that the RICH efficiency is 97% above a momentum 2.8 GeV/c for pions and 10 GeV/c for kaons. For protons identified by the indirect method the contamination of protons from pions and kaons is then estimated by multiplying the total pion and kaon yields in each momentum bin by the RICH inefficiency, i.e. 3%. Table 3.9 lists the average contamination factors for protons in the momentum range of 10-18 GeV/c by pions and kaons due to the RICH inefficiency when the FS sits at 12 degrees. For Au+Au collisions, the centrality dependence is not clear because the error is rather large due to lacking of statistics. In this analysis, a contamination factor of 5% is assumed for all centralities and the uncertainty thus goes to systematic errors. However, the contaminations are significant for d+Au and p+p collisions because the anti-proton yield is lower than that in Au+Au collisions.

Au+Au 0-10%	Au+Au 10-20%	Au+Au 20-40%	Au+Au 40-60%	d+Au	p+p
6.5±3.4%	4.6±3.2%	5.0±4.4%	3.5±6.4%	22.4±6.7%	36.8±2.2%

Table 3.9: *Contamination factors for protons in the momentum range of 10-18 GeV/c by pions and kaons due to the RICH inefficiency when the FS sits at 12 degrees.*

Corrections for decay, multiple scattering and absorption

Corrections for pion decay in-flight, multiple scattering and (anti-)proton absorption were studied by using BRAG. Single particles are passed from BRAG with and without the studied physical process to the BRAHMS event reconstruction chain which includes digitization of hits in the detectors, track reconstruction and particle identification. The same fiducial cuts, matching cuts and PID cuts should be applied as for real data. Finally the corrections were obtained by dividing the two simulation results in each momentum bin for each species as

$$\epsilon_{\rm sec}(j,p)^{-1} = \frac{\text{Number of reconstructed particles with process on}}{\text{Number of reconstructed particles with process off}}, \tag{3.25}$$

where j is the particle species. The resulting corrections are then fitted with a function of $a - b\exp(-cp)$. Figure 3.20 shows the momentum dependence of the corrections for different spectrometers. Due to additional trigger counters used in p+p and d+Au 2003 runs, additional corrections as shown in the lower panels have to be applied for multiple scattering and nuclear interactions.

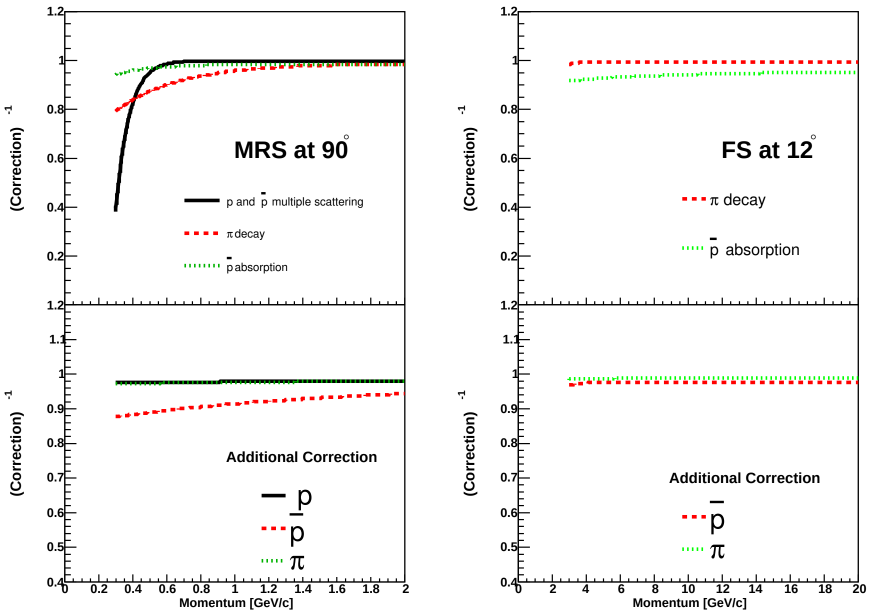

Figure 3.20: *Top panels illustrate corrections applied for MRS data at 90 degrees (left) and FS data at 12 degrees (right), respectively. Bottom panels are additional corrections for MRS (left) and FS (right) applied to p+p and d+Au data due to the additional trigger counters used.*

3.2.5 Building Particle Spectra

In order to remove the vertex dependence, each data set is divided into vertex bins of 5 cm with the same vertex range as the acceptance maps. For each vertex bin v the correction and raw data are constructed in the form of two-dimensional histograms in p_T and rapidity y (or pseudo-rapidity η) with the same binning as the acceptance maps. To obtain the differential multiplicity, a histogram containing all sorts of corrections and normalizations is constructed as

$$\epsilon_v(p_T, y) = \frac{\epsilon_{\rm sec}}{2\pi N_{\rm evt}\delta p_T \delta y \epsilon_{\rm acc}\epsilon_{\rm tr}\epsilon_{\rm pid}}, \tag{3.26}$$

where subscript v denotes the vertex bin and $N_{\rm evt}$ the corresponding number of events, δp_T and δy are the bin sizes in p_T and y, respectively. $\epsilon_{\rm acc}$, $\epsilon_{\rm tr}$, $\epsilon_{\rm sec}$ and $\epsilon_{\rm pid}$ denote the geometrical acceptance, tracking efficiency, secondary interaction correction and PID efficiency. It is worthwhile to mention that $N_{\rm evt}$ for Au+Au analysis is the number of trigger 5 or trigger 6 events depending on the event selection but for p+p and d+Au analyses it is the number of trigger 5 (minimum-bias trigger) events (in a certain centrality bin) multiplied by the scale-down factor when trigger 2 or trigger 3 is scaled up properly[11]. Then, for each data set s characterized by a spectrometer angle and a magnetic field, raw data histograms for all vertex bins are added up directly while the correction histograms are summed up according to following equation

$$\epsilon_{\rm s}(p_T, y) = \frac{1}{\sum_v (\epsilon_v(p_T, y))^{-1}}. \tag{3.27}$$

The normalized and corrected differential yields $dN_s(p_T, y)$ can thus be built up by

$$dN_s(p_T, y) = N_s(p_T, y) \times \epsilon_{\rm s}(p_T, y), \tag{3.28}$$

where $N_s(p_T, y)$ is the number of particles in cell (p_T, y) from a certain data set s.

In order to cover a broader p_T range at a certain rapidity range, it is necessary to combine data from several data sets. A weighted average of the differential yields from different data sets is taken according to

$$< dN(p_T, y) >= \frac{\sum_s dN_s(p_T, y) \times W_s(p_T, y)}{\sum_s W_s(p_T, y)}, \tag{3.29}$$

where the weight $W_s(p_T, y)$ is defined as [14]

$$W_s(p_T, y) = \frac{1}{\epsilon_s(p_T, y)}, \tag{3.30}$$

so that entries with larger corrections carry lower weights. Thus 3.29 can be rewritten as

$$< dN(p_T, y) >= \left(\sum_s N_s(p_T, y)\right) \times \left(\sum_s \frac{1}{\epsilon_s(p_T, y)}\right)^{-1}. \tag{3.31}$$

The left panel of Figure 3.21 shows the normalized differential yields of π^+ for 0-10% central Au+Au collusions at $\sqrt{s_{NN}} = 200$ GeV after averaging over several settings. Once the averaged two-dimensional histogram for differential yields is known, projections can be

[11] In certain runs, trigger 2 or trigger 3 has been scaled down, therefore the number of FS tracks or MRS tracks has to be scaled up accordingly.

made in a narrow rapidity interval of width Δy (as shown in Figure 3.21 interval between the two lines), and the invariant spectra at a given rapidity range can be constructed according to the following equations:

$$N(p_T) = \left(\sum_y \sum_s N_s(p_T, y)\right) \times \left(\sum_y \sum_s \frac{1}{\epsilon_s(p_T, y)}\right)^{-1}, \tag{3.32}$$

$$\frac{1}{2\pi p_T} \frac{d^2N}{dp_T dy} = \frac{N(p_T)}{p_T}, \tag{3.33}$$

where the sum of rapidity is from $y - \Delta y/2$ to $y + \Delta y/2$ and p_T in the denominator of last equation is the center of the histogram bin[12]. It is worthwhile to mention that $\epsilon_s(p_T, y)$ is zero outside of the geometrical acceptance of the setting and thus those bins are ignored for both the data and the correction. The right panel of Figure 3.21 shows the invariant spectrum obtained for π^+ at mid-rapidity in 0-10% central Au+Au collisions at $\sqrt{s} = 200$ GeV.

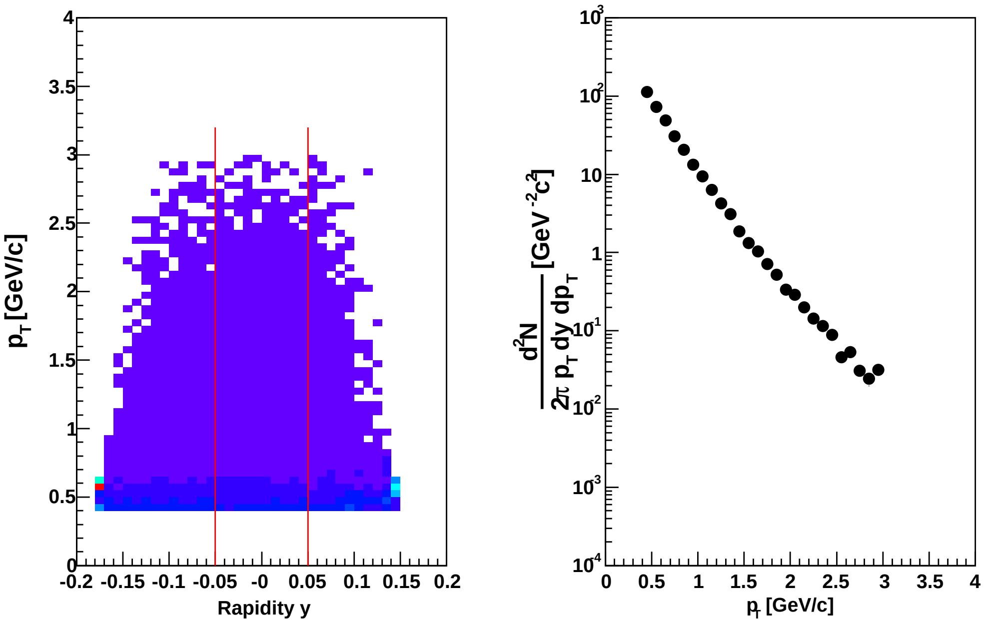

Figure 3.21: *Left: Normalized π^+ differential yields at mid-rapidity after several data sets were corrected and combined. Right: Invariant yields of π^+ at mid-rapidity in 0-10% central Au+Au collisions at $\sqrt{s_{NN}} = 200$ GeV.*

[12] To be more accurate, the p_T value should be the weighted average of p_T in each bin. Then this average should also be used when plotting the spectra. The effect on the absolute particle yields would be large, but should be minor on relative yields as presented in this thesis.

3.2.6 Systematic Uncertainties

The systematic errors in determining the particle spectra come from the uncertainties in track matching and momentum determination, uncertainties in the time-of-flight measurements and ring radius reconstruction procedure, and uncertainties in the quality of the tracking efficiency and PID efficiency estimations.

Because particle spectra are often obtained by the combination of several data sets covering the same phase space, sets of p_T spectra were made by using different data sets and varying the cuts applied in the data analysis. By studying the variation of the constructed spectra, the systematic errors are estimated. They are shown separately for different colliding systems in the next chapter. The centrality dependence of the systematic errors has not been investigated.

Chapter 4

Results and Discussion

In this chapter the high p_T results from the BRAHMS experiment will be presented and compared to other experiments and models.

4.1 High p_T Spectra of Protons and Charged Pions

4.1.1 Au+Au

Figure 4.1 shows the invariant p_T spectra of π^+ (left) and π^- (right) at mid-rapidity for various centrality classes of Au+Au collisions at $\sqrt{s_{NN}} = 200$ GeV. For clarity, the data points are scaled vertically as quoted in the figure. The error bars are statistical errors only. Systematic errors are estimated to be 13% for $p_T < 2$ GeV/c and 15% for $p_T > 2$ GeV/c. The pion spectra show an approximate power-law shape for all centrality bins.

Figure 4.2 shows the invariant p_T spectra of protons (left) and anti-protons (right) at the same energy. The error bars are statistical only. Systematic errors are estimated to be 14%. Feed-down corrections for Λ ($\bar{\Lambda}$) have not yet been applied. Both p and $\bar{p}$ spectra show a centrality dependence below 1.5 GeV/c, i.e. with increasing collision centrality a shoulder at low p_T develops.

Figure 4.3 shows the p_T distributions for charged pions and (anti-)protons at mid-rapidity for the most central 0-10% Au+Au collisions. The spectra for positively charged particles are presented on the left panel and those for negatively charged particles on the right panel. The data show a clear mass dependence in the shape of the spectra. The p and $\bar{p}$ spectra have a convex shape, while the pion spectra have a concave shape. The inverse slopes increase with the mass of the particles indicating a radial flow is developing during the evolution of a heavy ion collision. Another notable observation is that at p_T above $\sim$ 2 GeV/c, the proton and anti-proton yields become comparable to the pion yields, which is also observed in 130 GeV Au+Au collisions [101].

To illustrate the difference between using pseudo-rapidity η and using rapidity y, Figure 4.4 shows the invariant p_T spectra of charged pions and (anti-)protons at $\eta = 0$ for the most central 0-10% Au+Au collisions. Compared to Figure 4.3, the Jacobian transformation effect is rather large in particular at the low p_T region. From Eq. B.14 in Appendix B, one can see that the Jacobian effect is the largest at the most central rapidity region for the heaviest particle at lowest p_T. The effect becomes smaller at

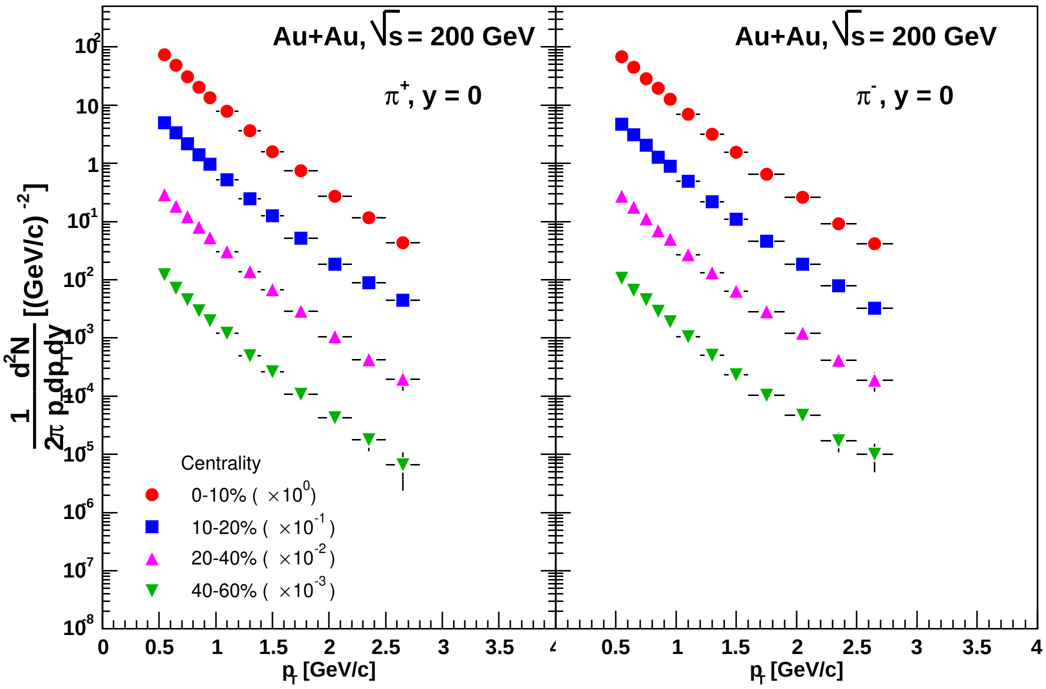

Figure 4.1: *The invariant p_T spectra of π^+ (left) and π^- (right) at mid-rapidity in Au+Au collisions at $\sqrt{s_{NN}} = 200$ GeV. The different symbols correspond to different centrality bins. The error bars are statistical errors only. Systematic errors are estimated to be 13% at $p_T < 2$ GeV/c and 15% at $p_T > 2$ GeV/c. For clarity, the data points are scaled vertically as quoted.*

forward rapidity and high p_T. At rapidity $y = 2.2$, the effect is less than 4% for protons at $p_T > 1$ GeV/c.

The invariant p_T spectra for negatively charged pions and anti-protons at pseudo-rapidity $\eta = 2.2$ are shown in Figure 4.5 for four different centralities. The error bars are statistical only. Systematic errors are estimated to be 14% and 15% respectively for π^- and $\bar{p}$.

Compared to our published spectra for inclusive charged hadrons in 0-10% central Au+Au collisions, Figure 4.6 shows that the presented results are consistently around 10% higher at mid-rapidity. On the contrary, at $\eta = 2.2$ the presented data lie around 16% below the previously published results [102]. One should note, however, that BRAHMS' published results are based on data recorded by the FFS only, while the present analysis is done with data recorded by the full forward spectrometer.

4.1.2 d+Au and p+p

Present analyses on p+p and d+Au data are mainly focused on the pseudo-rapidity $\eta = 2.2$, which is not covered by other experiments at RHIC. At mid-rapidity, the PID capability of the TOFW gets worse when the TMrsT0 is used to determine the start time

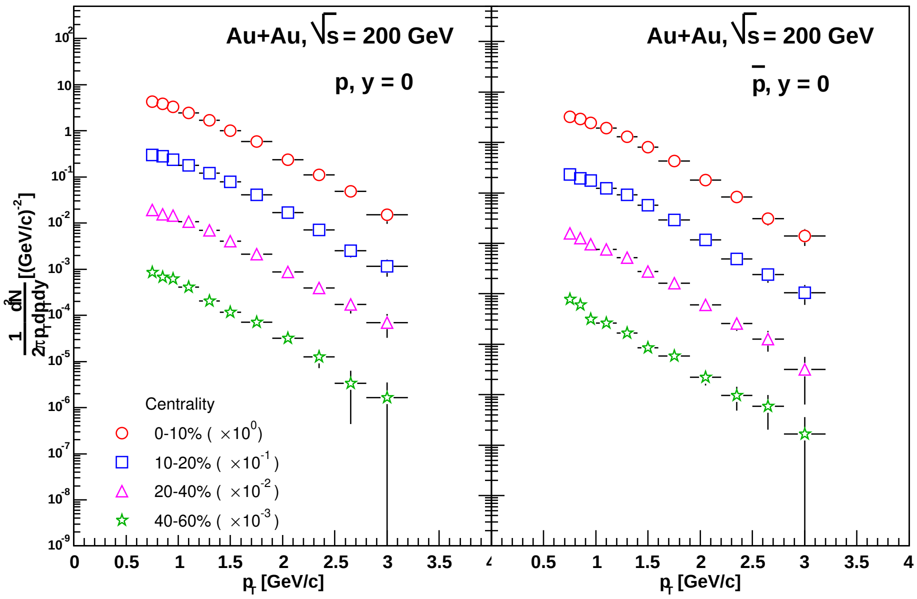

Figure 4.2: *The invariant p_T spectra of p (left) and $\bar{p}$ (right) at mid-rapidity in Au+Au collisions at $\sqrt{s_{NN}} = 200$ GeV. The different symbols correspond to different centrality bins. The error bars are statistical only. Systematic errors are estimated to be 14%. Feed-down corrections for $\Lambda(\bar{\Lambda})$ decaying into $p(\bar{p})$ have not been applied. For clarity, the data points are scaled vertically as quoted.*

and other PID detectors such as TFW2 and C4 are still not well under control. However, it is possible to separate protons from kaons up to 2.3 GeV/c with a 2σ cut. Figure 4.7 shows the invariant p_T spectra of protons and anti-protons at mid-rapidity in minimum-bias p+p collisions at $\sqrt{s} = 200$ GeV. The error bars are statistical only. Systematic errors are estimated to be 15%. Also shown in the figure is an exponential function fitted to the spectra,

$$\frac{d^2N}{2\pi p_T dp_T dy} = \frac{1}{2\pi} \frac{Y}{T^2} \exp(-p_T/T). \tag{4.1}$$

For protons the rapidity density $Y = 0.1309 \pm 0.0039$ and the inverse slope parameter $T = 0.298 \pm 0.004$ GeV, while for anti-protons $Y = 0.1236 \pm 0.0041$ and $T = 0.283 \pm 0.004$ GeV.

For the FS sitting at 12 degrees there are three data sets for p+p collisions: A427, A843 and A1692, while for d+Au collisions there are only two data sets (A843 and A1692) available. As a consequence, only protons with momentum above 10 GeV/c can be identified. We will therefore not present anti-proton spectra for d+Au collisions.

The left panel of Figure 4.8 shows the p_T spectra of π^- at pseudo-rapidity $\eta = 2.2$ in d+Au collisions for different centralities. The right panel of Figure 4.8 shows the p_T spectra of π^- and $\bar{p}$ at pseudo-rapidity $\eta = 2.2$ together with the fit function for minimum-bias p+p collisions (right) at $\sqrt{s} = 200$ GeV. The error bars are statistical only. Systematic errors are estimated to be 13% for π^- in both d+Au and $p+p$ collisions

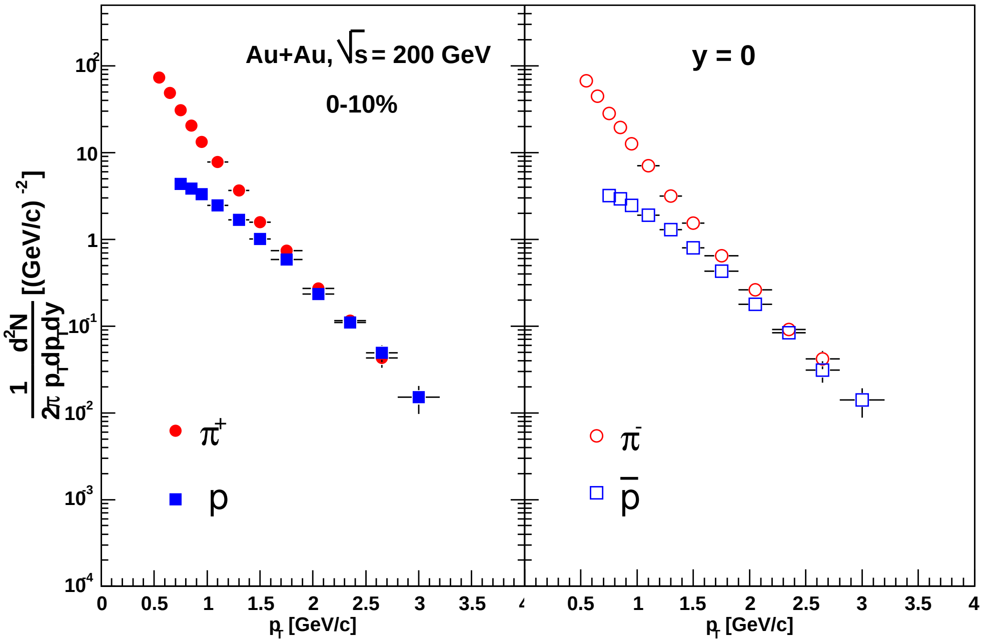

Figure 4.3: *p_T distributions for charged pions and (anti-)protons at mid-rapidity in 0-10% central Au+Au collisions at $\sqrt{s_{NN}} = 200$ GeV. Positively and negatively charged particles are shown on the left and right panels, respectively.*

and 15% (17%) for $\bar{p}$ in $p+p$ collisions at $p_T < 1.2$ GeV/c ($p_T > 1.8$ GeV/c). The spectra of negatively charged pions are parameterized by a power-law function,

$$\frac{d^2N}{2\pi p_T dp_T d\eta} = A(1 + \frac{p_T}{p_0})^{-n}, \tag{4.2}$$

with $A = 12.95 \pm 2.43$ GeV$^{-2}c^2$, $p_0 = 0.9956 \pm 0.117$ GeV/c and $n = 9.447 \pm 0.52$. As discussed before, the PID capability of H2 in p+p and d+Au runs is not as good as that in Au+Au runs. This results in a gap in the anti-proton spectrum from 1.2 to 1.8 GeV/c, where anti-protons can't be identified. The data can be fitted by an exponential function in p_T with a rapidity density $Y = 0.0755 \pm 0.0048$ and an inverse slope parameter $T = 0.2314 \pm 0.0071$ GeV.

For comparison with the published reference spectra of inclusive charged hadrons in [102], which were constructed based on the UA1 measurement after applying appropriate correction for the difference in η coverage estimated using HIJING simulation, Figure 4.9 shows the spectra of charged hadrons at mid-rapidity and negatively charged hadrons at $\eta = 2.2$ in $p+p$ collisions at $\sqrt{s} = 200$ GeV after experimental trigger bias correction[1]. Within systematic uncertainties, the measured spectra are consistent with the constructed one.

[1]Our minimum-bias trigger selects non-single-diffractive events. The correction to trigger bias was estimated to be $13 \pm 5\%$ [108], approximately independent of η and p_T.

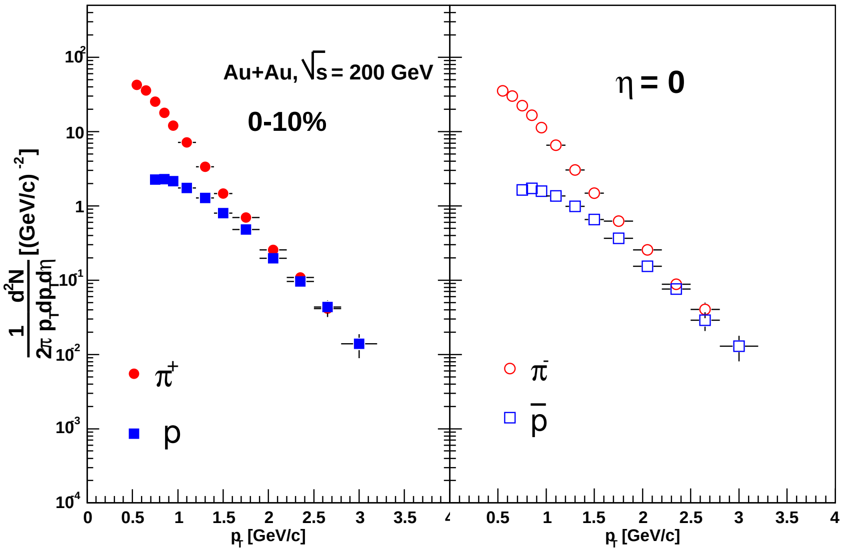

Figure 4.4: *p_T distributions for charged pions and (anti-)protons at $\eta = 0$ in 0-10% central Au+Au collisions at $\sqrt{s_{NN}} = 200$ GeV. Positively and negatively charged particles are shown on the left and right panels, respectively.*

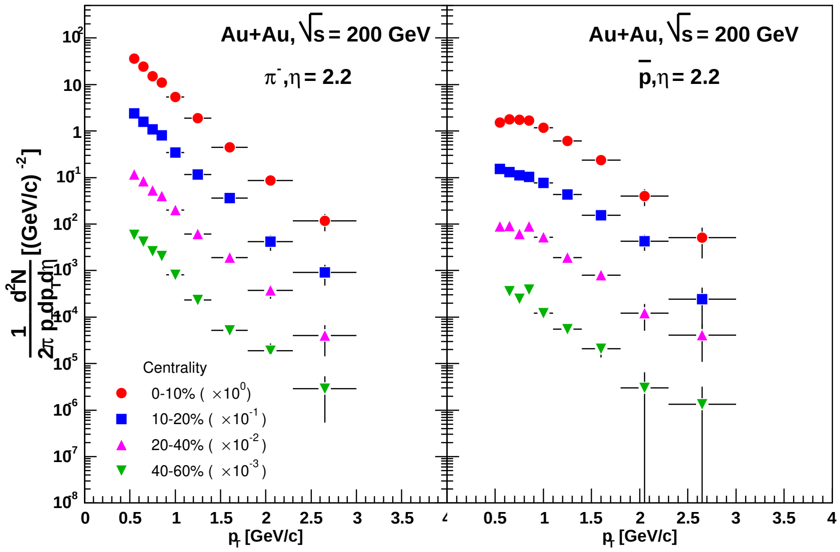

Figure 4.5: *p_T distributions for negatively charged pions and anti-protons at pseudo-rapidity $\eta = 2.2$ in Au+Au collisions at $\sqrt{s_{NN}} = 200$ GeV. The different symbols correspond to different centrality bins. The error bars are statistical only. Systematic errors are estimated to be 14% and 15% respectively for π^- and $\bar{p}$. Feed-down correction for $\bar{\Lambda}$ decaying into $\bar{p}$ has not been applied. For clarity, the data points are scaled vertically as quoted.*

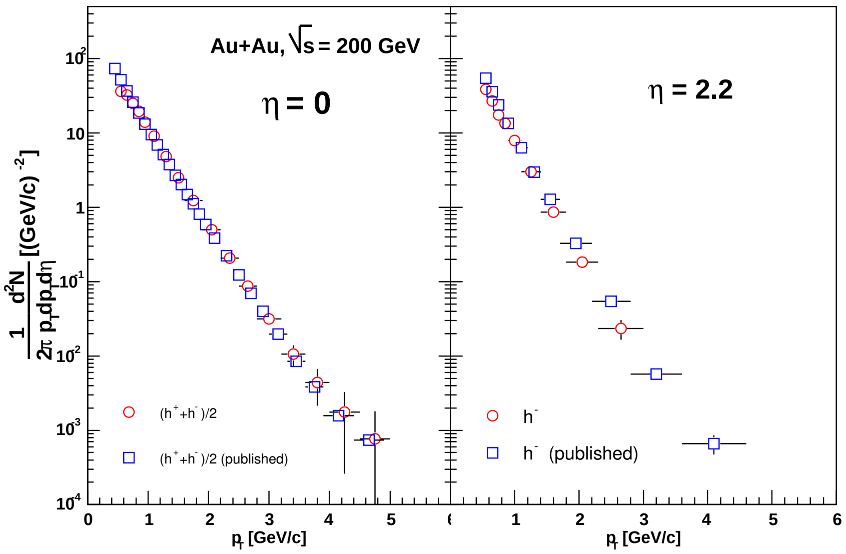

Figure 4.6: *A comparison of p_T distributions for inclusive charged hadrons in 0-10% central Au+Au collisions at $\sqrt{s_{NN}} = 200$ GeV with the published data [102].*

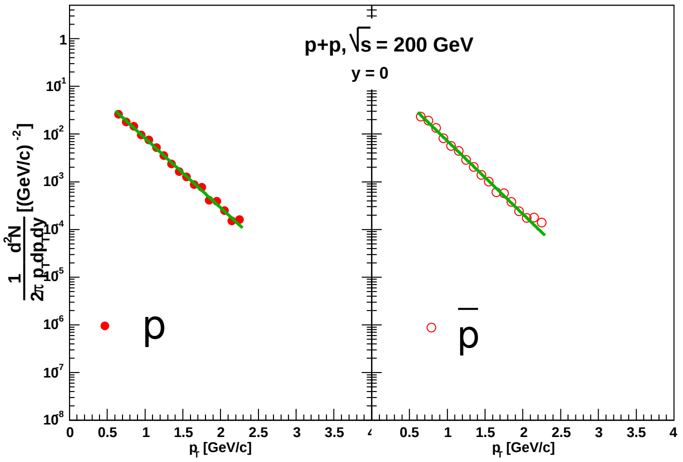

Figure 4.7: *p_T distributions for protons (left) and anti-protons (right) at mid-rapidity in minimum-bias p+p collisions at $\sqrt{s} = 200$ GeV. The error bars are statistical only. Systematic errors are estimated to be 15%. Feed-down corrections for $\Lambda(\bar{\Lambda})$ decaying into $p(\bar{p})$ have not been applied.*

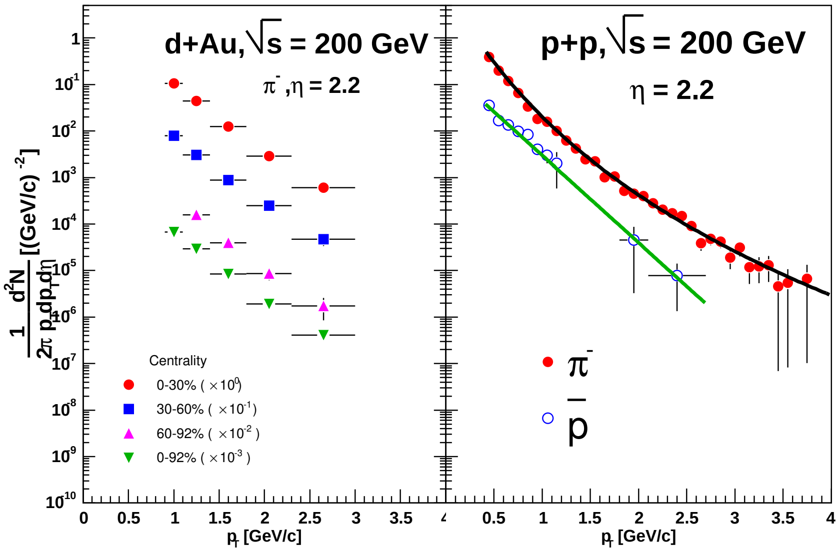

Figure 4.8: *Left: p_T distributions for negatively charged pions at $\eta = 2.2$ in d+Au collisions at $\sqrt{s_{NN}} = 200$ GeV. The different symbols correspond to different centrality bins. For clarity, the data points are scaled vertically as quoted. Right: p_T distributions for negatively charged pions and anti-protons at $\eta = 2.2$ in p+p collisions at $\sqrt{s} = 200$ GeV. The error bars are statistical only. Systematic errors are estimated to be 13% for π^- in both d+Au and p+p collisions and 15% (17%) for $\bar{p}$ in p+p collisions at $p_T < 1.2$ GeV/c ($p_T > 1.8$ GeV/c). A feed-down correction for $\bar{\Lambda}$ decaying into $\bar{p}$ has not been applied.*

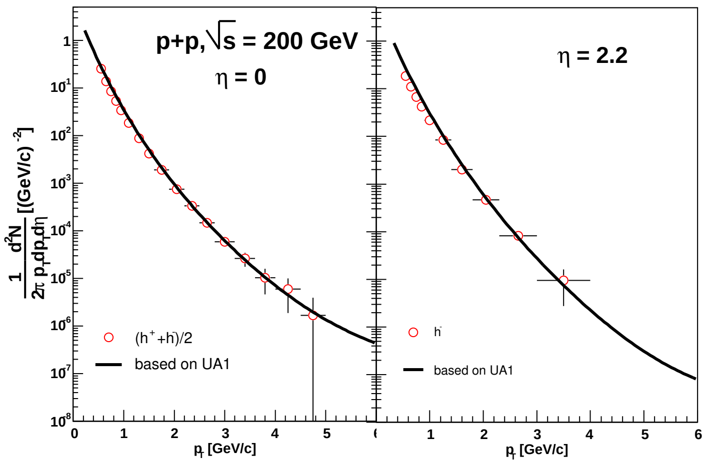

Figure 4.9: *The spectra of inclusive charged hadrons at mid-rapidity and negatively charged hadrons at $\eta = 2.2$ in $p + p$ collisions. The solid lines are the published reference spectra [102] constructed based on UA1 data.*

4.2 Nuclear Modification Factors

The nuclear medium can affect the high p_T hadron yields. It is common to quantify nuclear medium effects by the "nuclear modification factor" R_{AB} as defined in Eq. 2.36. One of the most interesting observation by all four RHIC experiments is that high p_T inclusive hadron yields in central Au+Au collisions are suppressed as compared to elementary nucleon-nucleon collisions. In this section, such an observation by the BRAHMS experiment will be reviewed, and then measurements of nuclear modification factors for charged pions and (anti-) protons will be presented at both mid-rapidity and pseudo-rapidity $\eta = 2.2$.

4.2.1 R_{AuAu} for Inclusive Charged Hadrons

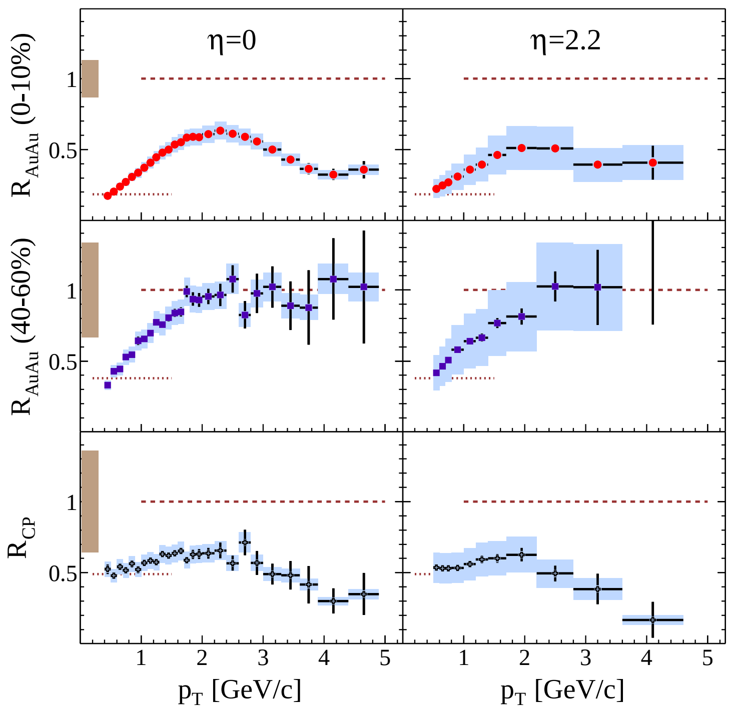

Figure 4.10: *Top row: Nuclear modification factor R_{AuAu} of inclusive charged hadrons as a function of p_T at $\eta = 0$ and $\eta = 2.2$ for 0-10% most central Au+Au collisions at $\sqrt{s_{NN}} = 200$ GeV. Middle row: as top row, but for centralities 40-60%. Bottom row: ratio of R_{AuAu} for the most central and semi-peripheral collisions at the two rapidities. The dotted and dashed lines show the expected value of R_{AuAu} using a scaling by the number of participants and by the number of binary collisions, respectively. Error bars indicate statistical errors. Systematic errors are denoted by the grey bands. The grey band at $p_T = 0$ is the uncertainty on the scale. The figure is taken from [102].*

Figure 4.10 shows the nuclear modification factors R_{AuAu} as a function of p_T at $\eta = 0$ and $\eta = 2.2$ for different centrality Au+Au collisions. The reference spectra used in the calculations were constructed from the UA1 measurement of the $p+\bar{p}$ collisions at CERN, suitably corrected for the respective η coverage [102]. The low p_T part of the spectrum which is associated with soft interactions scales with the number of participants. Above $p_T \approx 2$ GeV/c the R_{AuAu} distributions for central Au+Au collisions decrease and are systematically lower than unity. In other words, the high p_T component of the inclusive charged hadron yields in central Au+Au collisions is suppressed as compared to $p+p$ and peripheral Au+Au collisions at both mid-rapidity and forward rapidity. The degree of the high p_T suppression at $\eta = 2.2$ is similar to or even larger than that at $\eta = 0$.

In addition, it has also been observed that the yield of neutral pions is more strongly suppressed than that for non-identified charged hadrons in central Au+Au collisions at RHIC [103]. A study of the species dependence of the suppression would thus shed light on the hadron production mechanisms in heavy ion collisions at RHIC energy.

4.2.2 R_{dAu} for Inclusive Charged Hadrons

Figure 4.11 shows the nuclear modification factor of inclusive charged hadrons at four difference pseudo-rapidities measured for minimum bias d+Au collisions at $\sqrt{s_{NN}} = 200$ GeV [108]. In the calculation, the reference spectra are measured by BRAHMS for $p+p$ collisions at $\sqrt{s} = 200$ GeV. At mid-rapidity, R_{dAu} shows an enhancement as compared to the binary scaling limit at $p_T > 2$ GeV/c. In contrast to central Au+Au collisions, no suppression but an enhancement above $p_T \approx 2$ GeV/c at mid-rapidity in d+Au collisions is seen and is interpreted as an evidence for a final-state suppression of high p_T hadrons in central Au+Au collisions. At mid-rapidity, observations for such a high p_T suppression in central Au+Au collisions and the absence of high p_T suppression in $d+Au$ collisions have also been reported by the other three experiments [103, 104, 105]. However, the R_{dAu} does not show a Cronin-like peak at $\eta = 1$ and at more forward rapidity ($\eta = 3.2$) the data show a suppression of the high p_T hadron yields.

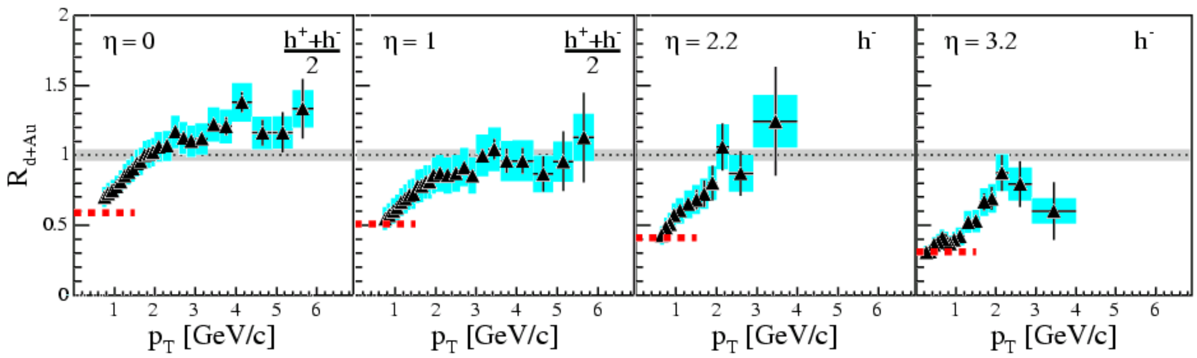

Figure 4.11: *Nuclear modification factor for charged hadrons at pseudo-rapidities $\eta = 0, 1.0, 2.2, 3.2$. The error bars indicate statistical errors. Systematic errors are shown by shaded boxes. The shaded band around unity indicates the estimated error on the normalization to $\langle N_{coll} \rangle$. Dashed lines at $p_T < 1$ GeV/c show the normalized charged particle density ratio $\frac{1}{\langle N_{coll} \rangle} \frac{dN/d\eta(d+Au)}{dN/d\eta(p+p)}$. The figure is taken from [108].*

4.2.3 R_{AA} for Charged Pions and (Anti-)Protons

Reference spectrum

In order to calculate the nuclear modification factor for identified charged pions and (anti-)protons, we need a reference spectrum for nucleon-nucleon collisions. The reference spectra of (anti-)protons at mid-rapidity and negatively charged pions and protons at pseudo-rapidity $\eta = 2.2$ are presented in the last section. Due to the limitation of the PID capability of our own spectrometer at mid-rapidity for charged pions, the reference spectrum of charged pions is constructed via PYTHIA simulation based on the measurement of the π^0 spectrum by PHENIX [40] in $p+p$ collisions at $\sqrt{s} = 200$ GeV.

The PHENIX π^0 spectrum for p+p collisions at $\sqrt{s} = 200$ GeV is shown in Figure 4.12a together with a power-law fit (Eq. 4.2) to the data with parameters $A = 9.147$ GeV$^{-2}c^2$, $p_0 = 1.219$ GeV$/c$ and $n = 9.99$. Figure 4.12b shows the ratio of the data to the power-law fit with the systematic error band.

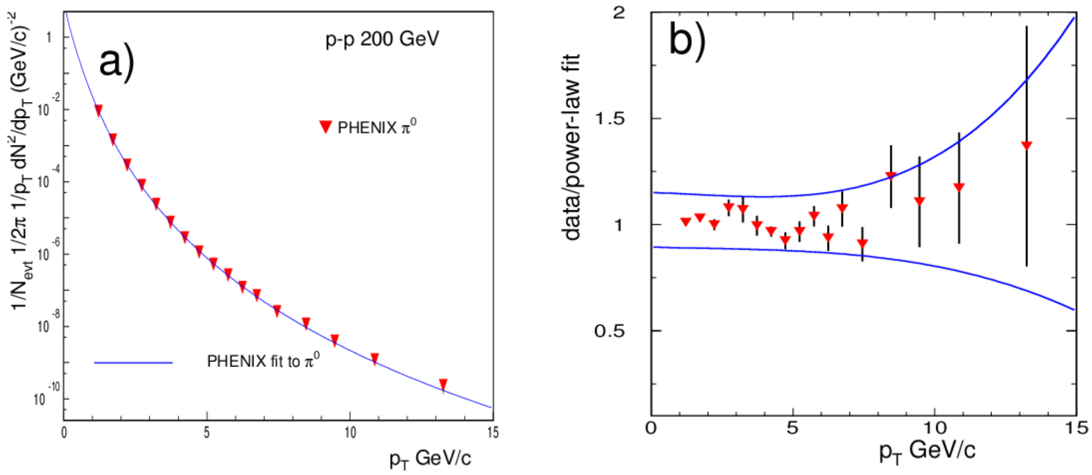

Figure 4.12: *a) PHENIX π^0 spectrum from p+p collisions at $\sqrt{s} = 200 GeV$ together with a power-law fit. b) Ratio of the data to the fit together with the systematic error band. The figure is taken from [107].*

The rapidity coverage of PHENIX neutral pion measurements is from -0.35 to 0.35 and is different from our charged pion measurements. Furthermore there might be a small isospin effect on charged and neutral pion spectra at mid-rapidity. PYTHIA, a leading order pQCD model optimized to $p+p$ collisions, is used to investigate the rapidity dependence of the p_T spectrum and the isospin effect. Figure 4.13 shows p_T spectra of pions from PYTHIA and ratios of them for $\sqrt{s} = 200$ GeV p+p collisions. In order to minimize the isospin effect on nuclear modification factor, we will construct the p_T spectra of $(\pi^+ + \pi^-)/2$ for $p+p$ collisions as the reference spectrum of charged pions.

The left panel of Figure 4.14 shows the spectra from PYTHIA for π^0 in the rapidity range of -0.35 to 0.35 and $(\pi^+ + \pi^-)/2$ in the rapidity range from -0.05 to 0.05 together with the PHENIX fit function to its π^0 data. The reference spectrum for $(\pi^+ + \pi^-)/2$ is

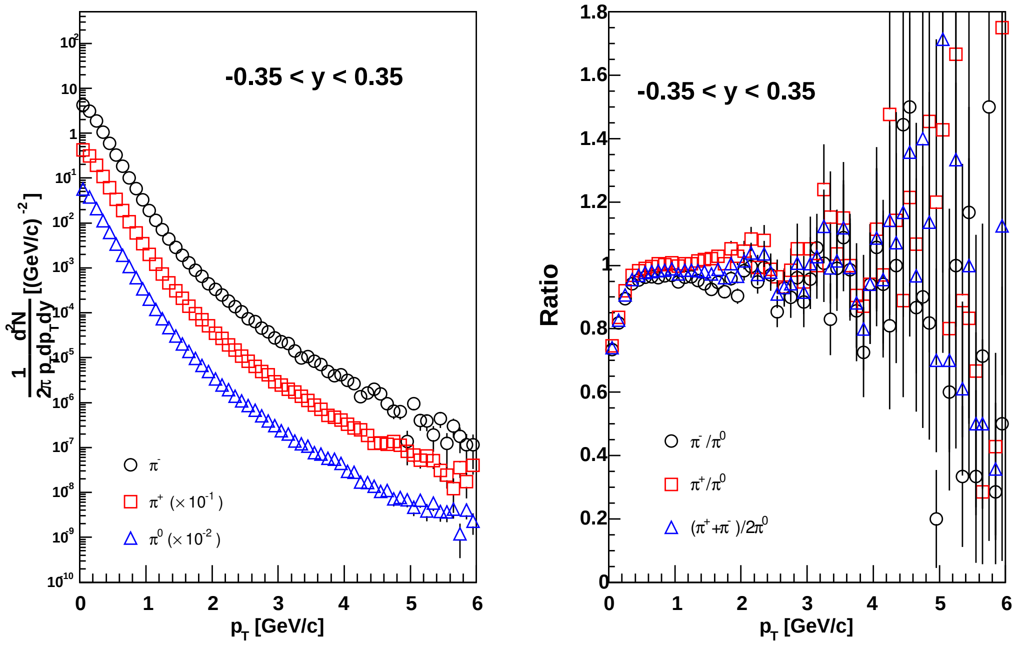

Figure 4.13: *Left: p_T spectra of pions from a PYTHIA simulation for 200 GeV p+p collisions. Right: π^+/π^0, π^-/π^0 and $(\pi^+ + \pi^-)/2\pi^0$ ratios illustrate the isospin effect.*

constructed by dividing the neutral pion spectrum from PHENIX by the spectrum from PYTHIA at the same rapidity range and then multiplying the results by the $(\pi^+ + \pi^-)/2$ spectrum from PYTHIA. The resulting spectrum together with a power-law fit is shown in the right panel of Figure 4.14. The fit parameters as in Eq. 4.2 are $A = 8.665$ GeV$^{-2}c^2$, $p_0 = 1.257$ GeV/c and $n = 10.16$. The systematic errors introduced by PYTHIA are estimated by varying the K factor and/or the intrinsic k_T of hadrons to be less than 12% for the overall p_T range covered by our Au+Au data. Since the systematic error of the PHENIX neutral pion spectrum is less than 15% at $p_T < 10$ GeV/c, the total systematic error of the constructed spectrum is thus estimated to be less than 19%.

R_{AuAu} for charged pions and protons at mid-rapidity

Figure 4.15 shows the nuclear modification factor R_{AuAu} as a function of p_T for $\pi^{\pm}$ and $p(\bar{p})$ at mid-rapidity for 0-10% central Au+Au collisions at $\sqrt{s_{NN}} = 200$ GeV. The dotted and dashed lines in the figure indicate the expectations of participant scaling and binary scaling, respectively. The shaded bars represent the systematic errors associated with the determination of these quantities. The experimental error bars indicate statistical errors only. Systematic errors other than the uncertainties in $\langle N_{coll} \rangle$ determinations are estimated to be 24% for charged pions and 22% for (anti-)protons[2]. Similar to the non-

[2]This includes the uncertainties in the minimum-bias trigger efficiency.

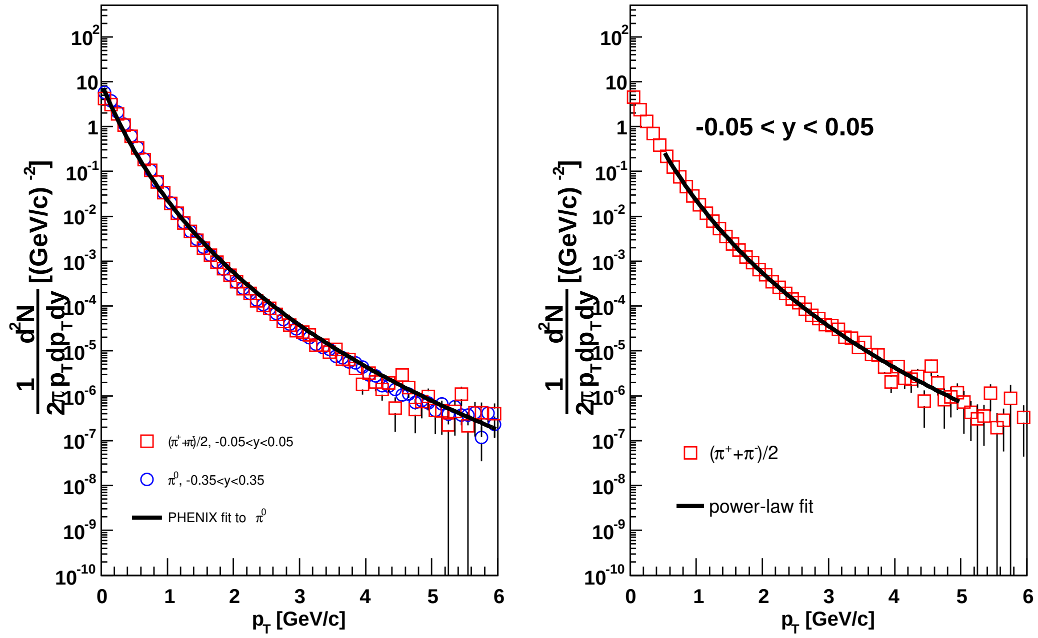

Figure 4.14: *Left: p_T spectra of pions at two different rapidity ranges from PYTHIA simulation for 200 GeV p+p collisions together with the PHENIX fit function to its π^0 measurements. Right: Constructed reference spectrum for charged pions at the rapidity range of -0.05 to 0.05.*

identified charged hadrons, R_{AuAu} for charged pions increases monotonically up to 1.5 GeV/c and remains below unity above 1.5 GeV/c indicating that charged pion yields are suppressed with respect to elementary p+p collisions at high p_T. However, the data show that (anti-)proton reaches unity for $p_T \geq 1.5$ GeV/c, consistent with binary scaling. These observations suggest that a significant fraction of the particle yield at high p_T is attributed to protons and anti-protons and indicate some high p_T production mechanisms other than fragmentation of partons with large momentum transfer in central Au+Au collisions at RHIC energy.

In Figure 4.16, R_{AuAu} for charged pions as a function of p_T is shown for semi-peripheral (with centrality of 40-60%) Au+Au collisions at $\sqrt{s_{NN}} = 200$ GeV. In contrast to central Au+Au collisions, R_{AuAu} remains near unity above $p_T \sim 1.5$ GeV/c for semi-peripheral collisions.

R_{AuAu} for π^- and $\bar{p}$ at $\eta = 2.2$

Figure 4.17 shows R_{AuAu} as a function of p_T for π^- and $\bar{p}$ at pseudo-rapidity $\eta = 2.2$ for 0-10% central Au+Au collisions at $\sqrt{s_{NN}} = 200$ GeV. The dotted and dashed lines in the figure indicate the expectations of participant scaling and binary scaling, respectively. The

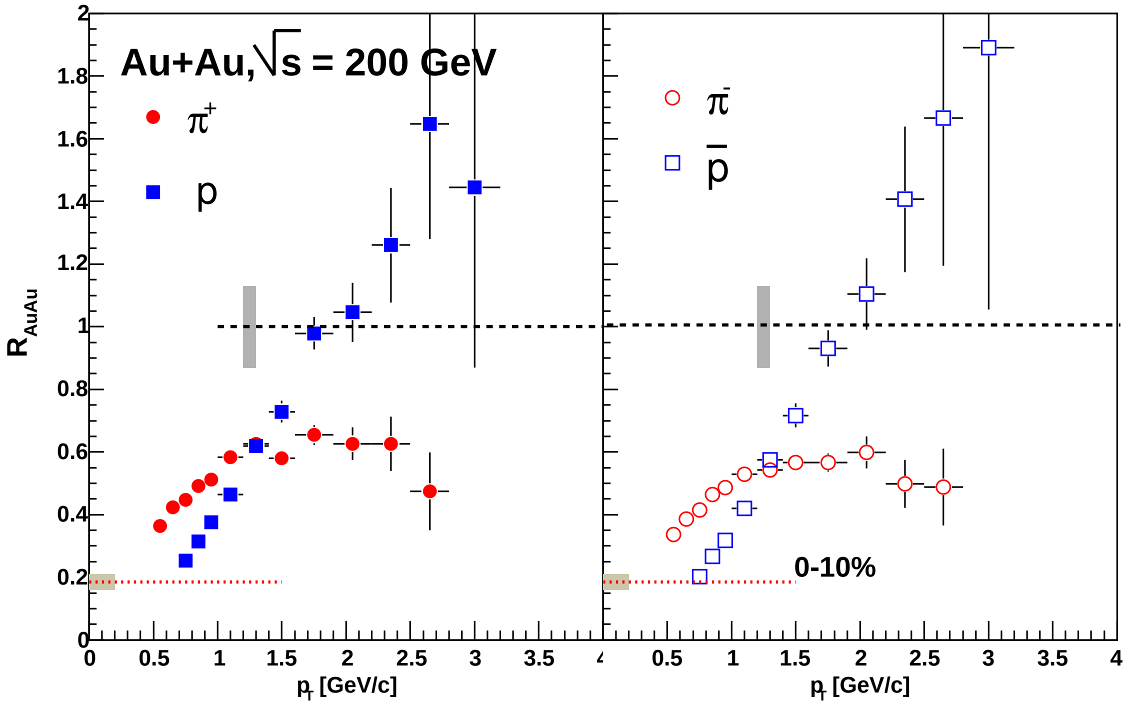

Figure 4.15: *R_{AuAu} for charged pions and (anti-)protons at mid-rapidity for 0-10% central Au+Au collisions at $\sqrt{s_{NN}}$ = 200 GeV. The dotted and dashed lines indicate the expectations of participant scaling and binary scaling, respectively. The shaded bars represent the systematic errors associated with the determination of these quantities. The experimental error bars indicate statistical errors only. Systematic errors other than the uncertainties in $\langle N_{coll} \rangle$ determinations are estimated to be 24% for charged pions and 22% for (anti-)protons.*

shaded bars represent the systematic errors associated with the determination of these quantities. The experimental error bars indicate statistical errors only. Systematic errors other than the uncertainties in $\langle N_{coll} \rangle$ determinations are estimated to be 20% for π^- and 23% for anti-protons[3]. The high p_T π^- yields at forward rapidity show even stronger suppression than that at mid-rapidity. Unfortunately the large and model dependent systematic errors for the reference spectrum of charged pions at mid-rapidity limit us to draw a definite conclusion. Another interesting observation is that anti-proton yields at forward rapidity are also not suppressed at $p_T > 1.5$ GeV/c with respect to elementary p+p collisions.

[3]It includes also the systematic error introduced by fitting.

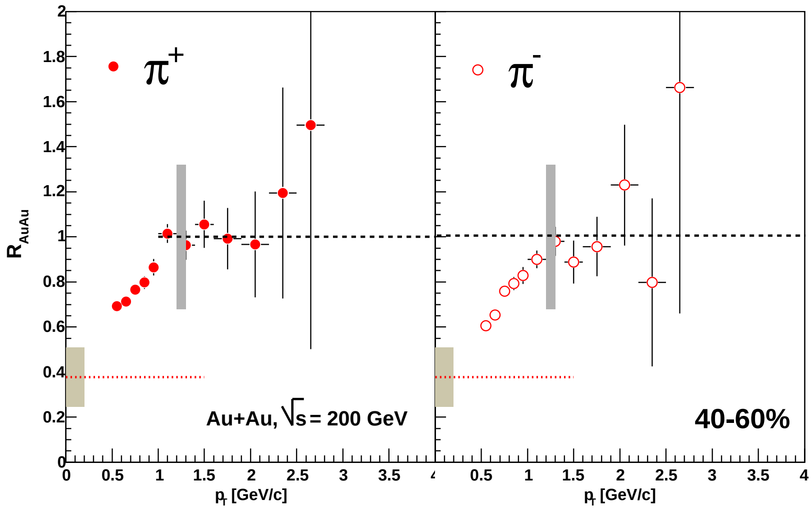

Figure 4.16: *R_{AuAu} for $\pi^{\pm}$ at mid-rapidity for semi-peripheral (with centrality of 40-60%) Au+Au collisions at* $\sqrt{s_{NN}} = 200$ *GeV. The dotted and dashed lines indicate the expectations of participant scaling and binary scaling, respectively. The shaded bars represent the systematic errors associated with the determination of these quantities. The experimental error bars indicate statistical errors only. Systematic errors other than the uncertainties in $\langle N_{coll} \rangle$ determinations are estimated to be 24%.*

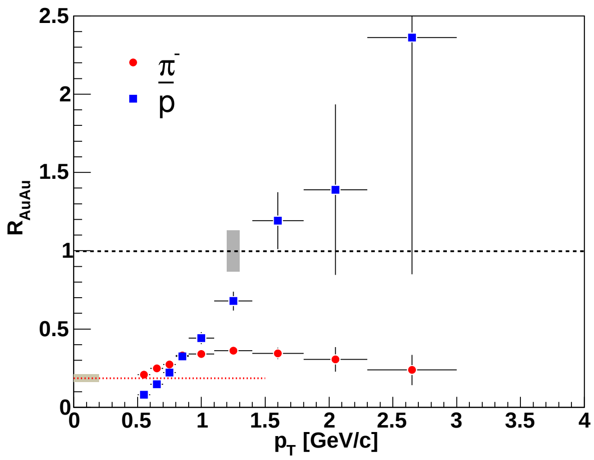

Figure 4.17: *R_{AuAu} for negatively charged pions and anti-protons at pseudo-rapidity* $\eta = 2.2$ *for 0-10% central Au+Au collisions at* $\sqrt{s_{NN}} = 200$ *GeV. The dotted and dashed lines in the figure indicate the expectations of participant scaling and binary scaling, respectively. The shaded bars represent the systematic errors associated with the determination of these quantities. The experimental error bars indicate statistical errors only. Systematic errors other than the uncertainties in $\langle N_{coll} \rangle$ determinations are estimated to be 20% for π^-'s and 23% for anti-protons.*

R_{dAu} for π^- at forward rapidity

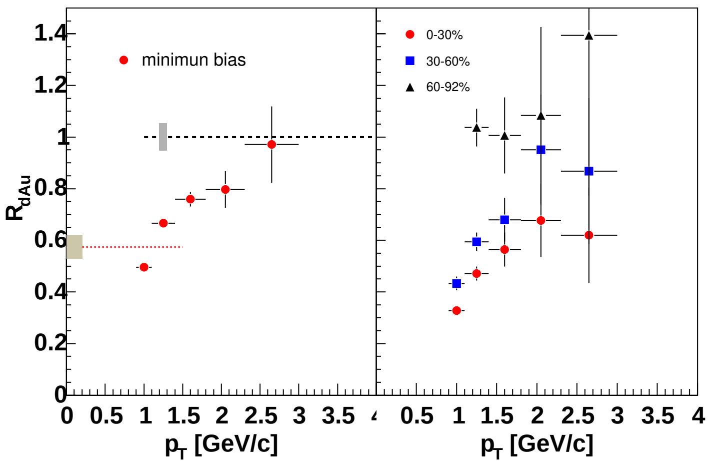

Figure 4.18: *R_{dAu} for negatively charged pions at pseudo-rapidity $\eta = 2.2$ for minimum bias (left) and different centrality (right) d+Au collisions at $\sqrt{s_{NN}} = 200$ GeV. The dotted and dashed lines in the figure indicate the expectations of participant scaling and binary scaling, respectively. The shaded bars represent the systematic errors associated with the determination of these quantities. The experimental error bars indicate statistical errors only. Systematic errors other than the uncertainties in $\langle N_{coll}\rangle$ determinations are estimated to be 8%.*

In Figure 4.18 R_{dAu} is shown as a function of p_T for π^- at pseudo-rapidity $\eta = 2.2$ for minimum bias (left) and three different centrality (right) d+Au collisions at $\sqrt{s_{NN}} = 200$ GeV. The dotted and dashed lines in the figure indicate the expectations of participant scaling and binary scaling, respectively. The shaded bars represent the systematic errors associated with the determination of these quantities. The experimental error bars indicate statistical errors only. Systematic errors other than the uncertainties in $\langle N_{coll}\rangle$ determinations are estimated to be less than 8%[4]. In contrast to a Cronin-like enhancement of high p_T non-identified charged hadron yields at mid-rapidity, the data show the high p_T yields of negatively charged pions are suppressed in central d+Au collisions at pseudo-rapidity $\eta = 2.2$. The more central the collisions are, the stronger the suppression is. The suppression of non-identified charged hadrons at forward rapidity has also been observed by the BRAHMS experiment [108]. This high p_T suppression at forward rapidity indicates a fraction of charged pion suppression at forward rapidity in central Au+Au collisions may be attributed to other suppression mechanisms, e.g. CGC [118].

4.2.4 Comparison with Inclusive Charged Hadrons

Figure 4.19 shows the measurements of R_{AuAu} for charged pions compared to those for inclusive charged hadrons at both mid-rapidity (left) and pseudo-rapidity $\eta = 2.2$ (right)

[4]Since the experimental setup is the same in p+p and d+Au 2003 runs at forward rapidity, it is expected that a large fraction of systematic uncertainties cancels out.

for 0-10% central Au+Au collisions at $\sqrt{s_{NN}} = 200$ GeV. For inclusive charged hadrons, both the published data [102] by BRAHMS and the results from the present analysis are shown. Compared to the published data, the present analysis demonstrates a smaller suppression at mid-rapidity but a stronger suppression at forward rapidity. These discrepancies are partly due to the difference in the reference spectra used in the two analyses and partly due to the difference in the reconstructed spectra of inclusive charged hadrons in Au+Au collisions as shown in Figure 4.6. Although the systematic error for the measurements of nuclear modification factors is rather large, the physical observation is essentially unchanged, i.e. high p_T inclusive charged hadron yields are suppressed at both mid-rapidity and forward rapidity in central Au+Au collisions. The high p_T suppression is even stronger at forward rapidity than that at mid-rapidity. Furthermore, the present analysis shows that high p_T charged pions are more strongly suppressed than inclusive charged hadrons at both mid-rapidity and $\eta = 2.2$. However, at mid-rapidity our data show that at low p_T charged pions are less suppressed compared to inclusive charged hadrons. This might be due to the strong collective flow effect which boosts particles to higher transverse momenta leading to larger deficits for heavier particles at low p_T.

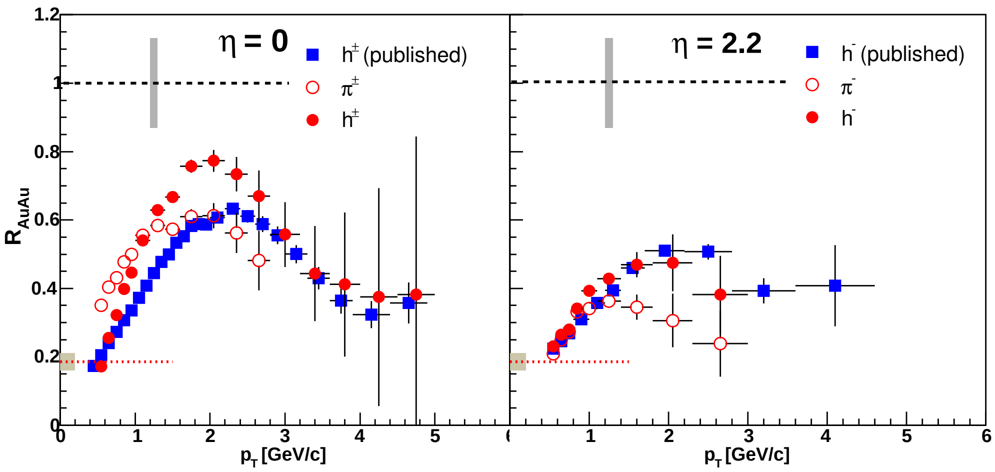

Figure 4.19: *A comparison of R_{AuAu} for charged pions with that for inclusive charged hadrons at mid-rapidity (left) and pseudo-rapidity $\eta = 2.2$ for 0-10% central Au+Au collisions at $\sqrt{s_{NN}} = 200$ GeV. The published data are taken from [102].*

4.2.5 Model Comparisons

The dominating models for high p_T suppression in central Au+Au collisions are based on the multiple scattering and induced gluon radiation energy loss of partons as they traverse a dense, strongly interacting medium. The predictions of R_{AuAu} at high p_T thus depend on the parton energy loss as discussed in 2.4.3.

Figure 4.20 shows the model predictions on the R_{AuAu} for π^0 at mid-rapidity in 0-10% central Au+Au collisions at $\sqrt{s_{NN}} = 200$ GeV. The BDMPS approach [72] for a thick QGP tends to over-predict the quenching at RHIC energy and leads to a too strong suppression [110]. In Vitev and Guylassy's approach [111], the energy loss is calculated via an opacity or higher twist expansion [77] in finite and expanding nuclear matter. At RHIC energies, they found that jet quenching dominates over k_T broadening and nuclear shadowing effects and the approximately constant suppression pattern of π^0 is well reproduced. In Wang's approach [112], the detailed balance of stimulated gluon emission and thermal absorption is included in the energy loss calculation [78] and the model reproduces PHENIX π^0 data well. Also shown in the figure is our measurements of R_{AuAu} for charged pions, which are different from PHENIX π^0. However, first of all one should be aware that there are uncertainties in our constructed reference spectrum for charged pions in p+p collisions. Secondly, we notice that the central (0-10%) to peripheral (60-92%) ratios of binary-collision-scaled p_T spectra, R_{CP}, as a function of p_T measured by PHENIX for charged pions are different from π^0, as reported in [113] and reproduced in Figure 4.21. Thirdly, we also notice that the average number of binary collisions for the 0-10% central Au+Au collisions determined by PHENIX is larger than that determined by BRAHMS[5], indicating that the 0-10% central collisions in PHENIX correspond to more central events compared to BRAHMS. Finally, PHENIX also demonstrates a stronger high p_T suppression for inclusive charged hadrons as compared to STAR and BRAHMS measurements (see Figure 4.30). Nevertheless, both PHENIX and BRAHMS data have demonstrated a strong suppression of high p_T pion yields in central Au+Au collisions.

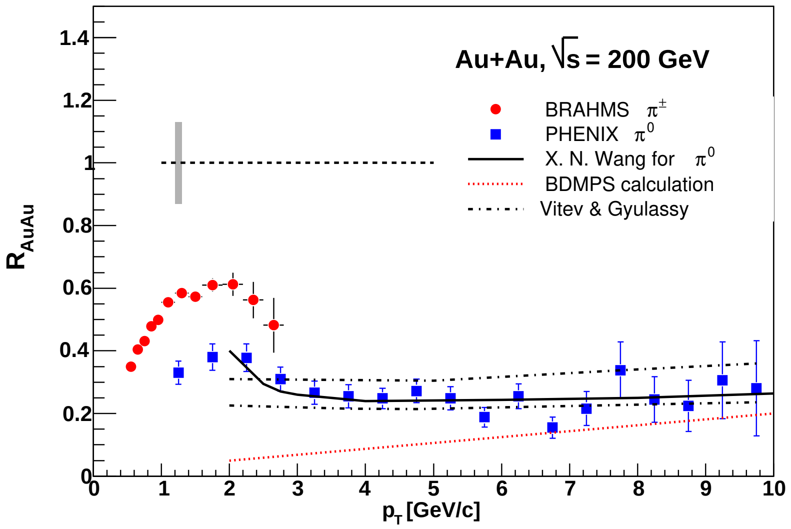

Figure 4.20: *Comparison of R_{AuAu} for charged pions (BRAHMS) and neutral pions (PHENIX) to calculations from BDMPS model [110], Vitev & Guylassy's model [111] with a gluon density dN^g/dy in the range of 800-1200 and Wang's model [112].*

Another very different interpretation of the suppression observed in central Au+Au

[5] The average number of binary collisions is 955.4 in PHENIX but 897 in BRAHMS for the 0-10% central Au+Au colllisions

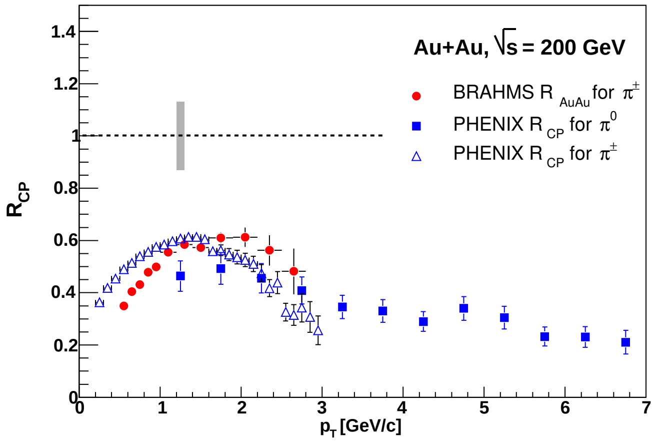

Figure 4.21: *Central (0-10%) to peripheral (60-92%) ratios of binary-collision-scaled p_T spectra, R_{CP}, as a function of p_T for charged pions and π^0 measured by PHENIX in Au+Au collisions at $\sqrt{s_{NN}}$ = 200 GeV. The data points are taken from [113]. Also shown in the figure is our measurements of R_{AuAu} for charged pions in 0-10% central Au+Au collisions.*

collisions is based on initial-state parton saturation effects [114]. The gluon density is expected to saturate for momenta below a saturation scale Q_s^2, which is calculated to be 2 GeV$^2/c^2$ at RHIC energy [115]. The saturation model has rather successfully predicted the rapidity, energy and centrality dependence of charged particle multiplicities in Au+Au collisions [9, 116]. In [114], it was also proposed that gluon saturation alone may account for a significant part of the observed high p_T hadron suppression. It was argued that saturation not only affects the region around Q_s, but also affects regions at momenta as large as Q_s^2/Λ_{QCD}, i.e. $\mathcal{O}$(5-10 GeV/c) for central Au+Au collisions at RHIC energies.

In order to distinguish initial state effects from final state effects, d+Au collisions, where no final state medium is expected to present, have been measured in the 2003 RHIC run. A 30% suppression of high p_T hadron yields in d+Au collisions is expected [114] if the strong suppression observed in Au+Au collisions is due to gluon saturation. On the contrary, if the observed suppression in Au+Au collisions is due to final state effects, the Cronin effect is predicted to dominate over nuclear shadowing in the $x > 0.01$ range accessible at RHIC, leading to an enhancement of high p_T yields relative to binary scaled $p + p$ collisions at intermediate p_T range. As shown in Figure 4.11, no suppression but Cronin-like enhancement at mid-rapidity is seen at $p_T > 2$ GeV/c in d+Au collisions, indicating that the high p_T suppression observed in central Au+Au collisions is mainly due to final state effects. Thus, a strongly interacting dense partonic medium is most likely formed in central Au+Au collisions at RHIC energy, but the gluon saturation or the Color Glass Condensate may provide the favorable initial conditions for the thermalization of parton modes with transverse momenta $\sim Q_s$ [117].

However, the arguments for the gluon-saturation-caused suppression should hold for sufficiently small x. The gluon saturation model is expected to be more reliable to make predications or applications at higher energies and/or more forward rapidities where smaller values of x in the target are probed. The gluon saturation scale depends on the gluon density and thus on the number of nucleons, and is connected with the rapidity y of measured particles by $Q_s^2 \sim A^{1/3}e^{\lambda y}$ [118], where $\lambda \sim 0.2$-0.3 is obtained from fits to HERA data. Thus it is supposed that a suppression of high p_T yields at forward rapidity with R_{dAu} being a decreasing function of centrality in d+Au collisions would indicate the Color Glass Condensate formation at RHIC energy.

Figure 4.22 shows a comparison of R_{dAu} for negatively charged pions at $\eta = 2.2$ in minimum-bias d+Au collisions at $\sqrt{s_{NN}} = 200$ GeV to theoretical calculations. The pQCD calculation [119], which includes initial multiple scattering and conventional nuclear shadowing effect, shows that R_{dAu} tends to increase above unity and peaks at $p_T \sim 3$ GeV/c. But it is difficult for the pQCD calculation to reproduce the centrality dependence of R_{dAu} as shown in the right panel of Figure 4.18 since the multiple scattering will lead to stronger enhancement for the more central collisions if a centrality independent nuclear shadowing is assumed. While the calculation from gluon saturation [120] predicts that $R_{dAu} < 1$ but a too small R_{dAu}, the data show the centrality dependence of R_{dAu} at forward rapidity agrees qualitatively with the prediction of Color Glass Condensate formalism, i.e. R_{dA} decreases with centrality. Even though it is not sufficient to conclude that the gluon saturation effect has its manifestation in the forward rapidity, the high p_T suppression at pseudo-rapidity $\eta = 2.2$ in central d+Au collisions indicates a fraction of high p_T suppression in the forward region of Au+Au collisions should be attributed to initial state effects.

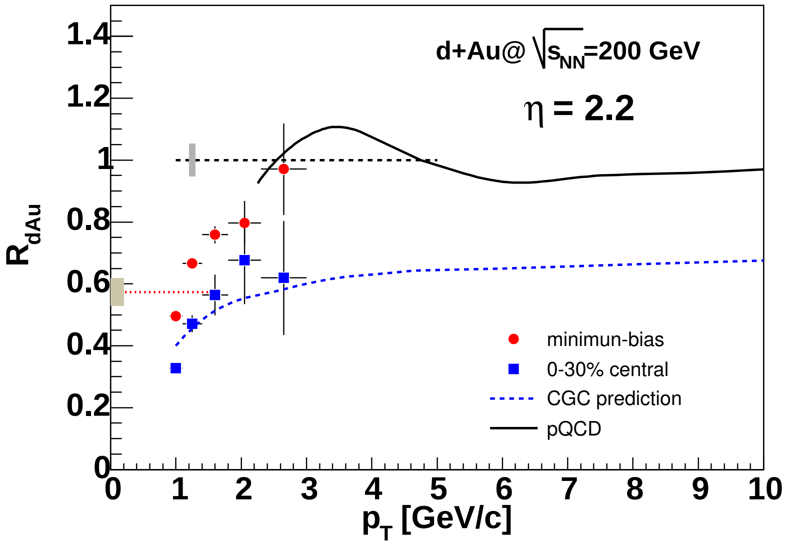

Figure 4.22: *Comparison of R_{dAu} for negatively charged pions at $\eta = 2.2$ in minimum-bias and 0-30% central d+Au collisions to calculations from pQCD-based model [119] and gluon saturation model [120] for minimum-bias d+Au collisions.*

4.3 Particle Composition

4.3.1 p/π^+ and $\bar{p}/\pi^-$ Ratios

In Figure 4.23, the p/π^+ and $\bar{p}/\pi^-$ ratios at mid-rapidity are shown as a function of p_T for the 0-10% central Au+Au collisions at $\sqrt{s_{NN}} = 200$ GeV. The error bars on our data are statistical only. The systematic errors are estimated to be less than 8%. The ratios increase rapidly at low p_T and the yields of both protons and anti-protons are comparable to the pion yields for $p_T > 2$ GeV/c. For comparison, the corresponding ratios for $p_T > 2$ GeV/c observed in $p+p$ collisions at $\sqrt{s} = 63$ GeV [51] and in gluon jets produced in $e^+ + e^-$ collisions [109] are also shown. In hard-scattering processes described by pQCD, the p/π^+ and $\bar{p}/\pi^-$ ratios at high p_T are determined by the fragmentation of energetic partons, independent of the initial colliding system, which is seen as agreement within the uncertainties between $p+p$ and $e^+ + e^-$ collisions. Thus, the clear increase in the p/π^+ and $\bar{p}/\pi^-$ ratios at high p_T from the $p+p$ and $e^+ + e^-$ to the central Au+Au collisions requires production mechanisms other than pQCD.

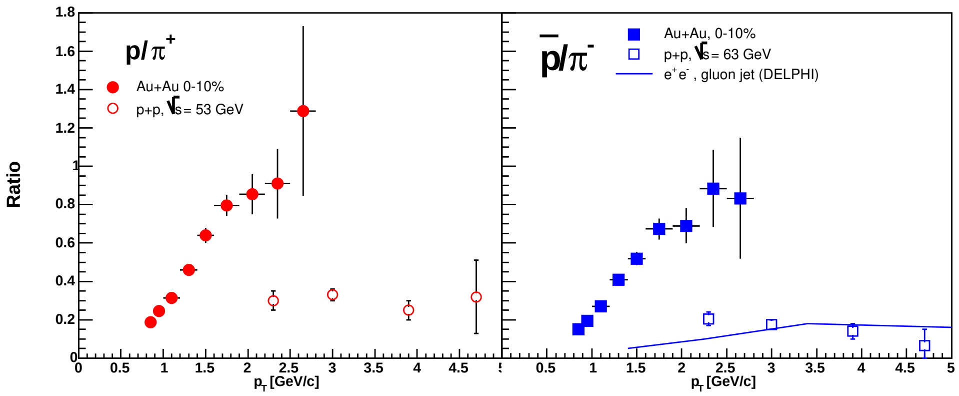

Figure 4.23: *p/π^+ (left) and $\bar{p}/\pi^-$ (right) ratios at mid-rapidity for 0-10% central Au+Au collisions at $\sqrt{s_{NN}} = 200$ GeV. The error bars show the statistical errors. The systematic errors are estimated to be less than 8%. Data at $\sqrt{s} = 63$ GeV $p+p$ collisions [51] are also shown. The solid line is the $(p+\bar{p})/(\pi^+ + \pi^-)$ ratio measured in gluon jets [109].*

To illustrate the effect of Jacobian transformation from rapidity to pseudo-rapidity, Figure 4.24 shows the $\bar{p}/\pi^-$ ratios at mid-rapidity by using both η and y. Because the Jacobian effect on proton is larger than that on pion, the ratios by using pseudo-rapidity are systematically smaller than using rapidity.

For comparison, the $\bar{p}/\pi^-$ ratios at both mid-rapidity and pseudo-rapidity $\eta = 2.2$ are shown in Figure 4.25 as a function of p_T for the 0-10% central Au+Au collisions at $\sqrt{s_{NN}} = 200$ GeV. For $p_T < 1.5$ GeV/c, the $\bar{p}/\pi^-$ ratio at $\eta = 2.2$ is larger than that at $\eta = 0$, while the opposite behavior is seen for $p_T > 2$ GeV/c. The systematic errors for the $\bar{p}/\pi^-$ ratios at pseudo-rapidity $\eta = 2.2$ are estimated to be 10%.

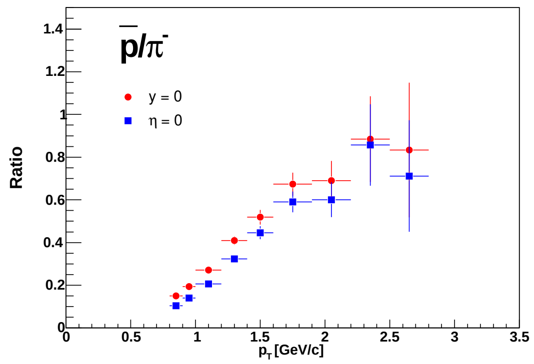

Figure 4.24: *Jacobian transformation effect on $\bar{p}/\pi^-$ ratios at mid-rapidity for 0-10% central Au+Au collisions at $\sqrt{s_{NN}} = 200$ GeV.*

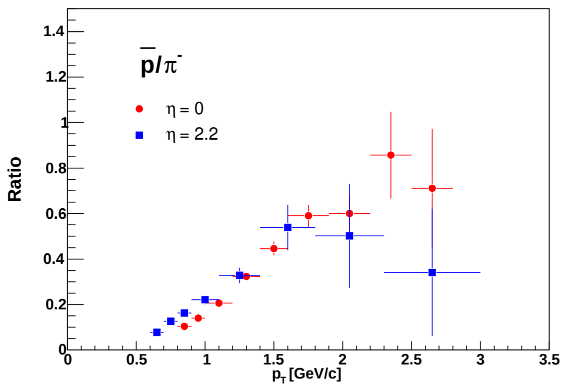

Figure 4.25: *$\bar{p}/\pi^-$ ratios at both mid-rapidity and pseudo-rapidity $\eta = 2.2$ for 0-10% central Au+Au collisions at $\sqrt{s_{NN}} = 200$ GeV. The error bars show the statistical errors only. The systematic errors are estimated to be 10% for $\bar{p}/\pi^-$ ratios at $\eta = 2.2$.*

4.3.2 p/h^+ and $\bar{p}/h^-$ Ratios at Mid-rapidity

In order to investigate the dependence of particle composition on the initial colliding system, we have extended the PID capability of the TOFW for (anti-)protons to 3 GeV/c in the d+Au and $p+p$ data analyses by applying an asymmetric PID cut the same way as in the Au+Au data analysis for charged pions. Figure 4.26 shows the resulting p/h^+ and $\bar{p}/h^-$ ratios as a function of p_T for 0-10% central Au+Au, 0-30% central d+Au and minimum-bias $p+p$ collisions at $\sqrt{s_{NN}} = 200$ GeV. Only statistical errors are shown in the figure. The data show that the p/h^+ and $\bar{p}/h^-$ ratios in d+Au and $p+p$ collisions at $p_T > 2.0$ GeV/c are around 0.2, while they are about a factor of 2 higher in central Au+Au collisions indicating an enhanced baryon production at intermediate transverse momentum.

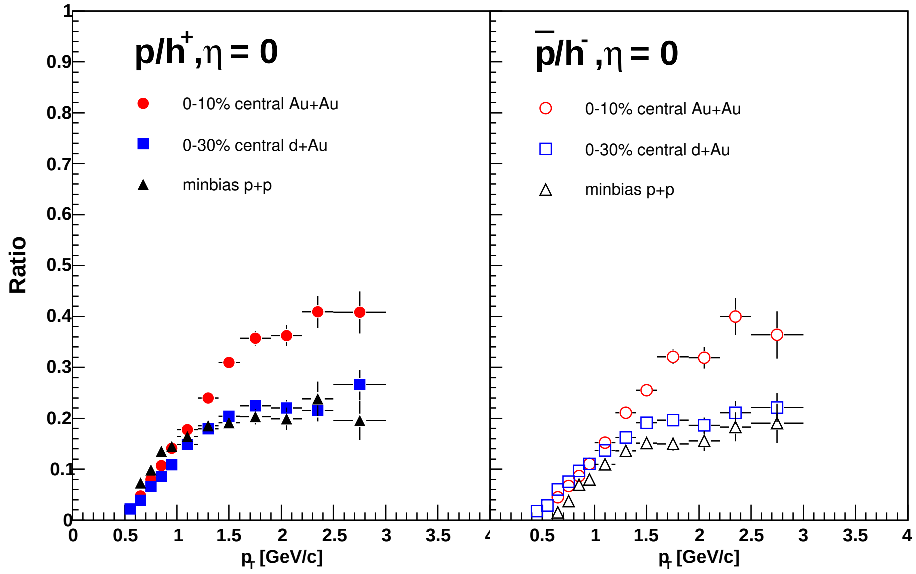

Figure 4.26: *p/h^+ and $\bar{p}/h^-$ ratios at mid-rapidity for 0-10% central Au+Au, 0-30% central d+Au and minimum-bias $p+p$ collisions at $\sqrt{s_{NN}}$ = 200 GeV. The error bars indicate the statistical errors only.*

4.3.3 π^-/h^- at Pseudo-Rapidity $\eta = 2.2$

In contrast to mid-rapidity, at pseudo-rapidity $\eta = 2.2$ pions can be well identified up to quite high p_T in d+Au and p+p data analyses. The π^-/h^- ratios are shown in Figure 4.27 as a function of p_T for 0-10% central Au+Au, 0-30% central d+Au and minimum-bias p+p collisions at $\sqrt{s_{NN}} = 200$ GeV. The data show within uncertainties that π^-/h^- ratios in d+Au collisions are similar to those in $p+p$ collisions. However, at $p_T > 1.5$ GeV/c, the abundance of π^- relative to inclusive negatively charged hadrons in d+Au and $p+p$ collisions is about a factor of 1.5 higher than that in central Au+Au collisions, indicating an enhancement of baryon yields and a suppression of pion yields at intermediate p_T at pseudo-rapidity $\eta = 2.2$ in central Au+Au collisions.

4.3.4 Comparison with Other Experiments

The p/π^+ and $\bar{p}/\pi^-$ ratios in Au+Au collisions have also been measured by PHENIX experiment [113]. Figure 4.28 shows a comparison of the ratios reported in this thesis for 0-10% central Au+Au collisions at $\sqrt{s_{NN}}$ = 200 GeV with PHENIX data. The p/π^+ and $\bar{p}/\pi^-$ ratios from the present analysis are systematically higher than PHENIX measurements because the feed-down corrections for the Λ and $\bar{\Lambda}$ have not yet been applied in our analysis.

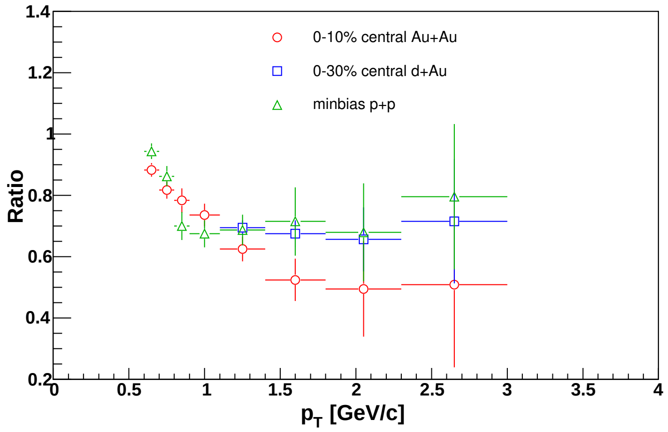

Figure 4.27: *π^-/h^- ratios at pseudo-rapidity $\eta = 2.2$ for 0-10% central Au+Au, 0-30% central d+Au and minimum-bias $p+p$ collisions at $\sqrt{s_{NN}} = 200$ GeV. The error bars indicate the statistical errors only.*

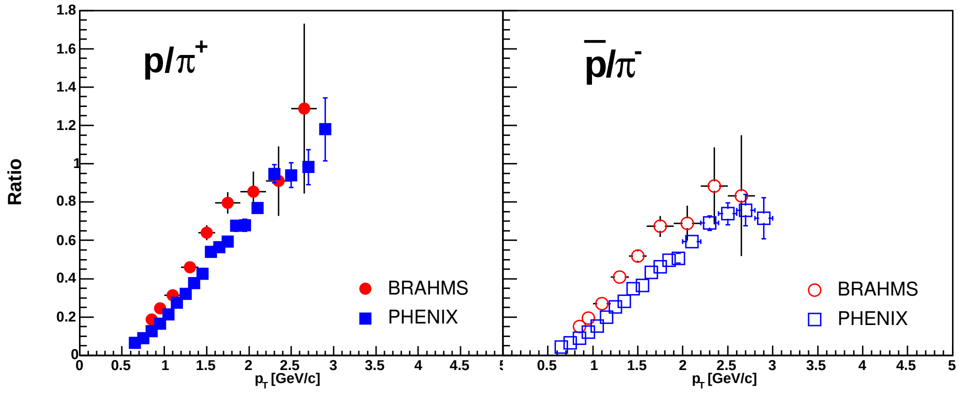

Figure 4.28: *Comparison of p/π^+ and $\bar{p}/\pi^-$ ratios reported in this thesis for 0-10% central Au+Au collisions at $\sqrt{s_{NN}} = 200$ GeV with PHENIX measurements [113].*

4.3.5 Model Comparisons

Two kinds of models have been proposed to explain the experimental results on the p_T dependence of p/π^+ and $\bar{p}/\pi^-$ ratios. One is the parton recombination model [84, 85] and the other is the baryon junction model [83]. Both models can explain qualitatively the observed feature of p/π enhancement in central collisions. Furthermore, both theoretical models predict that this baryon enhancement is limited to $p_T <$ 5-6 GeV/c. Figure 4.29 shows the result from a parton recombination model [85] together with our measurements of $\bar{p}/\pi^-$ ratios at mid-rapidity and pseudo-rapidity $\eta = 2.2$ in Au+Au collisions at $\sqrt{s_{NN}} = 200$ GeV. The solid and dashed curves correspond to calculations with and without collective flow in the quark-gluon plasma, respectively. The calculation with a flow velocity of $0.5c$ reproduces our data at mid-rapidity. The data at pseudo-rapidity $\eta = 2.2$ indicate that the collective flow is smaller at $\eta = 2.2$ than at mid-rapidity but greater than 0.

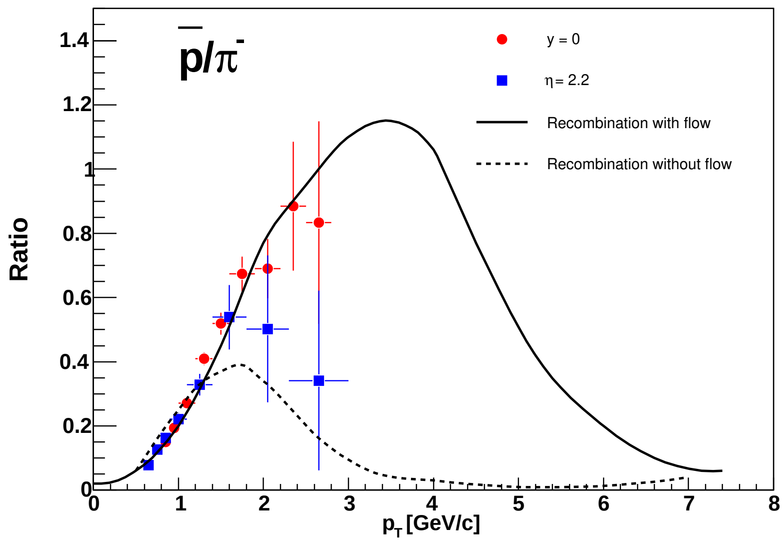

Figure 4.29: *Ratios of $\bar{p}/\pi^-$ calculated by the parton recombination model [85] with (solid curve) and without (dashed curve) collective flow in the quark-gluon plasma together with our measurements.*

The baryon junction model is found to be able to reproduce the p/π^+ and $\bar{p}/\pi^-$ ratios measured by the PHENIX experiment for Au+Au collisions at $\sqrt{s_{NN}} = 130$ GeV, but so far no calculation has been made for $\sqrt{s_{NN}} = 200$ GeV collisions. It is worthwhile to mention that baryon junction mechanism was originally proposed to enhance baryon production in order to explain the strong stopping observed at SPS energy. But data at RHIC energy show that the HIJING model with baryon junction overestimates the net-proton yields in the rapidity range of $-0.05 < y < 2$ by a factor of 2 [14].

4.4 Summary

To summarize, Figure 4.30 shows that charged hadron yields per nucleon-nucleon collisions at mid-rapidity in central Au+Au collisions at $\sqrt{s_{NN}} = 200$ GeV are significantly suppressed compared to nucleon-nucleon collisions although the differences between the four experiments are rather large. The results from the present analysis for 0-10% central Au+Au collisions are also shown in the figure and seem to be more consistent with STAR's measurements for 0-5% central Au+Au collisions. Furthermore, the present analysis shows that identified charged pions are more strongly suppressed compared to inclusive charged hadrons at both mid-rapidity and forward rapidity in central Au+Au collisions. The suppression of charged pion yields at $\eta = 2.2$ is even stronger than that at mid-rapidity. However, no high p_T suppression of (anti-)protons has been observed at both mid-rapidity and forward rapidity. The ratios of p/π^+ and $\bar{p}/\pi^-$ at mid-rapidity show that (anti-)proton yields are comparable to the pion yields at intermediate p_T and can be well reproduced by a parton recombination model incorporating with strong collective flow effects. To account for the $\bar{p}/\pi^-$ ratio at $\eta = 2.2$, a smaller flow velocity is suggested.

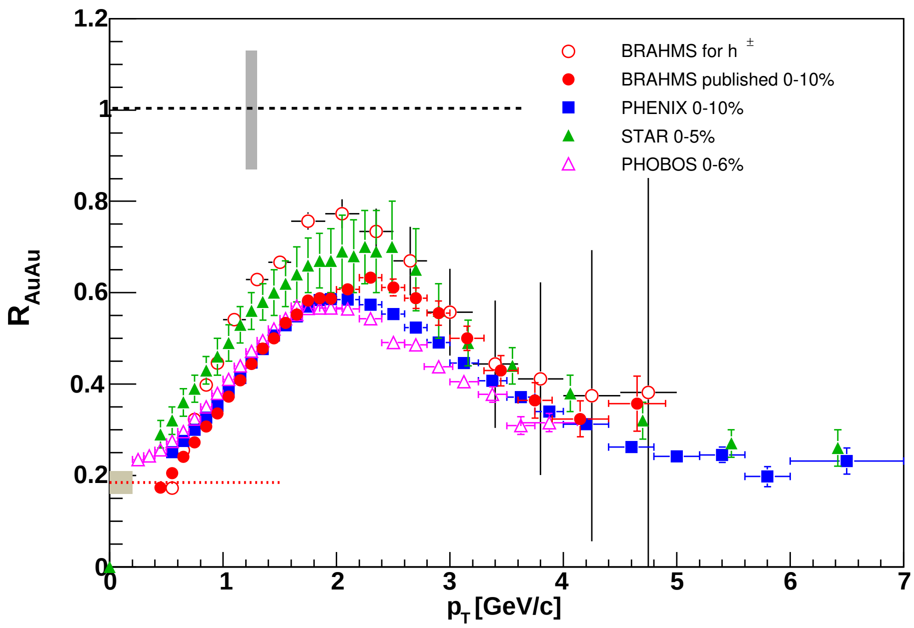

Figure 4.30: R_{AuAu} *for inclusive charged hadron at mid-rapidity for central Au+Au collisions at* $\sqrt{s_{NN}} = 200$ *GeV measured by BRAHMS [102], PHENIX [121], PHOBOS [122] and STAR [123]. The results from the present analysis are shown as open circles.*

To distinguish the final state effect from the initial state effect, data for d+Au collisions have been analyzed. All four experiments have shown a Cronin-like enhancement of high p_T inclusive charged hadron yields at mid-rapidity in d+Au collisions. This enhancement is widely seen as an indication that the suppression in central Au+Au collisions is not an initial state effect but a final state effect. However, the present data analysis shows that the negatively charged pion yields are also suppressed at forward rapidity in central d+Au collisions. The more central the collisions is, the stronger the suppression is. This suppression and its centrality dependence are qualitatively consistent with the gluon saturation model (or CGC) predictions. This indicates that, in addition to jet quenching, the gluon saturation effect might be attributed to the strong high p_T suppression observed at forward rapidity in central Au+Au collisions. Thus, in order to disentangle different nuclear medium effects, it is essential to determine the dependence of energy loss on, e.g. parton flavor, the energy density and size of the partonic matter, i.e. to understand the properties of the strongly interacting partonic matter. To determine how much of the suppression should be accounted for by the gluon saturation, it is important for gluon saturation models to be formalized to give quantitative predictions. Since gluon saturation is expected to be more reliable at higher energies and/or higher rapidity, the CGC, if any, should manifest itself at both mid-rapidity and forward rapidity at LHC energy.

Chapter 5

Outlook: High p_T Physics with PHOS at ALICE

The colliding energy for Pb+Pb collisions at the LHC will be $\sqrt{s_{NN}} = 5.5$ TeV, a factor of about 30 higher than that available at RHIC. Heavy-ion collisions at the LHC will thus access a both quantitatively and qualitatively new physics regime with much higher energy density. It is expected that particle production at LHC is determined by the high density (saturated) parton distributions and hard processes. In particular, very hard strongly interacting probes, whose attenuation can be used to study the early stages of the collision, will be produced at sufficiently high rates for detailed measurements. Weakly interacting hard probes such as direct photons, which will provide information about nuclear parton distributions at very high Q^2, become accessible.

The PHOS detector in ALICE experiment is dedicated to measuring photons, π^0 and η in a board p_T range from about a hundred MeV/c to 100 GeV/c. In this chapter we present the PHOS readout electronics required for high p_T physics, the data acquisition system built for PHOS beam test and the performance of a PHOS prototype.

5.1 The ALICE Experiment

ALICE is optimized for the study of heavy-ion collisions at $\sqrt{s_{NN}} = 5.5$ TeV. The primary goal is to explore in detail the behavior of matter at extremely high energy densities and temperatures, with the intent to elucidate the characteristics of the predicted phase transition from a quark-gluon plasma to hadronic matter [124].

ALICE is a sophisticated detector system consisting of three main parts: (1) the central part, contained in the L3 magnet and composed of detectors mainly devoted to probing the hadronic signals and di-electrons in pseudo-rapidity of $-0.9 < \eta < 0.9$ over the full azimuthal angle, (2) the forward muon spectrometer for detecting muon pairs from the decay of heavy quarkonia in the interval $2.5 < \eta < 4.0$, and (3) the forward detectors used to determine the multiplicity and serve as a fast centrality trigger. The central part comprises a large solenoidal magnet from the L3 experiment with a silicon Inner Track System (ITS), a Time Projection Chamber (TPC), Time-Of-Flight (TOF), Ring Image Čerenkov (RICH), and Transition Radiation Detector (TRD) to measure hadrons and electrons, and the PHOton Spectrometer (PHOS) to measure photons. The layout of the ALICE setup is shown in Figure 5.1. The complete layout of the ALICE detector as proposed initially together with the objectives is described in the ALICE Technical Proposal [125]. The individual sub-detectors are described in detail in their respective technical design reports.

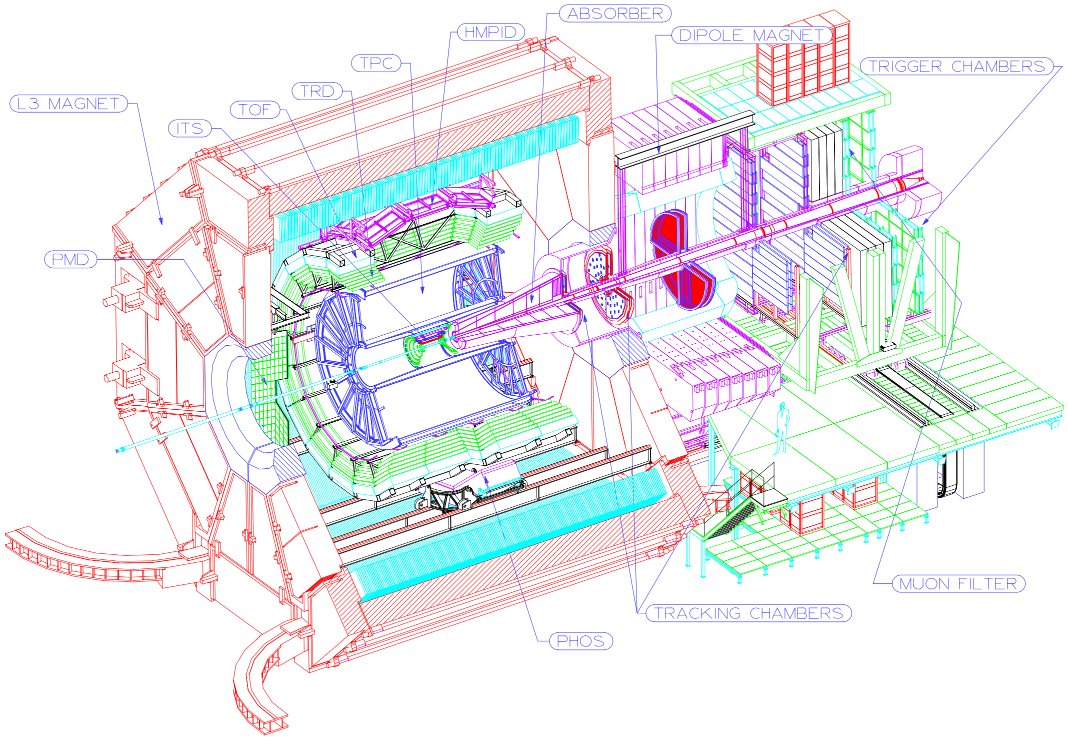

Figure 5.1: *The ALICE detector layout.*

The ALICE detector is designed with the goal to measure reliably the majority of particles produced in central Pb+Pb collisions over a large rapidity interval. The technical challenge of the experiment is imposed by the large number of particles produced in central Pb+Pb collisions at $\sqrt{s_{NN}} = 5.5$ TeV. This dictates a fine detector granularity, and a corresponding large number of readout channels. Other designed considerations are imposed by the large data volume and slow readout of the TPC detector. While the anticipated Pb+Pb interaction rate is high, ~ 8 kHz, the TPC event rate is limited to about 20 Hz for central Pb+Pb collisions due to the large TPC data volume and limited bandwidth for data recording. This implies the need for special physics triggers to select interesting events for readout. The need for a trigger is made even more pressing by the rarity of the most interesting hard probes, such as high p_T photon and jet production. An important detector in ALICE which focuses on hard probes and high p_T physics is a high resolution photon spectrometer as described in the following section.

5.2 The PHOS Detector

The PHOS [126], which is devoted to the study of photon signals, is a high resolution electromagnetic calorimeter consisting of a highly segmented ElectroMagnetic CAlorimeter (EMCA) and a Charged-Particle Veto (CPV) detector. The EMCA consists of 17920 detection channels of lead-tungsten crystals, $PbWO_4$ (PWO), of $2.2 \times 2.2 \times 18$ cm^3 dimensions. This corresponds to 1.1 Molière radius square in cross section and 20 radiation lengths in length. The crystals will be coupled to 5×5 mm^2 avalanche photo-diodes (APDs) which signals are processed by low-noise charge-sensitive pre-amplifiers. The PHOS is subdivided into 5 modules, each consisting of 64×56 channels, positioned along an arc on the bottom of the ALICE setup at a distance of 440 cm from the nominal interaction point in order to maintain the required low detector element occupancy. With a total area of ~ 8 m^2 it will cover approximately a quarter of a unit in pseudo-rapidity, $-0.12 \leq \eta \leq 0.12$, and 100° in azimuthal angle. The main mechanical assembly unit in a module is the crystal strip unit consisting of 2×8 crystals. The APD and the pre-amplifier are integrated in a common body glued onto the end face of the crystal.

Because the light yield of PWO depends strongly on the temperature with a coefficient of $\sim -2\%$ per °C, the working temperature for PHOS will be held at -25°C with a precision of ~ 0.3°C to significantly increase the light yield and reduce the thermal noise of the photo-detector and pre-amplifier. For this purpose the PHOS modules are subdivided by thermo-insulation into a "cold" and "warm" volume. The crystal strips including integrated APD and pre-amplifier are located in the "cold" volume, whereas other electronics are mounted on cards located in the "warm" volume.

The CPV, a Multi-Wire Proportional Chamber (MWPC) [129, 130] used to reject charged hadrons, consists of five separate modules located on the top of the EMCA modules at a distance of ~ 5 mm. Its detection efficiency for charged particle is better than 99%, and the spatial position resolution is ~ 1.6 mm in both directions.

5.2.1 Physics with PHOS

The PHOS detector is designed to measure photons and also π^0 and η via their 2γ decay branch. Detection of a direct photon signal, which is considered to be the best means to determine the temperature of the initial phase of the collision, is a primary goal of the PHOS physics program [126]. In addition, measurements of the π^0 and η p_T spectra up to 100 GeV/c can provide important information both on final- and initial-state effects on particle production. Furthermore, detection of high energy photons will allow to trigger on hard scatterings in which a jet has been produced (γ-tagged jet). The emitted photon which escapes unaffected by the medium, will provide a kinematic tag for the recoiling quark or gluon which might be affected by the hot and dense matter. Jet quenching, which has been confirmed by the RHIC experiments, is considered to be an important probe of the deconfined QGP and will be especially pronounced at LHC energies due to the expected large jet cross section. The cross section will be orders of magnitude larger at high p_T at the LHC than at RHIC. Recently data from PHENIX experiment indicate that the π^0 and γ spectra are most likely extended to about 100 GeV/c in transverse momentum at $\sqrt{s_{NN}} = 5.5$ TeV. By triggering on a high p_T photon in PHOS and searching for and reconstructing a jet in TPC, one can extract the effective fragmentation function. As a consequence of the physics results at RHIC, the requirements of PHOS have been extended 1) to cover larger p_T range leading to the use of APDs instead of PIN diodes[1] as the photo-detectors, and 2) to provide a high p_T trigger for measuring high p_T spectra of π^0 and γ.

5.3 The PHOS Front-End Electronics and Readout

The PHOS front-end electronics (FEE) chain includes energy digitization, timing for time-of-flight discrimination against low energy (anti-)neutrons and a trigger logic for generating level 0 (L0) and level 1 (L1) triggers for ALICE. In this section we present the physics requirements and the current conceptional design of the PHOS FEE.

5.3.1 Requirements

The main physics requirements for the front-end electronics are summarized in Table 5.1.

Least count energy per channel	5-10 MeV
Full energy per channel	100 GeV
Energy channel dynamic range	10,000-20,000
Timing resolution	~ 1 ns at 1-2 GeV
Trigger	L0 and L1
Max channel counting rate in Pb+Pb	2 kHz (by assuming 20% occupancy)
Max channel counting rate in $p+p$	200 Hz (at $\sqrt{s} = 14$ TeV, see section 5.3.2)
APD gain control	individual bias setting

Table 5.1: *Physics requirements to the PHOS front-end electronics.*

In order to measure high p_T photons up to a hundred GeV, the design requires a very large dynamic range. To obtain an optimum energy resolution for the low energy region up to 10 GeV, together with less stringent resolution requirement for high energy region, it is desired that each shaper channel supplies at least two outputs with "low" and "high" amplification, digitized by separate ADCs.

The time-of-flight for a photon and a 2 GeV/c neutron reaching the front of PHOS is $\sim$ 14.7 ns and 16.2 ns, respectively. Thus TOF capabilities for all channels with a resolution of $\sim$ 1 ns can be used to discriminate against 1-2 GeV/c (anti-)neutrons.

The amplification factor for the APD is strongly dependent on the bias voltage. Furthermore, the spread in the crystal light yields and efficiency in the crystal-APD coupling will further increase the effective gain variance under beam conditions. A large spread in APD gain would result in either overflow in high-gain channels or resolution degradation in low-gain channels and a significant degradation of the accuracy in the L0/L1 trigger sums. To reduce the effect an individual bias voltage is required for each APD.

[1] PIN diodes are sensitive to punch-through particles from the electromagnetic shower in the $PbWO_4$ crystals.

To select rare high p_T events, PHOS has to be part of the ALICE trigger and provide L0 and L1 triggers within 800 ns[2] and 6.2 μs, respectively.

5.3.2 PHOS Trigger

Trigger rate

PHOS can provide an input to the L0 trigger. This trigger could be a minimum bias trigger in low multiplicity events, such as peripheral Pb+Pb collisions, $p+p$ interactions and photon+photon physics in Pb+Pb. PHOS can also provide a L1 trigger on high p_T events. The PHOS photon event rate and trigger efficiency have been investigated via simulation.

1. PHOS photon event rate in p+p interactions. A PHOS photon event is defined as one with at least one photon with an energy above noise (10 MeV). By using the PYTHIA [127] event generator for $p+p$ interactions at $\sqrt{s} = 5.5$ TeV at a luminosity of 3×10^{30} cm^{-2}s^{-1}, i.e. 200 kHz interaction rate[3], the PHOS event rate reaches 20 kHz as shown in Figure 5.2. Assuming an occupancy of one photon per event and a cluster size of 3×3 gives an average counting rate per channel of about 10 Hz. For $p+p$ interactions at $\sqrt{s} = 14$ TeV, the average counting rate per channel reaches about 200 Hz.

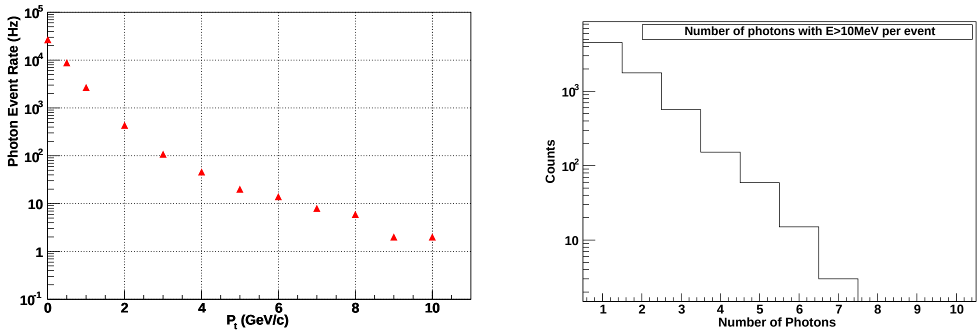

Figure 5.2: *Left: PHOS photon event rate versus p_T for p+p interactions at $\sqrt{s} = 5.5$ TeV at a luminosity of 3×10^{30} $cm^{-2}s^{-1}$. Right: Number of photons per event.*

2. High p_T trigger rate for Pb+Pb collisions. In order to derive an transverse energy (or p_T) trigger signal, all channels have to be passed to a filter function that calculates the energy sum over a $n \times m$ filter kernel. Different shapes of the sliding window, different sizes and a two-step approach[4] have been studied. Figure 5.3 illustrates the sliding window technique over a PHOS module with 64×56 channels. The trigger

[2] A L0 input has to be delivered to the Central Trigger Processor (CTP) within 800 ns.
[3] Interaction rate $R = \mathcal{L}\sigma$, where $\mathcal{L}$ and σ are luminosity and the interaction cross section.
[4] A cell of 2×2 is summed first and then a sum of 2×2 cells.

efficiency for triggering on single photons is plotted versus the sliding window size in the left panel of Figure 5.4. The sliding window sizes under study are 1×3 (in row and column), 2×2, 3×3 and 4×4. Simulation is done by embedding one single 10 GeV photon into a background event generated by a HIJING [69] parameterization in AliROOT [128]. It is considered as a trigger event if the energy sum of the considered window is greater than 9 GeV. Fake triggers are estimated by enriching the background events with high p_T (> 10 GeV/c) charged pions taking into account that there are 4 times more charged pions at $p_T > 10$ GeV/c than 10 GeV photons. In addition, the trigger efficiencies for different algorithms, e.g. a two step approach, are shown in the right panel of Figure 5.4. Any algorithm using a kernel size of at least 3×3, or a combination of a 2×2 sum (non-overlapping) first and a following a sum of 2×2 cells (i.e. 4×4 in channels) will give reasonable efficiency.

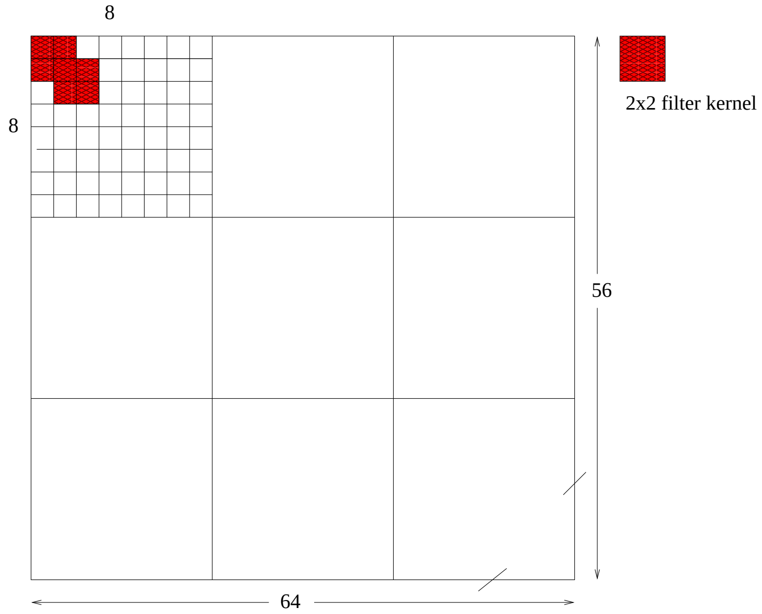

Figure 5.3: *Illustration of the sliding window technique over a PHOS module.*

The trigger rate for triggering on single photons versus a p_T threshold has been estimated by using the HIJING event generator and the result is shown in Figure 5.5 for Pb+Pb collisions. “Fake trigger rate”, the rate of trigger signal caused by charged pions, is estimated by the fake trigger event rate multiplied by the fake trigger probability[5] as shown for example in Figure 5.4. Below 6 GeV/c fake triggers dominate and below 2-3 GeV/c the fake trigger rate will saturate the ALICE DAQ and trigger system.

[5]The case # 1 was used for such study.

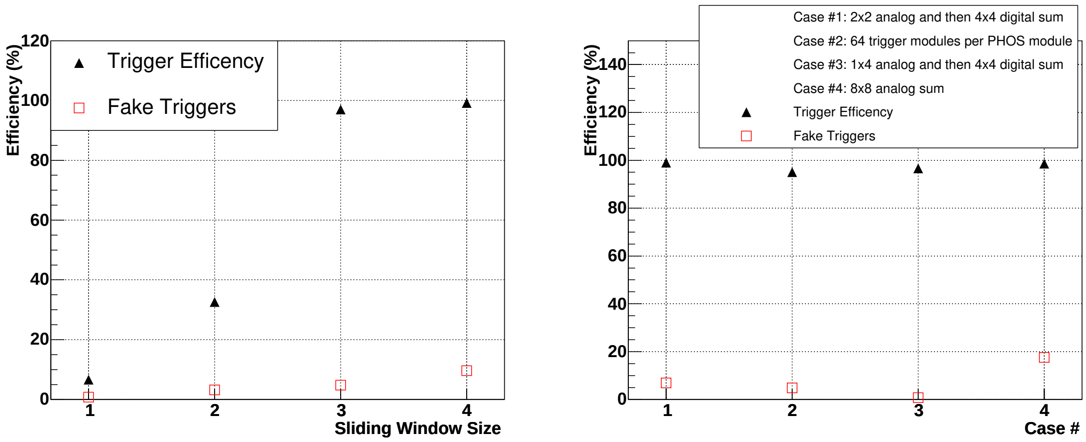

Figure 5.4: *Left: The trigger efficiency for triggering on single photons versus the sliding window size. Right: The trigger efficiency for triggering on single photons for different algorithms.*

L0 trigger

Simulations show that, with a fixed analog sum input of 2×2 to the FPGA-based trigger units, a trigger efficiency of 95% (excluding edge effects) is achievable by applying 4×4 (i.e. 2×2 cells with 2×2 channels) sliding window method over the whole trigger region.

The PHOS L0 trigger is conceived as a minimum bias trigger for p+p interactions at a latency of 800 ns. After subtraction of all delays, 200 ns is available to process the following algorithm:

1. Sample-wise charge summing of all 4×4 windows in parallel in 2D domain.
2. Pipelined summing of all 2D sums in consecutive samples.
3. Threshold comparison per window sum.
4. Peak finder look-up for LHC clock phase.
5. OR'ed output L0_YES.

A NRZ (No Return Zero) signal, synchronous with the 40 MHz clock of the LHC machine outputs a L0 decision from the FPGA at about 600 ns after collision so that it can arrive at the central trigger processor (CTP) within 800 ns over 40 m cable.

L1 trigger

The L1 trigger is sensitive to high p_T photons in Pb+Pb interactions at a maximum latency of 6.2 μs. Within the pure electronic L1 processing time of 5.6 μs, more ADC samples than for L0 can be processed and several different thresholds can be applied, each providing one trigger output.

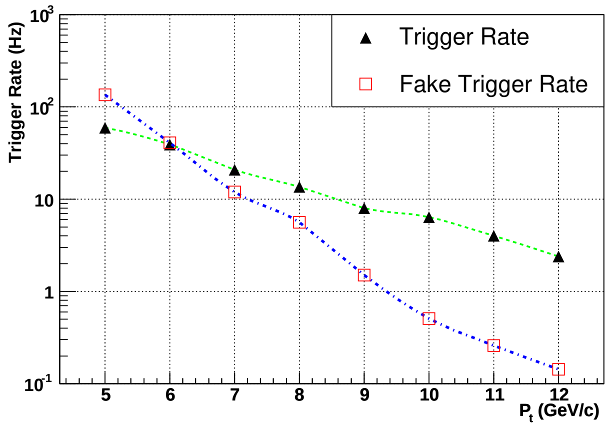

Figure 5.5: *Trigger and fake trigger rate for triggering on single photons versus a p_T threshold for Pb+Pb collisions.*

5.3.3 Conceptional Design of the PHOS FEE

The design guidelines are summarized as following:

1. Energy channels. The energy resolution for PHOS is optimized for the region up to 10 GeV, whereas the energy dynamic range for p_T coverage is 100 GeV. Because a linear 16-bit digitization will severely limit the resolution in the low energy region, it is essential to scale the dynamic range before digitization. Two amplifiers ($\times 1$ and $\times 10$) can be used for high and low energy ranges for each PHOS channel and the outputs can then feed 2 Altro-16[6] ADC channels.

2. Time-of-flight. The A/D converters of the Altro-16 chips operate at 40 MHz. By oversampling the energy signal and analyzing the pulse shape the time-of-flight can be determined with a resolution of ~ 1.6 ns or better [134].

3. Trigger. Each four energy signal channels (a cell of 2×2) are added into an analog sum with a fast shaping time. A sliding window of 2×2 cell digital sum and other trigger logic will be implemented in a FPGA.

4. APD-bias controller. In order to compensate for the APD gain differences, each APD should be biased at a specific high voltage. To control the bias voltage, an APD-bias controller needs to be implemented.

Figure 5.6 shows the configuration of PHOS front-end electronics and readout chain. FEE card will contain 32 channels with shaper and digitization logic for processing and timing [132]. In order to cover a p_T range up to 100 GeV/c, in each FEE card 32 energy channels are digitized with a resolution of 13 bits per crystal using two 10-bit ADCs and

[6]The Altro-16 chip, which is designed for the ALICE TPC, contains sixteen 10-bit ADC blocks.

a dual gain shaper of about 2 μs shaping time. The 64 ADCs are contained in four Altro-16 chips, which are sampled at 40 MHz. The Altro-16 chips also contain Multi-Event Buffers (MEB) which are filled and emptied by the ALICE L1 and L2 trigger signals. In addition, 8 trigger channels are obtained by analog summing of rectangular 2×2 crystal groups with a fast shaping time of 100 ns.

In addition, a 32-channel HV bias controller is situated on each FEE card. It distributes the nominal input voltage of 400 V to 32 individually programmable high voltage lines for APDs.

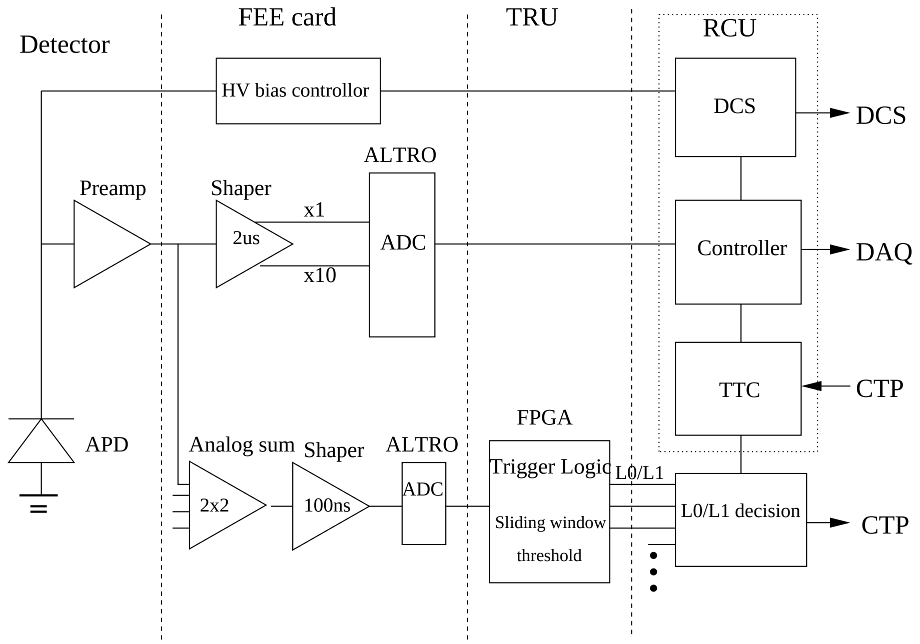

Figure 5.6: *The PHOS front-end electronic configuration.*

Arrays of 14 FEE cards corresponding to 448 crystals connect to one Trigger and Router Unit (TRU). The FPGA on the TRU cards receives digitized ADC samples from the 14 FEEs every 50 ns and outputs L0 and L1 trigger decisions of the PHOS detector via high speed cables to a simple external OR unit. The TRU also serves as buffer and router for energy and trigger data from the 14 FEE cards to the Readout Control Unit (RCU) [135]. For each PHOS module there are 8 embedded TRUs and four external RCUs reading out and transferring energy data to the Data Acquisition System (DAQ). Table 5.2 summarizes the different components for the PHOS readout electronics chain.

Module	Crystal Serviced	Inputs	Number Needed
Pre-amplifier	1	1	17920
FEE	32	32	560
TRU	448	14	40
RCU	896	2	20

Table 5.2: *PHOS electronic channel counts.*

5.4 The DAQ System for PHOS Beam Test

A Data Acquisition (DAQ) system, which is based on the ALICE DATE (Data Acquisition and Test Environment) [136], has been developed in 2001 to support the PHOS beam test. In this section we describe the DATE architecture, the setup of the DAQ system. A study of the performance of a PHOS prototype by using data collected by this newly developed DAQ system will be presented in the next section.

ALICE DATE architecture

The ALICE DATE system has been developed as a basis for prototyping the components of the ALICE DAQ system and for the support of the ALICE test beams. It includes a set of programs and packages such as run control, error reporting, event building and data recording, and also provides interfaces to readout and monitoring programs. It is designed to run on two different types of machines: the Local Data Concentrator (LDC) and the Global Data Concentrator (GDC). The LDC is used as a front-end processor to readout the front-end electronics, format the data fragments into (sub-)events, record or send data to a GDC, whereas the GDC performs event-building, formatting of sub-events into events and data recording. A schematic view of the DATE data-flow is depicted in Figure 5.7. Data are read out from the front-end electronics via LDCs independently and concurrently. Then various sub-events from the LDCs are collected, put together and encapsulated with a proper event structure by GDCs. Finally the full events are recorded in local disk or shipped to a central data recording service.

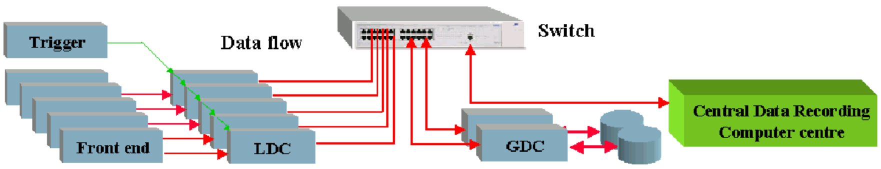

Figure 5.7: *Schematics of DATE data-flow and hardware architecture. The figure is taken from [136].*

Setup

A schematic view of the DAQ setup for PHOS beam test is shown in Figure 5.8. A VME embedded CCT processor is running as a LDC, and a computer with Linux OS, which is connected to the VME system through a fast Ethernet network, is running as a GDC. A CAMAC Branch Driver (CBD 8210) is used to drive the CAMAC branch so that front-end electronic modules[7] in the CAMAC crate can be accessed from the VME

[7]CAMAC readout modules for PHOS beam test are: trigger pattern unit, Kurchatov ADC, LeCroy 2249 ADC, LeCroy 2228 TDC.

bus. The VME crate also contains front-end electronic modules[8] and a CORBO module (CES RCB 8047) as the trigger module.

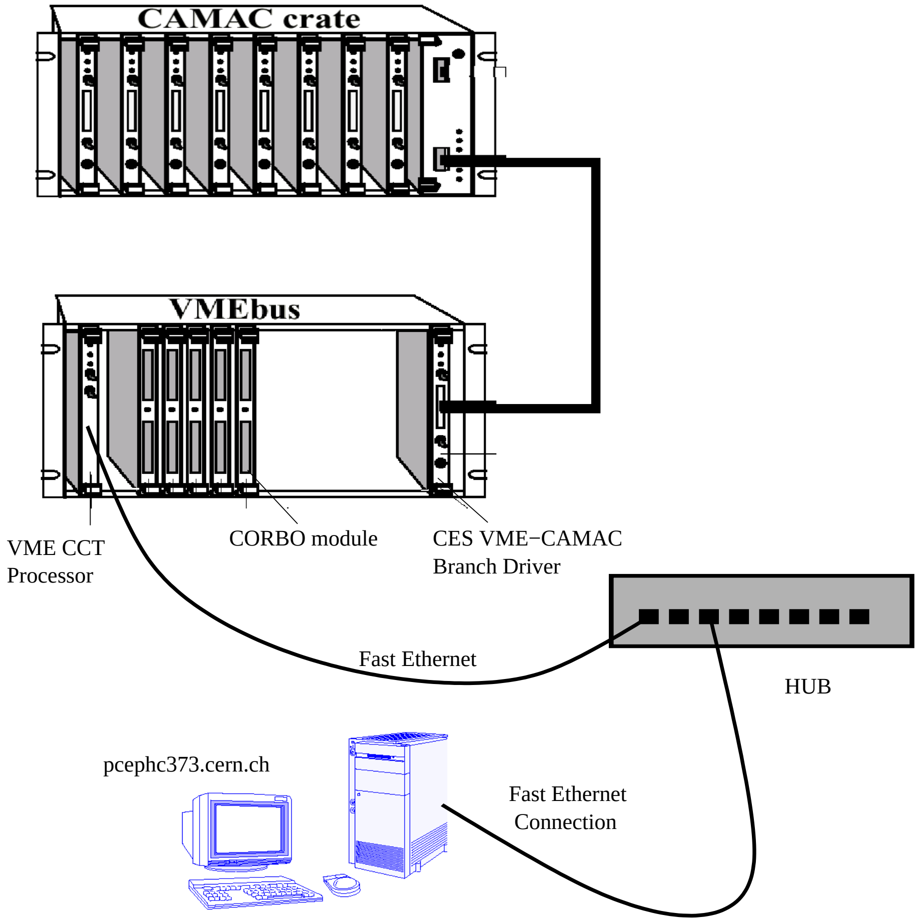

Figure 5.8: *Schematics view of the DAQ setup for PHOS beam test.*

As only one LDC is used in PHOS beam test, the trigger electronics is simply setup as shown in Figure 5.9. The first channel of CORBO is used to trigger the LDC and activate the readout program. The readout program polls the channel until a trigger arrives. The busy output then will gate off subsequent triggers until it is removed by software (see Appendix C).

Readout

As shown in Figure 5.10, the readout is performed in each LDC by a process called "readout", which waits for a trigger and then reads the front-end electronics and fills a circular buffer. Another process called "recorder" off-loads the buffer and sends the events to either a local disk file or a GDC via network.

[8]VME modules for the PHOS beam test are three CAEN VME 550 C-RAMS units and a CAEN V551B C-RAMS Sequencer to control the C-RAMS units.

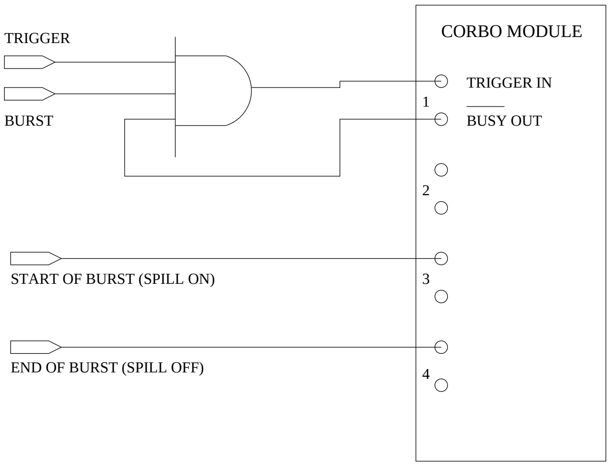

Figure 5.9: *Trigger electronics setup for PHOS beam test.*

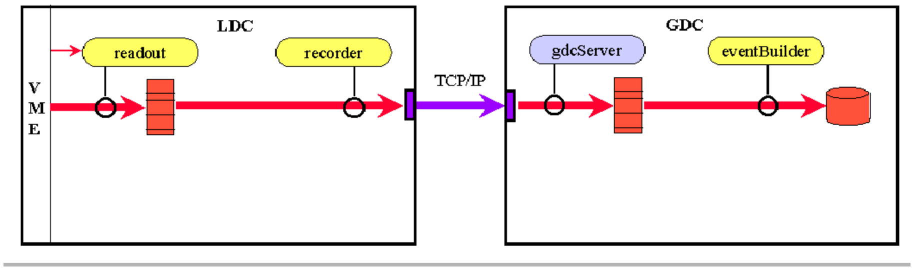

Figure 5.10: *Schematics of readout and data-flow. The figure is taken from [136]. The LDC processor is an embedded VME processor.*

In the GDC, an Internet daemon called "gdcServer" is created when the "recorder" opens the socket. The "gdcServer" gets the events from the socket and fills a circular buffer. Another process in each GDC called "eventBuilder" then off-loads the buffer and sends to a device for recording. If there are more than one LDC, the "eventBuilder" process will collect the sub-events from the various LDCs and build the full event.

It is the experimentalist's own responsibility to customize and build the experimental dependent readout process, which performs the hardware readout and inserts data into buffers. An example of readout routines for one of the front-end electronics used in the PHOS beam test is shown in Appendix C. Figure 5.11 shows the common structure of the readout program along with the main event loop.

The readout process performs in the order the following sequence of operations:

1. At each start of run, execute the Start Of Run (SOR) scripts and/or files if any, and then call the user routine *ArmHw* to initiate hardware.

2. Initiate the physics events main loop and wait for a trigger by calling the user routine *EventArrived*. The arrival of a trigger can signal a physics event or a start

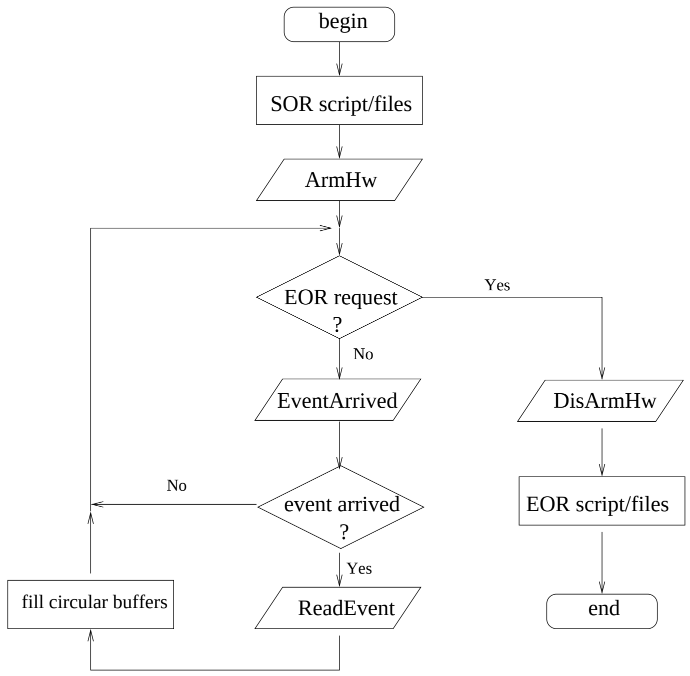

Figure 5.11: *The structure of the readout program and the event loop. The figure is taken from [136].*

of burst (SOB) or an end of burst (EOB).

3. By arrival of a trigger, the readout process fills the event header fields and the event data by calling the user routine *ReadEvent*.

4. Exit the main event loop if there is an end of run (EOR) request, e.g. the maximum number of events reached.

5. At each end of run, call the user routine *DisArmHw* to perform the hardware rundown, and then execute the End Of Run (EOR) script/files if any.

Monitoring

An on-line analysis process may request events from any data-acquisition machine by calling the monitoring library routines provided by DATE. A buffer reserved for the monitoring function is filled with the requested events by either the "readout" or the "eventBuilder" process. The architecture of the monitoring function is shown in Figure 5.12. The analysis process may run locally on the machine producing the events or on any other workstation.

An on-line monitoring program for PHOS beam test has been developed in the ROOT [137] framework during the summer of 2001. It reads events dynamically from data source and performs raw data de-coding and data analyzing for physics events according to the trigger pattern. Some results from such a monitoring program are shown in section 5.5.

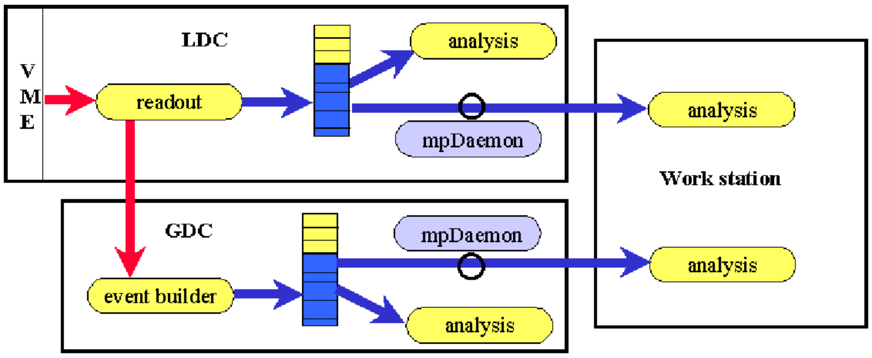

Figure 5.12: *Schematics of monitoring function. The figure is taken from [136].*

5.5 Performance of PHOS Prototype

In 2002 and 2003 CERN PS and SPS beam tests, a 16×16 matrix, 256 channel PHOS prototype was tested with an electron beam at a momentum range of 0.6-150 GeV/c. The experimental setup is shown schematically in Figure 5.13, where S_1 and S_2 are scintillators with dimension of 10 cm $\times$ 10 cm $\times$ 0.5 cm, DWC is a drift wire chamber and F is a scintillator with size of 1 cm $\times$ 1 cm $\times$ 0.5 cm. Combining signals from these scintillators and the Čerenkov counter, wide and narrow electron trigger information is delivered to the trigger pattern unit of the DATE-based DAQ system. In this section we will present some results from the beam tests in 2002 and 2003 with APDs as the photo-detectors.

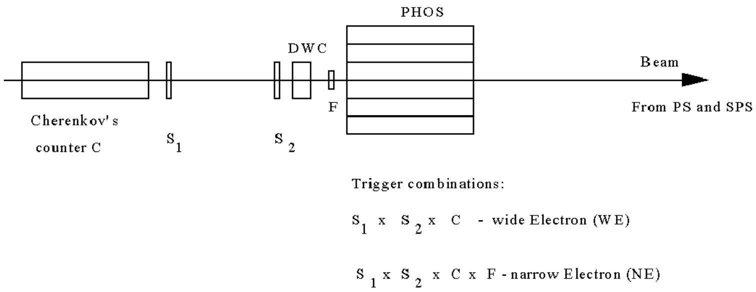

Figure 5.13: *The experimental setup for PHOS beam test.*

Measurements of the response to incoming electrons

The left panel of Figure 5.14 shows the spectrum from a single central detector of 18 cm long $PbWO_4$ crystals with response to incoming 4 GeV/c electrons with narrow electron trigger condition. In the right panel of Figure 5.14, the spectrum from the central 3×3 array of detectors is shown after pedestal subtraction and gain calibration, together with a Gaussian fit. The energy sum of 3×3 matrix is peaked at the right position and the obtained energy resolution is: $\sigma_E/E = 1.9\%$.

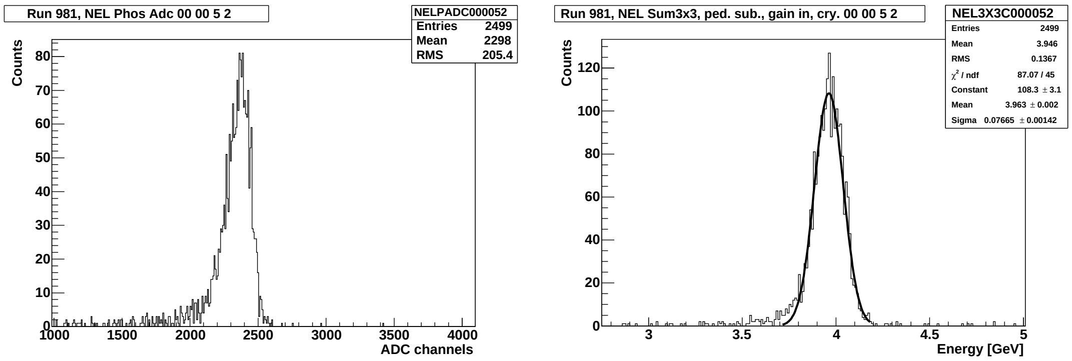

Figure 5.14: *The measured spectra from the single central detector (left) and the sum of 3×3 array (right) of 18 cm $PbWO_4$ crystals with Narrow Electron trigger at the beam momentum of 4 GeV/c.*

Figure 5.15 shows the peak positions of reconstructed electron energies from the sum of 3×3 array of detectors. The mean position of the energy peaks is obtained by fitting a Gaussian to the measured spectrum after pedestal subtraction and gain calibration as illustrated in the right panel of Figure 5.14. To guide the eye, a straight-line of $y = x$ is drawn. The data show that the deviation from the linearity curve is less than 2% in the energy range from 0.6 to 150 GeV [138].

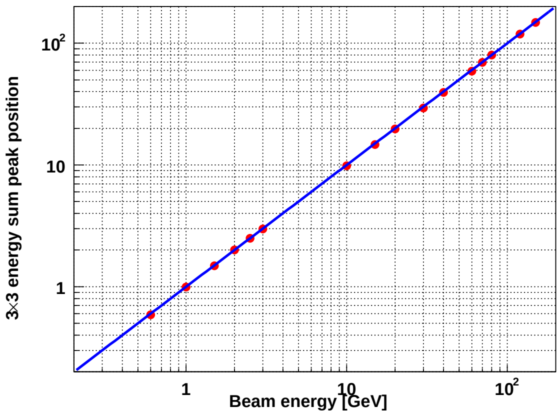

Figure 5.15: *The measured peak positions from the energy sum of a 3×3 array of detectors for different beam energies.*

Results for the energy resolution

The performance of an electromagnetic calorimeter is qualified in terms of the energy resolution, which is parameterized as

$$\frac{\sigma_E}{E} = \sqrt{\frac{a^2}{E^2} + \frac{b^2}{E} + c^2}, \tag{5.1}$$

where a represents the electronic readout noise, b represents the stochastic fluctuations in the involved physical processes, and c represents in-homogeneities in the detector and readout in addition to the energy loss and calibration errors. Here, the energy E is given in units of GeV. In the ALICE Technical Proposal [125] and the PHOS Technical Design Report [126], these parameters are required to be less than 0.03, 0.03 and 0.01, respectively.

In Figure 5.16, the mean value of the energy resolution for sixteen 3×3 subset detectors is shown as a function of beam energy measured in the 2002 and 2003 beam tests [138]. The dashed curve represents a fit to data by the Eq. 5.1 with parameters $a = 0.013\pm0.0007$ GeV, $b = 0.0358 \pm 0.002$ and $c = 0.0112 \pm 0.003$. Also shown in the figure is the PHOS requirement. The data indicate that the PHOS requirements are fulfilled with respect to the energy resolution.

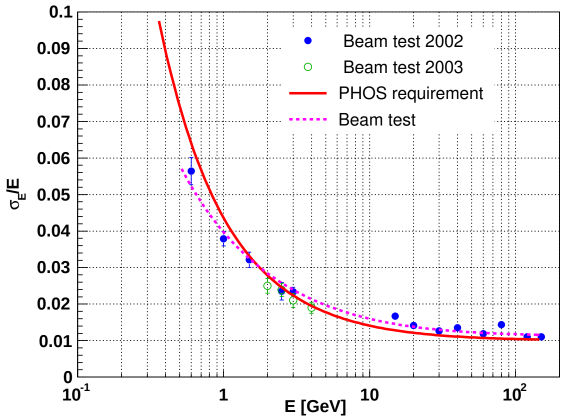

Figure 5.16: *The measured mean value of the energy resolution for sixteen 3×3 subset detectors as a function of electron beam energy in the 2002 and 2003 beam tests. The dashed line is a fit to the data with Eq. 5.1. The solid curve shows the PHOS requirement.*

Invariant mass resolution

The π^0 and η production yields will be extracted from the two-γ invariant mass spectrum, reconstructed by

$$M_{\gamma\gamma} = \sqrt{2E_1E_2(1 - \cos\phi)}, \tag{5.2}$$

where E_1 and E_2 are the energies of two photons and ϕ is the opening angle between them. The background to signal ratio depends on the mass resolution. A better mass resolution means higher statistical significance and lower systematic error for the meson yields. During 2002 and 2003 beam tests, the invariant mass resolution for the PHOS prototype has been studied at CERN PS and SPS via the reaction $\pi^- + {}^{12}C \rightarrow \gamma + \gamma + X$. A schematic view of the experimental setup is shown in Figure 5.17.

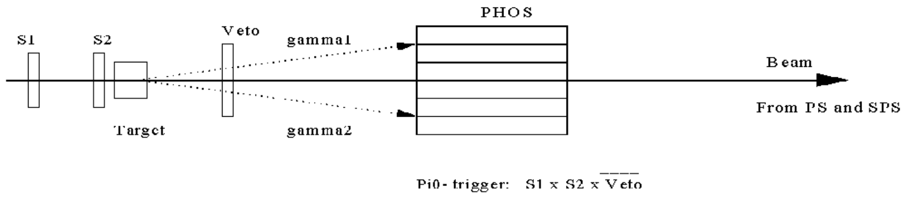

Figure 5.17: *The experimental setup for 2γ invariant mass measurements in the PHOS beam test experiment.*

Figure 5.18 shows the 2γ invariant mass spectrum measured at CERN SPS with a 70 GeV/c incoming π^- beam and the target located at a distance of 450 cm from the PHOS prototype[9]. Also shown in the figure is a Gaussian function combined with a third-order polynomial function fitted to the spectrum. The resulting resolution of π^0 is around 6%.

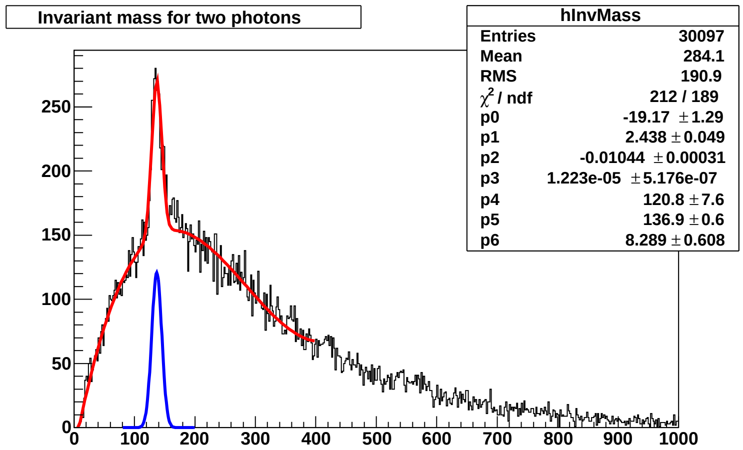

Figure 5.18: *Spectrum of two-photon invariant mass measured at CERN SPS with incoming 70 GeV/c π^- bombarding a ${}^{12}C$ target located at a distance of 450 cm away from the PHOS prototype. A π^0 peak is clearly seen. The red (grey) curve is a Gaussian combined with a third-order polynomial fitted to the spectrum. The blue (black) curve is the resulting Gaussian fit.*

[9](1)The distance from IP to PHOS in the ALICE setup is 440 cm. (2) With such a configuration π^0 with momenta greater than 3.8 GeV/c might be detected by the 256 channel PHOS prototype.

5.6 Summary

In order to optimize the PHOS detector regarding high p_T physics, an extensive research and development program has been carried out during the past several years. A decision has been made to use APDs instead of PIN-diodes as photo-detectors. A modification of the pre-amplifier was made to increase the linear dynamic range to match the requirement for measuring high p_T events. A feasibility study has been carried out to find out whether and how PHOS can deliver a trigger to ALICE followed by the conceptional design of the PHOS front-end electronics. The requirements of generating a L0 trigger in less than 800 ns and covering a large energy dynamic range have been realized by the newly designed front-end electronics without deteriorating the resolution for low energy data. Furthermore a DATE-based data acquisition system has been developed and set up for PHOS beam tests, with user-friendly interface and on-line monitoring program. The beam test studies of the 256 channel PHOS prototype, which incorporated the newly developed front-end electronics and APDs, have shown that the PHOS prototype has already met the PHOS requirement with respect to the energy resolution.

Chapter 6

Conclusion

The nuclear medium effect on high p_T particle production has been studied at mid-rapidity and pseudo-rapidity $\eta = 2.2$ in Au+Au and d+Au collisions at $\sqrt{s_{NN}} = 200$ GeV. Based on the present analysis, the high p_T yields for charged pions are more strongly suppressed than those for inclusive charged hadrons at both mid-rapidity and forward rapidity in central Au+Au collisions. The degree of high p_T suppression observed at $\eta = 2.2$ is similar to or even stronger than that at mid-rapidity. Compared to the observed enhancement of the relative inclusive charged hadron yields at mid-rapidity in d+Au collisions, the suppression of high p_T charged hadron yields in central Au+Au collisions can be attributed to the final state nuclear medium effects. The persistence of the suppression to $\eta = 2.2$ suggests that the dense partonic medium which causes such a suppression might also be formed in the forward region. However, a suppression of high p_T π^- yields at $\eta = 2.2$ has also been observed in central d+Au collisions and R_{dAu} decreases with centrality. This is qualitatively consistent with the predictions of the CGC formalism, indicating that a fraction of the R_{AuAu} suppression at $\eta = 2.2$ should be attributed to initial state effects.

The $\bar{p}/\pi^-$ (also p/π^+) ratios have been measured up to $p_T \sim 3$ GeV/c at both mid-rapidity and $\eta = 2.2$ in 0-10% central Au+Au collisions. The data at mid-rapidity can be well reproduced by a parton recombination model with a collective flow velocity of $0.5c$. A smaller flow velocity is required to account for the data at forward rapidity. The particle composition is further studied in terms of p/h^+ ($\bar{p}/h^-$) ratios at mid-rapidity and π^-/h^- ratios at $\eta = 2.2$ in minimum-bias $p+p$, central d+Au and central Au+Au collisions. At mid-rapidity the p/h^+ ($\bar{p}/h^-$) ratio at intermediate p_T in central Au+Au collisions is found to be about a factor of 2 higher than that from d+Au and $p+p$ collisions, while at $\eta = 2.2$ the π^-/h^- ratio in central Au+Au collisions is around a factor of 1.5 lower than that from d+Au and $p+p$ collisions. All in all, these observations indicate that a dense strongly interacting partonic medium with a strong collective flow is formed in central Au+Au collisions which results in the strong suppression of high p_T charged pion yields and boosts the protons to higher transverse momenta. However, it is still a long way to go to fully understand such a strongly interacting QCD matter with respect to its formation, evolution and transition to hadronic matter.

The LHC, which is scheduled to operate in 2007, will provide a qualitatively new environment with ideal conditions to explore the properties of the QGP. The higher energy and high luminosity will improve the access to hard probes sensitive to the earliest stages of the collision and allow the study of the parton energy loss and the effective jet fragmentation function via e.g. γ-tagged jets up to $p_T \sim 100$ GeV/c. To address high p_T observables, an extensive research and development program for the PHOS detector has been carried out during the past years. Studies show that PHOS can provide a trigger to ALICE within 800 ns and cover a large energy dynamic range by the newly designed front-end electronics without degradation of the resolution for low energy data. A 256-channel PHOS prototype with APDs as photo-detectors has been tested in the past years. The results indicate that the performance of the PHOS prototype has met the design goals. A final PHOS prototype, which will incorporate the newest developed front-end electronics and the full readout chain including FEE, TRU cards and RCU modified from TPC-RCU, will be built and tested in the near future.

References

[1] S. Bethke, hep-ex/0211012.

[2] F. Karsch, Nucl. Phys. **A698** (2002) 199.

[3] Z. Fodor and S. D. Katz, JHEP **03** (2002) 014.

[4] P. Braun-Munzinger *et al.*, Phys. Lett. **B465** (1999) 15.

[5] J. Cleymans and K. Redlich, Phys. Rev. Lett. **81** (1998) 5284.

[6] R. Stock, Phys. Lett. **B456** (1999) 277.

[7] C. W. deJager, H. deVries and C. deVries, Atomic Data and Nuclear Data Table **14** (1974) 485.

[8] R. J. Glauber and G. Matthiae, Nucl. Phys. **B21** (1970) 135.

[9] BRAHMS Collaboration, I. G. Bearden, *et al.*, Phys. Rev. Lett. **88** (2002) 202301.

[10] E917 Collaboration, B. B. Back *et al.*, Phys. Rev. Lett. **86** (2001) 1970.

[11] E802 Collaboration, L. Ahle *et al.*, Phys. Rev. **C60** (1999) 064901.

[12] E877 Collaboration, J. Barette *et al.*, Phys. Rev. **C62** (2000) 024901.

[13] H. Appelshäuser *et al.*, Phys. Rev. Lett. **82** (1999) 2471.

[14] P. H. L. Christiansen, Ph.D. Thesis, University of Copenhagen, 2003.

[15] J. D. Bjorken, Phys. Rev. **D27** (1983) 140.

[16] S. A. Bass, M. Gyulassy, H. Stocker and W. Greiner, J. Phys. **G25** (1999) R1.

[17] NA50 Collaboration, M. C. Abreu *et al.*, Phys. Lett. **B477** (2000) 28.

[18] R. Pisarski, Phys. Lett. **B110** (1982) 155.

[19] V. Bernard *et al.*, Phys. Lett. **B227** (1989) 465.

[20] G. E. Brown *et al.*, Phys. Rev. **C43** (1991) 1881.

[21] CERES Collaboration, G. Agakichiev *et al.*, Phys. Rev. Lett. **75** (1995) 1272; Phys. Lett. **B422** (1998) 405; B. Lenkeit *et al.*, Nucl. Phys. **A661** (1999) 23c.

[22] G. Q. Li, C. M. Ko and G. E. Brown, Phys. Rev. Lett. **75** (1995) 4007.

[23] R. Rapp, G. Chanfray and J. Wambach, Nucl. Phys. **A617** (1997) 472.

[24] H. Sorge, Phys. Rev. Lett. **82** (1999) 2048.

[25] STAR Collaboration, J. Adams *et al.*, Phys. Rev. Lett. **92** (2004) 062301; Phys. Rev. Lett. **92** (2004) 052302; C. Adler *et al.*, Phys. Rev. **C66** (2002) 034904.

[26] PHENIX Collaboration, S. S. Adler *et al.*, Phys. Rev. Lett. **91** (2003) 182301; Phys. Rev. Lett. **91** (2003) 072301.

[27] P. F. Kolb, P. Huovinen, U. W. Heinz and H. Heiselberg, Phys. Lett. **B500** (2001) 232; P. Huovinen, P. F. Kolb, U. W. Heinz, P. V. Ruuskanen and S. A. Voloshin, Phys. Lett. **B503** (2001) 58; P. F. Kolb, U. W. Heinz, P. Huovinen, K. J. Eskola and K. Tuominen, Nucl. Phys. **A696** (2001) 197; P. Huovinen, nucl-th/0305064; P. F. Kolb and U. W. Heinz, nucl-th/0305084.

[28] T. Hatsuda, Nucl. Phys. **A544** (1992) 27c.

[29] W. Weise, Nucl. Phys. **A610** (1996) 35c.

[30] J. Rafelski, J. Letessier and A. Tounsi, Acta Phys. Pol. **B27** (1996) 1037.

[31] L. Sandor (for NA57 Collaboration), Proceedings of 7th International Conference on Strangeness in Quark Matter, March 12-17, 2003, Atlantic Beach, North Carolina, USA, to be published in J. Phys. G.

[32] J. D. Bjorken, Fermilab-Pub-82/59-THY (1982).

[33] M. Gyulassy and X. N. Wang, Nucl. Phys. **B420** (1994) 583.

[34] The CMS (Compact Muon Solenoid) experiment. http://cmsinfo.cern.ch/

[35] The ATLAS (A Toroidal LHC ApparatuS) experiment. http://pdg.lbl.gov/atlas/atlas.html

[36] The LHCb (Large Hadron Collider Beauty) experiment. http://lhcb.cern.ch

[37] The TOTEM experiment. http://totem.web.cern.ch/Totem/

[38] The ALICE (A Large Ion Collider Experiment) experiment. http://alice.web.cern.ch/Alice/AliceNew/

[39] C. Albajar *et al.*, Nucl. Phys. **B335** (1990) 261.

[40] PHENIX Collaboration, S. S. Adler *et al.*, Phys. Rev. Lett. **91** (2003) 241803.

[41] J. D. Bjorken, Phys. Rev. **179** (1969) 1547.

[42] A. D. Martin, R. G. Roberts, W. J. Stirling and R. S. Thorne, Eur. Phys. J. **C23** (2002) 73.

[43] J. Pumplin *et al.*, JHEP **12** (2002) 0207.

[44] M. Glueck, E. Reya, M. Stratmann and W. Vogelsang, Phys. Rev. **D63** (2001) 094005.

[45] L. N. Lipatov, Sov. J. Nucl. Phys. **20** (1975) 95; V. N. Gribov and L. N. Lipatov, Sov. J. Nucl. Phys. **15** (1972) 438; G. Altarelli and G. Parisi, Nucl. Phys. **B126** (1977) 298; Yu. L. Dokshitzer, Sov. Phys. JETP **46** (1977) 641.

[46] B. A. Kniehl, G. Kramer and B. Pötter, Nucl. Phys. **B582** (2000) 514.

[47] J. Binnewies, B. A. Kniehl and G. Kramer, Phys. Rev. **D52** (1995) 4947.

[48] S. Kretzer, Phys. Rev. **D62** (2000) 054001.

[49] L. Bourhis, M. Fontannaz, J. P. Guillet and M. Werlen, Eur. Phys. J. **C19** (2001) 89.

[50] J. C. Collions *et al.*, in Perturbative Quantum Chromodynamics, ed. A. H. Mueller, Adv. Ser. Direct. High Energy Phys. **5** (1988) 1.

[51] B. Alper *et al.*, Nucl. Phys. **B100** (1975) 237.

[52] F. Abe *et al.*, Phys. Rev. Lett. **61** (1988) 1819.

[53] W. M. Geist *et al.*, Phys. Rep. **197** (1990) 263.

[54] J. J. Aubert *et al.*, Phys. Lett. **B123** (1982) 275.

[55] T. Sloan, G. Smadja and R. Voss, Phys. Rep. **162** (1988) 45; L. Frankfurt and M. Strikman, Phys. Rep. **160** (1988) 235; M. Arneodo, Phys. Rep. **240** (1991) 301.

[56] M. Arneodo, Nucl. Phys. **B441** (1995) 12.

[57] J. W. Cronin *et al.*, Phys. Rev. **D11** (1975) 3105.

[58] D. Antreasyan *et al.*, Phys. Rev. **D19** (1979) 764.

[59] D. A. Garbutt *et al.*, Phys. Lett. **B67** (1977) 355.

[60] D. Chaney *et al.*, Phys. Rev. **D19** (1979) 3210.

[61] H. J. Frisch *et al.*, Phys. Rev. **D27** (1983) 1001.

[62] M. M. Aggarwal *et al.*, Phys. Rev. Lett. **81** (1998) 4087.

[63] Y. Chen, Ph.D Thesis, University of California, 2003.

[64] A. Mueller and J. Qiu, Nucl. Phys. **B268** (1986) 427.

[65] K. J. Eskola, V. J. Kolhinen and C. A. Salgado, Eur. Phys. J. **C9** (1999) 61.

[66] J. Jalilian-Marian, A. Kovner, L. McLerran, H. Weigert, Phys. Rev. **D55** (1997) 5414.

[67] K. Golec-Biernat and M. Wüsthoff, Phys. Rev. **D59** (1998) 014017.

[68] E. Iancu, A. Leonidov and L. McLerran, Nucl. Phys. **A692** (2001) 583.

[69] X. N. Wang and M. Gyulassy, Phys. Rev. **D44** (1991) 3501.

[70] S. Y. Li and X. N. Wang, Phys. Lett. **B527** (2002) 85.

[71] M. Gyulassy and M. Plümer, Phys. Lett. **B243** (1990) 432.

[72] R. Baier *et al.*, Phys. Lett. **B345** (1995) 277.

[73] M. H. Thoma, Quark-Gluon Plasma 2, ed. R. C. Hwa, World Sci., Singapore (1995), p.51.

[74] A. Casher, H. Neuberger and S. Nussinov, Phys. Rev. **D20** (1979) 179.

[75] L. D. Landau and I. Y. Pomeranchuk, Dokl. Akad. Nauk SSSR **92:535** (1953) 735; A. B. Migdal, Phys. Rev. **103** (1956) 1811.

[76] R. Baier, Nucl. Phys. **A715** (2003) 209c.

[77] M. Gyulassy, P. Levai and I. Vitev, Phys. Rev. Lett. **85** (2000) 5535.

[78] E. Wang and X. N. Wang, Phys. Rev. Lett. **87** (2001) 142301.

[79] S. Jeon, J. Jalilian-Marian and I. Sarcevic, Phys. Lett. **B562** 45.

[80] A. Capella, U. Sukhatme, C. I. Tan and J. Tran Thanh Van, Phys. Rep. **236** (1994) 225.

[81] B. Andersson, G. Gustafson and C. Peterson, Phys. Lett. **B69** (1977) 221; B. Andersson, G. Gustafson, G. Ingelman and T. Sjöstrand, Phys. Rep. **97** (1983) 31.

[82] K. P. Das and R. C. Hwa, Phys. Lett. **B68** (1977) 459; R. C. Hwa, Phys. Rev. **D22** (1980) 1593.

[83] I. Vitev and M. Gyulassy, Phys. Rev. **C65** (2002) 041902(R).

[84] R. C. Hwa and C. B. Yang, Phys. Rev. **C66** (2002) 025205; R. C. Hwa and C. B. Yang, Phys. Rev. **C67** (2003) 034902.

[85] V. Greco, C. M. Ko and P. Lévai, Phys. Rev. Lett. **90** (2003) 202302.

[86] Y. Zhang *et al.*, Phys. Rev. **C65** (2002) 034903.

[87] S. A. Voloshin, Nucl. Phys. **A715** (2003) 379.

[88] C. Adler *et al.*, Phys. Rev. Lett. **90** (2003) 082302.

[89] X. N. Wang, Z. Huang and I. Sarcevic, Phys. Rev. Lett. **77** (1996) 231.

[90] G. C. Rossi and G. Veneziano, Nucl. Phys. **B123** (1977) 507; Phys. Rep. **63** (1980) 153.

[91] D. Kharzeev, Phys. Lett. **B378** (1996) 238.

[92] S. E. Vance, M. Gyulassy and X. N. Wang, Phys. Lett. **B443** (1998) 45; S. E. Vance and M. Gyulassy, Phys. Rev. Lett. **83** (1999) 1735.

[93] BRAHMS Collaboration, M. Adamczyk *et al.*, Nucl. Instr. Meth. **A499** (2003) 437.

[94] H. Ito, Ph.D. Thesis, University of Kansas, 2002.

[95] D. Ouerdane, Ph.D. Thesis, University of Copenhagen, 2003.

[96] R. Karabowicz, Master Thesis, University of Krakow, 2002.

[97] BRAHMS Collaboration, Conceptual Design Report, October 1994.

[98] Application Software Group, CERN Computing and Networks Division. GEANT — Detector Description and Simulation Tool, 1993. *http://consult.cern.ch/writeup/geant/*

[99] T. M. Larsen, Master Thesis, University of Oslo, 2003.

[100] P. Staszel, BRAHMS analysis notes 27, 29, 34 and 38.

[101] PHENIX Collaboration, K. Adcox *et al.*, Phys. Rev. Lett. **87** (2002) 242301.

[102] BRAHMS Collaboration, I. Arsene *et al.*, Phys. Rev. Lett. **91** (2003) 072305.

[103] PHENIX Collaboration, K. Adcox *et al.*, Phys. Rev. Lett. **88** (2002) 022301; PHENIX Collaboration, S. S. Adler *et al.*, Phys. Rev. Lett. **91** (2003) 072301.

[104] STAR Collaboration, J. Adams *et al.*, Phys. Rev. Lett. **91** (2003) 072304.

[105] PHOBOS Collaboration, B. B. Back *et al.*, Phys. Rev. Lett. **91** (2003) 072302.

[106] STAR Collaboration, J. Adams *et al.*, nucl-ex/030912.

[107] J. Jia, Ph. D. Thesis, State University of New York at Stony Brook, 2003.

[108] BRAHMS Collaboration, I. Arsene *et al.*, nucl-ex/0403005.

[109] DELPHI Collaboration, P. Abreu *et al.*, Eur. Phys. J. **C17** (2000) 207.

[110] F. Arleo, JHEP **11** (2002) 044.

[111] I. Vitev and M. Gyulassy, Phys. Rev. Lett. **89** (2002) 252301.

[112] X. N. Wang, Phys. Lett. **B579** (2004) 299.

[113] PHENIX Collaboration, S. S. Adler *et al.*, Phys. Rev. **C69** (2004) 034909.

[114] D. Kharzeev, E. Levin and L. McLerran, Phys. Lett. **B561** (2003) 93.

[115] D. Kharzeev and M. Nardi, Phys. Lett. **B507** (2001) 121.

[116] D. Kharzeev, Nucl. Phys. **A715** (2003) 35.

[117] R. Baier, A. H. Mueller, D. Schiff and D. T. Son, Phys. Lett. **B539** (2002) 494.

[118] D. Kharzeev, Y. V. Kovchegov and K. Tuchin, Phys. Rev. **D68** (2003) 094013.

[119] G. G. Barnaföldi, G. Papp, P. Lévai and G. Fai, Quark Matter 2004, nucl-th/0404012.

[120] D. Kharzeev, RIKEN-BNL Workshop on high p_T physics at RHIC, 2-6, December, 2003.

[121] PHENIX Collaboration, S. S. Adler *et al.*, Phys. Rev. **C69** (2004) 034910.

[122] PHOBOS Collaboration, B. B. Back *et al.*, Phys. Lett. **B578** (2004) 297.

[123] STAR Collaboration, J. Adams *et al.*, Phys. Rev. Lett. **91** (2003) 172302.

[124] ALICE Collaboration, ALICE Physics Performance Report, CERN/LHCC 2003-049, 7 November 2003.

[125] ALICE Collaboration, ALICE Technical Proposal, CERN/LHCC/95-71(1995).

[126] ALICE Collaboration, PHOS Technical Design Report, CERN/LHCC 99-4, 5 March 1999.

[127] T. Sjöstrand *et al.*, Comp. Phys. Commun. **135** (2001) 238.

[128] ALICE Off-line Project. *http://Alisoft.cern.ch/offline/*

[129] A. M. Blik *et al.*, Instruments and Experimental Technics **44** (2001) 339.

[130] M. Yu. Bogolyubsky *et al.*, Instruments and Experimental Technics, **45** (2002) 327.

[131] H. Beker *et al.*, CERN/LHCC/96-39, p. 170.

[132] H. Müller *et al.*, Nucl. Instr. Meth. **A518** (2004) 525.

[133] H. Müller *et al.*, PHOS Electronics Specifications, ALICE Technical Note, 22 Octobor, 2003.

[134] B. T. Skaali, LHCC ALICE Comprehensive Review IV, PHOS electronics, March 22-23, 2004.

[135] R. Esteve-Bosch *et al.*, Readout control unit of the front end electronics for the ALICE time projection chamber, Proceedings of the 8th Workshop on Electronics for LHC experiments, September 2002, Colmar, France.

[136] CERN ALICE DAQ group, ALICE DATE User's Guide, ALICE Internal Note 2000-31, January 2000.

[137] R. Brun and F. Rademakers, ROOT: An Object-Oriented Data Analysis Framework. *http://root.cern.ch*

[138] M. Ippolitov (for the ALICE/PHOS Collaboration), Talk given in the 6th International Conference on Calorimetry in High Energy Physics, March 29, 2004, Perugia.

Appendix A

The BRAHMS Collaboration

I. G. Bearden[7], D. Beavis[1], C. Besliu[10], Y. Blyakhman[6], B. Budick[6], H. Bøggild[7], C. Chasman[1], C. H. Christensen[7], P. Christiansen[7], J. Cibor[3], R. Debbe[1], E. Enger[12], J. J. Gaardhøje[7], M. Germinario[7], K. Hagel[8], O. Hansen[7], A. Holm[7], A. K. Holme[12], H. Ito[11], E. Jakobsen[7], A. Jipa[10], F. Jundt[2], J. I. Jørdre[9], C. E. Jørgensen[7], R. Karabowicz[4], T. Keutgen[8], E. J. Kim[1], T. Kozik[4], T. M. Larsen[12], J. H. Lee[1], Y. K. Lee[5], G. Løvhøiden[12], Z. Majka[4], A. Makeev[8], B. McBreen[1], M. Mikelsen[12], M. Murray[8], J. Natowitz[8], B. S. Nielsen[7], J. Norris[11], K. Olchanski[1], J. Olness[1], D. Ouerdane[7], R. Płaneta[4], F. Rami[2], C. Ristea[10], D. Röhrich[9], B. H. Samset[12], D. Sandberg[7], S. J. Sanders[11], R. A. Scheetz[1], P. Staszel[7], T. S. Tveter[12], F. Videbæk[1], R. Wada[8], A. Wieloch[4], Z. Yin[9], I. S. Zgura[10]

[1] Brookhaven National Laboratory, Upton, New York 11973, USA
[2] Institut de Recherches Subatomiques and Université Louis Pasteur, Strasbourg, France
[3] Institute of Nuclear Physics, Krakow, Poland
[4] Smoluchkowski Inst. of Physics, Jagiellonian University, Krakow, Poland
[5] Johns Hopkins University, Baltimore 21218, USA
[6] New York University, New York 10003, USA
[7] Niels Bohr Institute, Blegdamsvej 17, University of Copenhagen, Copenhagen 2100, Denmark
[8] Texas A&M University, College Station, Texas, 17843, USA
[9] University of Bergen, Department of Physics, Bergen, Norway
[10] University of Bucharest, Romania
[11] University of Kansas, Lawerence, Kansas 66049, USA
[12] University of Oslo, Department of Physics, Oslo, Norway

Appendix B

Kinematics

In this appendix, kinematics relevant to relativistic heavy ion physics is reviewed. Throughout this section units are used in which $\hbar = c = 1$. The following conversions are useful: $\hbar c = 197.3$ MeV fm, $(\hbar c)^2 = 0.3894$ (GeV)^2 mb.

B.1 Lorentz Transformations

The energy E and 3-momentum $\mathbf{p}$ of a particle of mass m form a 4-vector $(E, \mathbf{p})$ and $E^2 - |\mathbf{p}|^2 = m^2$. The velocity of the particle is $\beta = \mathbf{p}/E$. The energy and momentum $(E', \mathbf{p}')$ viewed from a frame moving with a velocity β_f are given by

$$\begin{pmatrix} E' \\ p'_{||} \end{pmatrix} = \begin{pmatrix} \gamma_f & -\gamma_f \beta_f \\ -\gamma_f \beta_f & \gamma_f \end{pmatrix} \begin{pmatrix} E \\ p_{||} \end{pmatrix}, \tag{B.1}$$

$$p'_T = p_T \tag{B.2}$$

where $\gamma_f = 1/\sqrt{1-\beta_f^2}$ and $p_T(p_{||})$ is the component of $\mathbf{p}$ perpendicular (parallel) to β_f. Other 4-vectors, such as the space-time coordinates of the events transform in the same manner. The scalar product of two 4-momenta $p_1 \cdot p_2 = E_1 E_2 - \mathbf{p}_1 \cdot \mathbf{p}_2$ is invariant.

B.2 Kinematic Variables

In two body collisions one usually chooses the beam direction for the z-axis. As an example, Figure B.1 shows the coordinate systems used in the BRAHMS experiment where the beam axis coincides with z-axis in global coordinate system. For the purpose of present single-particle differential multiplicities, it is convenient to use Lorentz invariant variables.

Transverse Momentum and Transverse Mass

The momentum component p_x and p_y are unchanged by a boost along the z-axis, so the transverse momentum p_T and transverse mass m_T, which are defined as

$$p_T = \sqrt{p_x^2 + p_y^2}, \tag{B.3}$$

$$m_T = \sqrt{m^2 + p_T^2}, \tag{B.4}$$

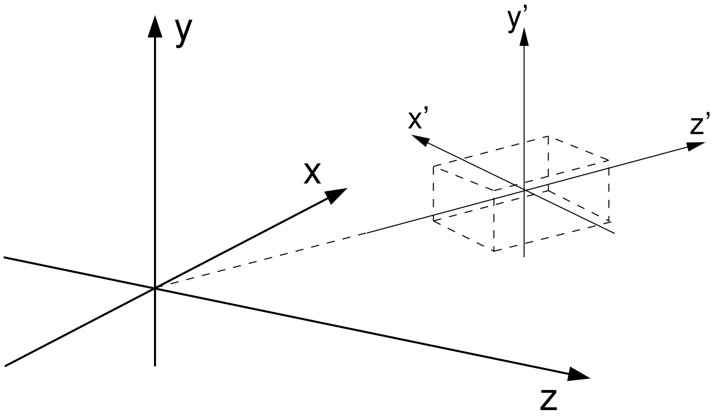

Figure B.1: *The BRAHMS global and local coordinate system. In the global coordinate system (denoted x, y, z) the nominal IP is located at $(0, 0, 0)$ and the z-axis follows the beam-line. The x-axis and y-axis point toward the MRS and the roof, respectively. For each detector a local coordinate system is defined with the z'-axis pointing away from the nominal IP and the y'-axis parallel to the y-axis.*

are boost invariant, m is the rest mass of the particle.

Rapidity

The most commonly used longitudinal variable is the rapidity y,

$$y = \frac{1}{2}\ln\left(\frac{E+p_z}{E-p_z}\right) \tag{B.5}$$

$$= \ln\left(\frac{E+p_z}{m_T}\right), \tag{B.6}$$

which is additive under Lorentz transformations along the z-axis. This means that the difference in rapidity dy and also the shape of the rapidity density distribution dN/dy are invariant under Lorentz transformations along the z-axis. The energy and the longitudinal momentum can be expressed in y as

$$p_z = m_T \sinh y \tag{B.7}$$

$$E = m_T \cosh y. \tag{B.8}$$

Then the longitudinal component of the velocity of a particle of rapidity y can be obtained by dividing the two equation above as

$$\beta_z = \tanh y. \tag{B.9}$$

Since rapidity is additive, under a boost in the z-direction to a frame with velocity β_f, the rapidity y' in the new frame is then:

$$y' = y - \tanh^{-1}\beta_f. \tag{B.10}$$

Pseudo-rapidity

In case the mass and momentum of the particle are unknown, it is convenient to use pseudo-rapidity,

$$\eta = -\ln(\tan(\theta/2)), \tag{B.11}$$

where θ is the polar angle between the particle momentum and the beam axis. In terms of momentum, the pseudo-rapidity can be written as

$$\eta = \frac{1}{2}\ln\left(\frac{|\mathbf{p}| + p_z}{|\mathbf{p}| - p_z}\right). \tag{B.12}$$

If $|\mathbf{p}| \gg m$, then $\eta \sim y$.

Jacobian Effect

One can express the pseudo-rapidity η in terms of the rapidity by using Eq. B.7 and B.8 as

$$\eta = \frac{1}{2}\ln\left(\frac{\sqrt{m_T^2\cosh^2 y - m^2} + m_T\sinh y}{\sqrt{m_T^2\cosh^2 y - m^2} - m_T\sinh y}\right). \tag{B.13}$$

If particles have a distribution $\frac{d^2N}{dydp_T}$ in terms of rapidity, then the distribution in pseudo-rapidity is

$$\frac{d^2N}{d\eta dp_T} = \sqrt{1 - \frac{m^2}{(p_T^2 + m^2)\cosh^2 y}}\frac{d^2N}{dydp_T}. \tag{B.14}$$

The above expression is a Jacobian transformation whose value depends on the rapidity, mass and p_T of the particle. The Jacobian is largest at mid-rapidity, and for a given rapidity it is larger for higher mass and lower p_T particles.

Appendix C

An Example of a Readout Program for PHOS Beam Test

Readout program has been written for the PHOS beam test. Kurchatov ADC, LeCroy 2249 ADC, LeCroy 2228 TDC and CAEN VME 550 C-RAM have been implemented as readout equipment, while CORBO as a trigger module. This appendix shows an example for a readout of Kurchatov ADC. In order to save space, some log information and comments have been omitted.

```
#include <stdlib.h>
#include <stdio.h>
#ifdef SunOS
#include <unistd.h>
#endif
#include ‘‘event.h’’
#include ‘‘equipment.h’’
#include ‘‘corboDef.h’’
#include ‘‘rcShm.h’’
#include ‘‘readList_detectors.h’’

/* Definition of function for CAMAC */
#define BCNAF(B,C,N,A,F) (((B)<<19)|((C)<<16)|((N)<<11)|((A)<<7)|((F)<<2)|0x2)
#define getm16 (unsigned short)*(unsigned short *)
#define putm16 *(unsigned short *)

extern int readList_error;

/******************** Function prototype definition **********/
void ArmVmeWindow( char *);
void DisArmVmeWindow( char *);
void ReadEventVmeWindow( char *, struct eventHeaderStruct *);

void ArmCorbo( char *);
void DisArmCorbo( char *);
void ReadEventCorbo( char *, struct eventHeaderStruct *);
int EventArrivedCorbo( char *);

void ArmCBD( char *);
void DisArmCBD( char *);
void ReadEventCBD( char *, struct eventHeaderStruct *);

void ArmKurchatovADC( char *);
void DisArmKurchatovADC( char *);
int ReadEventKurchatovADC( char *, struct eventHeaderStruct *,
                           struct equipmentHeaderStruct *, int *);

/************************** VmeWindow *************************/
unsigned long32 *vmeWinAddr;
```

```
unsigned long32 vmeWinOffset;
unsigned long32* MapVME(unsigned long32 vme_addr, unsigned long32 size);
void* UnmapVME();
typedef struct {
  unsigned long32 *vmeWinOffsetPtr;
  unsigned long32 *vmeWinSizePtr;
} VmeWindowParType;

void ArmVmeWindow( char *parPtr) {
  VmeWindowParType *vmePar = (VmeWindowParType *)parPtr;
  vmeWinOffset = *vmePar->vmeWinOffsetPtr;
  vmeWinAddr = (unsigned long32 *)MapVME( *vmePar->vmeWinOffsetPtr,
                                          *vmePar->vmeWinSizePtr);
}

void DisArmVmeWindow( char *parPtr) {
  UnmapVME();
}

void ReadEventVmeWindow( char *parPtr,
                         struct eventHeaderStruct *header_ptr){}

/************************** Corbo *************************/
/* Define hardware registers */
unsigned short *regPtrShortCLEAR1;
unsigned short *regPtrShortCLEAR3;
unsigned short *regPtrShortCLEAR4;
unsigned short *regPtrShortCSR1  ;
unsigned short *regPtrShortCSR3  ;
unsigned short *regPtrShortCSR4  ;
unsigned short *regPtrShortCNT1A  ;
unsigned short *regPtrShortCNT2A  ;
unsigned short *regPtrShortCNT1B  ;
unsigned short *regPtrShortCNT2B  ;

unsigned int corboBaseAddr;
unsigned int eventArrivedFlag;
unsigned int sobArrivedFlag;
unsigned int eobArrivedFlag;
int burstCount;
int eventsInBurstCount;
typedef struct {
  unsigned int *vmeBaseAddressPtr;
} CorboParType;

void ArmCorbo( char *parPtr) {
    register unsigned char *regPtrChar;
    register unsigned short *regPtrShort;
    CorboParType *corboPar = (CorboParType *)parPtr;

    corboBaseAddr=(unsigned int)vmeWinAddr +
      *corboPar->vmeBaseAddressPtr - (unsigned int)vmeWinOffset;

    /* Initialize pointers */
    regPtrShortCLEAR1  = (unsigned short *)(corboBaseAddr + CORBO_CLEAR1) ;
    regPtrShortCLEAR3  = (unsigned short *)(corboBaseAddr + CORBO_CLEAR3) ;
    regPtrShortCLEAR4  = (unsigned short *)(corboBaseAddr + CORBO_CLEAR4) ;
    regPtrShortCSR1    = (unsigned short *)(corboBaseAddr + CORBO_CSR1)   ;
    regPtrShortCSR3    = (unsigned short *)(corboBaseAddr + CORBO_CSR3)   ;
    regPtrShortCSR4    = (unsigned short *)(corboBaseAddr + CORBO_CSR4)   ;
    regPtrShortCNT1A   = (unsigned short *)(corboBaseAddr + CORBO_CNT1)   ;
    regPtrShortCNT2A   = (unsigned short *)(corboBaseAddr + CORBO_CNT2)   ;
    regPtrShortCNT1B   = regPtrShortCNT1A + 1 ;
    regPtrShortCNT2B   = regPtrShortCNT2A + 1 ;

    /* Channel 1 initialization.
    Input=trigger, output=busy,
    event counter=trigger number (events on this LDC) */
    regPtrShort  = (unsigned short *)(corboBaseAddr + CORBO_CSR1) ;
```

```
    *regPtrShort = CHANNELENABLE | BUSYLATCHED | INPUTINTERNAL |
      LOCALBUSYOUT | COUNTBUSY;
    regPtrChar  = (unsigned char *)(corboBaseAddr + CORBO_BIM1 + OFST_CR0) ;
    *regPtrChar = 0; /* Disable event interrupt */
    regPtrChar  = (unsigned char *)(corboBaseAddr + CORBO_BIM1 + OFST_VR0) ;
    *regPtrChar = 0; /* Clear event vector */
    regPtrChar  = (unsigned char *)(corboBaseAddr + CORBO_BIM2 + OFST_CR0) ;
    *regPtrChar = 0; /* Disable time-out interrupt */
    regPtrChar  = (unsigned char *)(corboBaseAddr + CORBO_BIM2 + OFST_VR0) ;
    *regPtrChar  = 0; /* Clear time-out vector */
    regPtrShort  = (unsigned short *)(corboBaseAddr + CORBO_TEST1) ;
    *regPtrShort = 0; /* Prepare to trigger */
    *regPtrShort = FULLBYTE; /* and then trigger once ( set busy) */
    regPtrShort  = (unsigned short *)(corboBaseAddr + CORBO_CNT1) ;
    *regPtrShort++ = 0; /* Clear event counter */
    *regPtrShort = 0;
    regPtrShort  = (unsigned short *)(corboBaseAddr + CORBO_TOU1) ;
    *regPtrShort = 0; /* Clear dead time counter */
    regPtrShort  = (unsigned short *)(corboBaseAddr + CORBO_CSR1) ;
    *regPtrShort = CHANNELENABLE | BUSYLATCHED | INPUTFRONTPANEL |
      LOCALBUSYOUT | COUNTBUSY;

    if (DAQCONTROL->burstPresentFlag) {
#ifdef FREEEVENTCOUNTER
      /* Channel 2 initialization.
         Input=event number, output not used,
         event counter=event number (all the events) */
      regPtrShort  = (unsigned short *)(corboBaseAddr + CORBO_CSR2) ;
      *regPtrShort = CHANNELENABLE | INPUTINTERNAL | COUNTINPUT ;
      regPtrChar  = (unsigned char *)(corboBaseAddr + CORBO_BIM1 + OFST_CR1) ;
      *regPtrChar = 0; /* Disable event interrupt */
      regPtrChar  = (unsigned char *)(corboBaseAddr + CORBO_BIM1 + OFST_VR1) ;
      *regPtrChar = 0; /* Clear event vector */
      regPtrChar  = (unsigned char *)(corboBaseAddr + CORBO_BIM2 + OFST_CR1) ;
      *regPtrChar = 0; /* Disable time-out interrupt */
      regPtrChar  = (unsigned char *)(corboBaseAddr + CORBO_BIM2 + OFST_VR1) ;
      *regPtrChar  = 0; /* Clear time-out vector */
      regPtrShort  = (unsigned short *)(corboBaseAddr + CORBO_TEST2) ;
      *regPtrShort = 0; /* Prepare to trigger */
      *regPtrShort = FULLBYTE; /* and then trigger once ( set busy) */
      regPtrShort  = (unsigned short *)(corboBaseAddr + CORBO_CNT2) ;
      *regPtrShort++ = 0; /* Clear event counter */
      *regPtrShort = 0;
      regPtrShort  = (unsigned short *)(corboBaseAddr + CORBO_TOU2) ;
      *regPtrShort = 0; /* Clear dead time counter */
      regPtrShort  = (unsigned short *)(corboBaseAddr + CORBO_CSR2) ;
      *regPtrShort = CHANNELENABLE | INPUTFRONTPANEL | COUNTINPUT ;
#endif

      /* Channel 3 initialization.
         Input=start of burst, output=in-burst interval,
         event counter=burst started (on this LDC) */
      regPtrShort  = (unsigned short *)(corboBaseAddr + CORBO_CSR3) ;
      *regPtrShort = CHANNELENABLE | BUSYLATCHED | INPUTINTERNAL |
        LOCALBUSYOUT | COUNTBUSY;
      regPtrChar  = (unsigned char *)(corboBaseAddr + CORBO_BIM1 + OFST_CR2);
      *regPtrChar = 0; /* Disable event interrupt */
      regPtrChar  = (unsigned char *)(corboBaseAddr + CORBO_BIM1 + OFST_VR2);
      *regPtrChar = 0; /* Clear event vector */
      regPtrChar  = (unsigned char *)(corboBaseAddr + CORBO_BIM2 + OFST_CR2);
      *regPtrChar = 0; /* Disable time-out interrupt */
      regPtrChar  = (unsigned char *)(corboBaseAddr + CORBO_BIM2 + OFST_VR2);
      *regPtrChar  = 0; /* Clear time-out vector */
      regPtrShort  = (unsigned short *)(corboBaseAddr + CORBO_TEST3) ;
      *regPtrShort = 0; /* Prepare to trigger */
      *regPtrShort = FULLBYTE; /* and then trigger once ( set busy) */
      regPtrShort  = (unsigned short *)(corboBaseAddr + CORBO_CNT3) ;
      *regPtrShort++ = 0; /* Clear event counter */
      *regPtrShort = 0;
```

```
      regPtrShort  = (unsigned short *)(corboBaseAddr + CORBO_TOU3) ;
      *regPtrShort = 0; /* Clear dead time counter */
      regPtrShort  = (unsigned short *)(corboBaseAddr + CORBO_CSR3) ;
      *regPtrShort = CHANNELENABLE | BUSYLATCHED | INPUTFRONTPANEL |
        LOCALBUSYOUT | COUNTBUSY;

      /* Channel 4 initialization.
         Input=end of burst, output=out-of-burst interval,
         event counter=burst ended (on this LDC) */
      regPtrShort  = (unsigned short *)(corboBaseAddr + CORBO_CSR4) ;
      *regPtrShort = CHANNELENABLE | BUSYLATCHED | INPUTINTERNAL |
        LOCALBUSYOUT | COUNTBUSY;
      regPtrChar  = (unsigned char *)(corboBaseAddr + CORBO_BIM1 + OFST_CR3) ;
      *regPtrChar = 0; /* Disable event interrupt */
      regPtrChar  = (unsigned char *)(corboBaseAddr + CORBO_BIM1 + OFST_VR3) ;
      *regPtrChar = 0; /* Clear event vector */
      regPtrChar  = (unsigned char *)(corboBaseAddr + CORBO_BIM2 + OFST_CR3) ;
      *regPtrChar = 0; /* Disable time-out interrupt */
      regPtrChar  = (unsigned char *)(corboBaseAddr + CORBO_BIM2 + OFST_VR3) ;
      *regPtrChar  = 0; /* Clear time-out vector */
      regPtrShort  = (unsigned short *)(corboBaseAddr + CORBO_TEST4) ;
      *regPtrShort = 0; /* Prepare to trigger */
      *regPtrShort = FULLBYTE; /* and then trigger once ( set busy) */
      regPtrShort  = (unsigned short *)(corboBaseAddr + CORBO_CNT4) ;
      *regPtrShort++ = 0; /* Clear event counter */
      *regPtrShort = 0;
      regPtrShort  = (unsigned short *)(corboBaseAddr + CORBO_TOU4) ;
      *regPtrShort = 0; /* Clear dead time counter */
      regPtrShort  = (unsigned short *)(corboBaseAddr + CORBO_CSR4) ;
      *regPtrShort = CHANNELENABLE | BUSYLATCHED | INPUTFRONTPANEL |
        LOCALBUSYOUT | COUNTBUSY;
    }

    /* Initialize flags */
    eventArrivedFlag = 1;
    sobArrivedFlag = 1; /* Force to clear h/w the first time */
    eobArrivedFlag = 1; /* Force to clear h/w the first time */
    burstCount = 0;
    eventsInBurstCount = 0;
}

void DisArmCorbo( char *parPtr) {}

int EventArrivedCorbo( char *parPtr) {
  /* Returns a value > 0 when a trigger has occurred */

  int value;

  /****** Re-initialize electronics and flags */
  if (DAQCONTROL->burstPresentFlag) {
    if  (sobArrivedFlag == 1) {
      sobArrivedFlag = 0;
      *regPtrShortCLEAR3 = FULLBYTE; /* Clear SOB busy */
    }
    if  (eobArrivedFlag == 1) {
      eobArrivedFlag = 0;
      *regPtrShortCLEAR4 = FULLBYTE; /* Clear EOB busy */
    }
  }

 if  (eventArrivedFlag == 1) {
    eventArrivedFlag = 0;
    *regPtrShortCLEAR1 = FULLBYTE; /* Clear event busy */
  }

  /****** Now check whether anything happened in the mean time*/
  if (DAQCONTROL->burstPresentFlag) {
    if (!DAQCONTROL->inBurstFlag) {
      value = *regPtrShortCSR3 & (LOCALBUSYPRESENT | DIFFBUSYPRESENT);
```

```
      if ((sobArrivedFlag = (value == 0) ? 0 : 1)) {
        *regPtrShortCLEAR4 = FULLBYTE; /* Clear EOB busy */
        return (sobArrivedFlag);
      }
    } else {
      value = *regPtrShortCSR4 & (LOCALBUSYPRESENT | DIFFBUSYPRESENT);
      if ((eobArrivedFlag = (value == 0) ? 0 : 1)) {
        return (eobArrivedFlag);
      }
    }
    value = *regPtrShortCSR1 & (LOCALBUSYPRESENT | DIFFBUSYPRESENT);
    if ((eventArrivedFlag = (value == 0) ? 0 : 1)) {
      return (eventArrivedFlag);
    }
    return 0; /* default exit */
  } else {
    value = *regPtrShortCSR1 & (LOCALBUSYPRESENT | DIFFBUSYPRESENT);
    return (eventArrivedFlag = (value == 0) ? 0 : 1);
  }
}

void ReadEventCorbo( char *parPtr,
                     struct eventHeaderStruct *header_ptr) {
  int nbInRun;
  if (DAQCONTROL->burstPresentFlag) {
    if (sobArrivedFlag == 1) {
      eventsInBurstCount    = 0;
      header_ptr->type      = START_OF_BURST;
      header_ptr->nbInBurst = eventsInBurstCount;
      header_ptr->burstNb   = ++ burstCount;
      header_ptr->nbInRun   = 0;
      return;
    }
    if (eobArrivedFlag == 1) {
      header_ptr->type      = END_OF_BURST;
      header_ptr->burstNb   = burstCount;
      return;
    }
    header_ptr->nbInBurst = ++ eventsInBurstCount;
    header_ptr->burstNb = burstCount;
  }

#ifdef FREEEVENTCOUNTER
  {
    int triggerNb;
    /* Read local trigger counter from channel 1 (twice 16 bits) */
    triggerNb = (*regPtrShortCNT1A << 16);
    triggerNb |= *regPtrShortCNT1B;
    if (triggerNb != DAQCONTROL->triggerCount + 1) {
      printf ( ``Trigger count mismatch: s/w %d h/w %d\n'',
               DAQCONTROL->triggerCount + 1,
               triggerNb);
    }

    /* Read official event number from CORBO channel 2 (twice 16 bits) */
    nbInRun = (*regPtrShortCNT2A << 16);
    nbInRun |= *regPtrShortCNT2B;

    /* This is the experiment official event number: set it in the header */
    header_ptr->nbInRun = nbInRun;

    if (nbInRun != triggerNb ) {
      printf ( ``Event number mismatch: CORBO 1 %d CORBO 2 %d\n'',
               triggerNb,
               nbInRun);
    }
  }
#else
  /* Read official event number from CORBO channel 1 (twice 16 bits) */
```

```
  nbInRun = (*regPtrShortCNT1A << 16);
  nbInRun |= *regPtrShortCNT1B;

  /* This is the experiment official event number: set it in the header */
  header_ptr->nbInRun = nbInRun;
#endif
}

/* ******************** CBD *********************** */
unsigned int camacBaseAddr;     /* the memory base address of the CBD */
unsigned short B;               /* Branch number */
unsigned int CBDCSR;            /* CSR register */
typedef struct {
  unsigned int *vmeBaseAddressPtr;
  unsigned short *branch;               /* Branch number */
  unsigned short *nbCrates;             /* How many crates you have? */
} CBDParType;

void ArmCBD( char *parPtr){
  unsigned short readData;
  CBDParType * cbdPar = (CBDParType *)parPtr;

  camacBaseAddr = (unsigned int)vmeWinAddr
    + *cbdPar->vmeBaseAddressPtr
    - (unsigned int)vmeWinOffset;
  B = *cbdPar->branch;

  CBDCSR = camacBaseAddr + BCNAF(B, 0, 29, 0, 0);

  /* Initialize the CAMAC crates */
  readData = getm16 (camacBaseAddr + BCNAF(B,1,28,9,26));
  readData = getm16 (camacBaseAddr + BCNAF(B,1,30,9,24));
}

void DisArmCBD( char *parPtr){}

void ReadEventCBD( char *parPtr, struct eventHeaderStruct * header_ptr){}

/* *************************** Kurchatov ADC ******************************* */
/* Kurchatov 64+3-channel memory ADC, readout by F0A0 */
/* words 1-64 : data */
/* word 65-66 : temperature  */
/* word 67 : control word */

unsigned int KurchatovADC_F0;    /* Read data */
unsigned int KurchatovADC_F8;    /* Generate LAM */
unsigned int KurchatovADC_F9;    /* Reset registers */
unsigned int KurchatovADC_F16A1; /* For writting gain code */
unsigned int KurchatovADC_F16A0; /* Select module to read out */
typedef struct {
  unsigned short *numberOfModules; /* Number of Kurchatov Modules */
  unsigned short *numberOfChs;     /* Number of ADC channeds per module */
  unsigned short *C;               /* Crate Address */
  unsigned short *N;               /* Station Address */
  unsigned short *gain;   /* gain code 0,1,2 or 3 (0 is default for minimum) */
  short *eqIdPtr;
}KurchatovADCParType;

void ArmKurchatovADC( char *parPtr){
  KurchatovADCParType *kurchatovAdcPar = (KurchatovADCParType *)parPtr;
  unsigned short rdata;

  /* Initialize some register for further using  */
  KurchatovADC_F0 = camacBaseAddr + BCNAF(B, *kurchatovAdcPar->C,
                                          *kurchatovAdcPar->N, 0, 0);
  KurchatovADC_F8 = camacBaseAddr + BCNAF(B, *kurchatovAdcPar->C,
                                          *kurchatovAdcPar->N, 0, 8);
  KurchatovADC_F9 = camacBaseAddr + BCNAF(B, *kurchatovAdcPar->C,
                                          *kurchatovAdcPar->N, 0, 9);
```

```
  KurchatovADC_F16A0 = camacBaseAddr + BCNAF(B, *kurchatovAdcPar->C,
                                             *kurchatovAdcPar->N, 0,16);
  KurchatovADC_F16A1 = camacBaseAddr + BCNAF(B, *kurchatovAdcPar->C,
                                             *kurchatovAdcPar->N, 1, 16);
  putm16 KurchatovADC_F16A1 = *kurchatovAdcPar->gain;
  rdata = getm16 KurchatovADC_F9;
}

void DisArmKurchatovADC( char *parPtr){}

int ReadEventKurchatovADC( char *parPtr, struct eventHeaderStruct *header_ptr,
                           struct equipmentHeaderStruct *eq_header_ptr,
                           int *data_ptr){
  unsigned short timeout;
  unsigned short loop;
  unsigned short loop_m;
  unsigned short ADC_KURCHATOV_MODULE;
  unsigned short ADC_KURCHATOV_CH;
  unsigned short rdata;
  int * firstWord = data_ptr;
  KurchatovADCParType *kurchatovAdcPar = (KurchatovADCParType *)parPtr;
  ADC_KURCHATOV_MODULE = *kurchatovAdcPar->numberOfModules;
  ADC_KURCHATOV_CH = *kurchatovAdcPar->numberOfChs;

  /* SOB and EOB treatment: no data */
  if ( ((EVENT_TYPE_MASK & header_ptr->type) != PHYSICS_EVENT) &&
       ((EVENT_TYPE_MASK & header_ptr->type) != CALIBRATION_EVENT) ){
    return ( (unsigned long32)data_ptr - (unsigned long32)firstWord );
  }

  /* Physics or calibration data */
  /* mark equipment structure present in the event header */
  header_ptr->type |= EVENT_EQUIPMENT;

  /* fill the equipment header */
  eq_header_ptr->equipmentId = *kurchatovAdcPar->eqIdPtr;
  eq_header_ptr->rawByteAlign = 2;

  /* Read Kurchatov ADC and fill the raw data */
  timeout = 200;        /*  wait a little bit */
  while (timeout --){
    rdata = getm16 KurchatovADC_F8;
    if ((getm16 CBDCSR) & 0x8000) goto readoutKurchatovADC;
  }

  /* no LAM, pad channels */
  for (loop_m = 0; loop_m < ADC_KURCHATOV_MODULE; loop_m++){
    putm16 KurchatovADC_F16A0 = loop_m;
    for (loop = 0; loop < ADC_KURCHATOV_CH; loop++){
      *data_ptr = 0;
      data_ptr ++;
    }
  }
  printf( ‘‘No LAM from Kurchatov ADC!?\n’’);

  goto end_of_readout;

 readoutKurchatovADC:
  for (loop_m = 0; loop_m < ADC_KURCHATOV_MODULE; loop_m++){
    putm16 KurchatovADC_F16A0 = loop_m;
    for (loop = 0; loop < ADC_KURCHATOV_CH; loop++){
      *data_ptr = getm16 KurchatovADC_F0;
      data_ptr ++;
    }
  }

 end_of_readout:
  rdata = getm16 KurchatovADC_F9;     /* Reset Kurchatov ADC */
```

```
  /* returns the number of bytes of raw data actually readout */
  return ( (unsigned long32) data_ptr - (unsigned long32) firstWord );
}

equipmentDataTableType equipmentDataTable[] = {
  equipmentDataType( KurchatovADC)      /* for PHOS beam test */
};
int nbDtEqps = sizeof(equipmentDataTable)/sizeof(equipmentDataTable[0]);

equipmentNoDataTableType equipmentNoDataTable[] = {
  equipmentNoDataType( VmeWindow),
  equipmentNoDataType( CBD)                     /* for PHOS beam test */
};
int nbNoDtEqps = sizeof(equipmentNoDataTable)/sizeof(equipmentNoDataTable[0]);

triggerDataTableType triggerDataTable[]= {};
int nbDtTrgs = 0;

triggerNoDataTableType triggerNoDataTable[] = {triggerNoDataType( Corbo)};
int nbNoDtTrgs = sizeof(triggerNoDataTable)/sizeof(triggerNoDataTable[0]);
```